AD-A278 413

ENTATION PAGE

1. AGENCY USE ONLY (Leave blank)	2. REPORT DATE February 28th, 1994	3. REPORT TYPE AND DATES COVERED Final July 1990 - Nov. 1993

4. TITLE AND SUBTITLE

Luminescence and Electroluminescence of Nd, Tm and Yb Doped GaAs and some II-Vi compounds.

5. FUNDING NUMBERS

AFOSR-90-0322

6. AUTHOR(S)

Principal Investigator:
Professor DSc. Dr. H. J. Lozykowski

7. PERFORMING ORGANIZATION NAME(S) AND ADDRESS(ES)

Ohio University
Office of Research and Sponsorod Programs
Athens, Ohio 45701-2979

DTIC
SELECTE
APR 20 1994
S B D

8. PERFORMING ORGANIZATION REPORT NUMBER

AFOSR-TR- 94 0241

9. SPONSORING / MONITORING AGENCY NAME(S) AND ADDRESS(ES)

AFOSR / PKD
Building 410
Bolling AFB, DC 20332-6448

10. SPONSORING / MONITORING AGENCY REPORT NUMBER

2315ES

11. SUPPLEMENTARY NOTES

12a. DISTRIBUTION / AVAILABILITY STATEMENT

Approved for public release; distribution unlimited.

unlimited

12b. DISTRIBUTION CODE

13. ABSTRACT (Maximum 200 words)

This report describes the progress accomplished during the three year of research on photoluminescence and electroluminescence properties of Nd, Tm, Yb doped, InP, GaAs, CdS, and ZnS. The results are as follow: I) We developed the kinetics model of energy transfer from the host lattice to the localized core excited state of rare earth isoelectronic structured traps. The energy transfer processes occur through an Auger mechanism where the recombination energy of the bound electron with a free hole is transferred nonradiatively to the core states, (or energy can be transferred from the bound exciton on an REI-trap to the core states). If the initial and final states are not resonant, the energy mismatch must be accommodated by emission or absorption of phonons. Furthermore we discuss details of several quenching processes, which are incorporated into the kinetics equations. The derived two sets of differential equations for semi-insulating, and n type semiconductors governing the kinetics of rare earth luminescence. The numerically simulated luminescence rise and decay times show a good quantitative agreement with experimental data obtained for InP: Yb, over a wide range of excitation intensity. The photoluminescence spectra and decay time were also studied as a function of temperature. The new quenching mechanism of ytterbium luminescence involving Yb and Fe ions is proposed. The electric field quenching of InP: Yb photoluminescence was investigated for the first time.

II) The photoluminescence kinetics as a function of excitation intensity in n and p type InP: Yb, and GaAs: Nd grown by MOCVD was studied at 1.8 K and 77 K. The experimental rise time depends on excitation intensity, and is decreasing with

(continued on next page)

14. SUBJECT TERMS

Photoluminescence, Electroluminescence, Spectroscopy, Polarization, GaAs and some II-VI compounds doped with Rare Earth

15. NUMBER OF PAGES

16. PRICE CODE

17. SECURITY CLASSIFICATION OF REPORT	18. SECURITY CLASSIFICATION OF THIS PAGE	19. SECURITY CLASSIFICATION OF ABSTRACT	20. LIMITATION OF ABSTRACT
Unclass	Unclass	Unclass	UL

increasing excitation rate. The rare earth decay occurs by a combination of intrinsic relaxation processes, the Auger energy back transfer processes, and migration and cross relaxation processes. The photoluminescence studies of GaAs: Yb shows no 4f emission.

III) To study the impact excitation mechanism of RE ions in GaAs, we designed five EL heterostructures one of which is a light emitting transistor.

IV) The photoluminescence and time resolved spectra of Nd- and Yb-implanted CdS samples are studied under pulsed and CW excitations, at different excitation intensities and temperatures. The samples were annealed under different conditions using the thermal-pulse method. For CdS: Nd, the PL. spectra were recorded in the ranges: 890-930 nm, 1070-1120 nm, and 1370-1420 nm. The PL spectra of CdS: Yb was recorded in the range 980 - 1010 nm. The excitation spectra were performed using dye and Ti-sapphire lasers. Rise time and decay time were studied for both CdS: Nd and CdS: Yb at different emission lines as a function of temperature and excitation power. The experimental data are discussed and compared with a proposed theoretical kinetics model.

V) The ac electroluminescence of Tm doped ZnS embedded in boric acid matrix was investigated. The El emission spectra were recorded as a function of voltage, frequency and temperature. The emission spectra at all temperatures show only strong sharp emission lines assigned to transitions within the 4f shell of Tm^{3+} ion. The emission spectra consisted of five groups of lines centered on 483 nm, 661.7 nm, 710.5 nm, 785 nm, and 805.5 nm. The experimental values of the 483 emission lines (transition $^1G_4 \rightarrow {}^3H_6$) intensities versus the applied voltage were reproduced theoretically on the basis of the direct impact excitation mechanism. We showed that the direct impact excitation of Tm^{3+} is the dominant excitation mechanism.

VI) In view of the strong enhancement role of Li on luminescence properties of rare earth in II-VI compounds, we study GaAs doped with Er and Li. To our knowledge, no study on influence of Li on Er doped GaAs has been reported in the literature. The GaAs co-doped with Er and Li showed the difference in relative intensities of the emission peaks of Er. The biggest changes in spectra are observed for sample doped with Li at temperatures range 570°C to 650°C.

94-11906

94 4 19 012

Luminescence and Electroluminescence Properties of Nd, Tm, and Yb Doped GaAs and Some II-VI Compounds

Final Report Submitted to :

The Air Force Office of Scientific Research

by :

Henryk J. Lozykowski
Department of Electrical and Computer Engineering
Stocker Center, Ohio University
Athens, Ohio 45701-2979

February 1994

PERSONNEL

Faculty

H. J. Lozykowski, Professor, *Principal Investigator*

Graduate Students

A. K. Alshawa, *Ph.D. Student*
Z. I. Akir, *Ph.D. Student*
T. Li, *Ph.D. Student*

Scientific Papers and Presentations

The following scientific papers have been published (and in preparation) as a result of research performed under Air Force sponsorship:

1. "Digital spectropolarimeter for the measurement of optical polarization"
   H. J. Lozykowski, T. Li, and Z. I. Akir,Rev. Sci. Insrum., v. 63, No. 9, p. 4096 (1992).
2. "Optical properties of CdTe/Cd$_{1-x}$Zn$_x$Te strained-layer single quantum wells"
   T. Li, H. J. Lozykowski, and John L. Reno, Phys. Rev. B, v. 46, No. 11, p. 6961 (1992).
   (partially don in AFB Dayton see I Introduction)
3. "Kinetics of luminescence of isoelectronic rare earth ions in III-V semiconductors"
   H. J. Lozykowski, Phys. Rev. B, Vol.48 No. 24, p. 17758, (1993)
4. "Kinetics of the Luminescence of Isoelectronic Rare-Earth Ions in III-V Semiconductors"
   H. J. Lozykowski, Mat. Res. Soc. Symp. Proc. Vol. 301, 397, (1993)
5. "Luminescence Properties of Nd and Yb doped CdS"
   A. Alshawa and H. J. Lozykowski, Mat. Res. Soc. Symp. Proc. Vol. 301, 281, (1993)
6. "Luminescence Properties of Yb Doped InP" ,H. J. Lozykowski, A. K. Alshawa,
   G. Pomrenk, and I. Brown, Mat. Res. Soc. Symp. Proc. Vol. 301, 263, (1993)
7. "Electroluminescence of Tm Doped ZnS", A.K. Alshawa and H.J. Lozykowski, J of Electrochem. Soc. (in print)
8. "The luminescence rise and decay kinetics of MOCVD-grown InP:Yb and GaAs:Nd".
   H. J. Lozykowski and K. Takahei (in preparation)
9. "Optical Properties of CdTe/Cd$_{1-x}$Zn$_x$Te Strained -Layer Single Quantum Wells"
   Tieshing, Li, Ph.D Disertation, Ohio University, 1993.
10. "Luminescence of rare earth doped semiconductors"
   A. K. Alshawa PhD Disertation, (in preparation)

Presentations

1. "Luminescence Properties of Yb-Doped InP", H. J. Lozykowski, A. K. Alshawa, G. Pomrenke, I. Brown, Bull. Am. Phys. Soc., 36(8), p.2167, C5-4, (1991). Spring Meeting 1991 (short abstract).
2. "Electroluminescence of Tm Doped ZnS" A. K. Alshawa and H. J. Lozykowski, Bull. Am. Phys. Soc., 36(8), CP-6, p.2164 (1991). Spring Meeting 1991 (short abstract).
3. "Photoluminescence Study of Cd$_{1-x}$Zn$_x$Te/CdTe Strained - Layer Single Quantum Wells", T. Li, H. J. Lozykowski, and J. L. Reno, Bull. Am. Phys. Soc., 36(8),C5-5, p. 2167 (1991). Spring Meeting 1991 (short abstract)
4. "Optical Properties of Cd$_{1-x}$Zn$_x$Te/CdTe Strained-Layer Single Quantum Wells" T. Li, H. J. Lozykowski, and J. L. Reno, Advanced Processing and Characterization Technologies, Clearwater FL., 1991.
5. "Luminescence Properties of Nd and Yb doped CdS", A. Alshawa and H. J. Lozykowski, Mat. Res. Soc. Symp. Proc. Vol. 301, 281, (1993)
6. "Luminescence Properties of Yb Doped InP", H. J. Lozykowski, A. K. Alshawa, G. Pomrenk, and I. Brown, Mat. Res. Soc. Symp. Proc. Vol. 301, 263, (1993)
7. "Kinetics of luminescence of isoelectronic rare earth ions in III-V semiconductors" H.J. Lozykowski, Spring Meeting of The Material Research Society- Rare Earth Symposium, San Francisco (1993)

The final research report containes studies of rare earth (RE) centers in semiconductors, namely Yb, Nd, and Tm in GaAs, InP, ZnS and CdS. Special emphasis has been put on the optical properties of the RE centers in semiconductors systems by studing the luminescence rise time of the rare earth doped semiconductors, excited indirectly above the band-gap, contain information about the energy transfer processes from the host to the $4f^n$ electron system.

The results are collected in the following paragraphs and papers:

I Introduction

This final research report containes studies of a rare earth (RE) centers in a semiconductors, namely Yb, Nd, and Tm in GaAs, InP, ZnS and CdS. Special emphasis has been put on the optical properties of the RE centers in semiconductors systems by studing the luminescence rise time of the rare earth doped semiconductors, excited indirectly above the band-gap, contain information about the energy transfer processes from the host to the $4f^n$ electron system. It is shown that the study of the rise time at different temperatures, excitation intensities, and excitation pulse durations can provide important information about the energy transfer, the radiative, and non-radiative processes respectively. We discuss only the structured isoelectronic traps in III-V semiconductors introduced by triply charged rare earth ions replacing the element from column III (or athers more complex RE isoelectronic traps). Furthermore, we develop the luminescence kinetic models (for InP:Yb which can be applied toather semiconductors) that describe the energy transfer and recombination processes. The numerically simulated luminescence rise and decay measurements for InP: Yb show a good quantitative agreement with experiment over a wide range of generation rate. The presence of low lying empty core orbitals in rare earth impurities introduces new excitation and recombination phenomena, which we discussed in detail. Finally the possible quenching mechanisms and the temperature dependence of rare earth luminescence are discussed.

The study of photoluminescence (and electroluminescence) of some II-VI compounds include: ZnS: Tm^{3+}, CdS: Yb^{3+}, CdS: Nd^{3+}. The deep understanding of excitation mechanism in II-VI compounds system can lead to better understanding of excitation mechanism in other more complicated RE^{3+} systems in semiconductors. Figure 1a shows the energy levels scheme of the Nd^{3+} ion in cubic (Td) and noncubic symmetry (C_{v3}, C_{v2}, C_s) environment. In cubic symmetry $^4F_{3/2}$ level is not split (Γ_8 fourfold degenerated crystal field state). Therefore, in the cubic hosts, any splitting of the $^4F_{3/2}$ level is indicative for association of the Nd^{3+} ion with other defects. The same argument holds for the multiplicities of the ground state. The ground state $^4I_{9/2}$ in cubic symmetry is split into three states (Γ_8, Γ_8, Γ_7) and the first excited state $^4I_{11/2}$ into four crystal f-leld states as in the left part of Fig. 1a. In noncubic symmetry, the fourfold degenerate Γ_8 states of
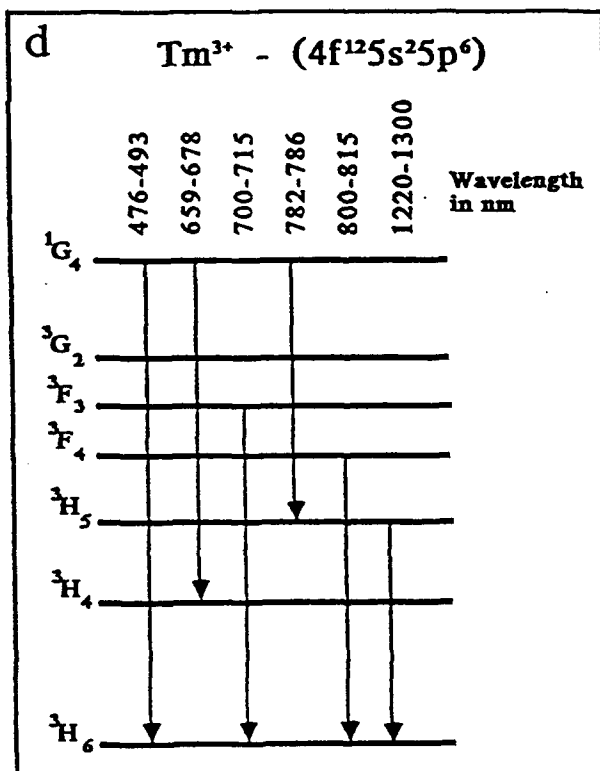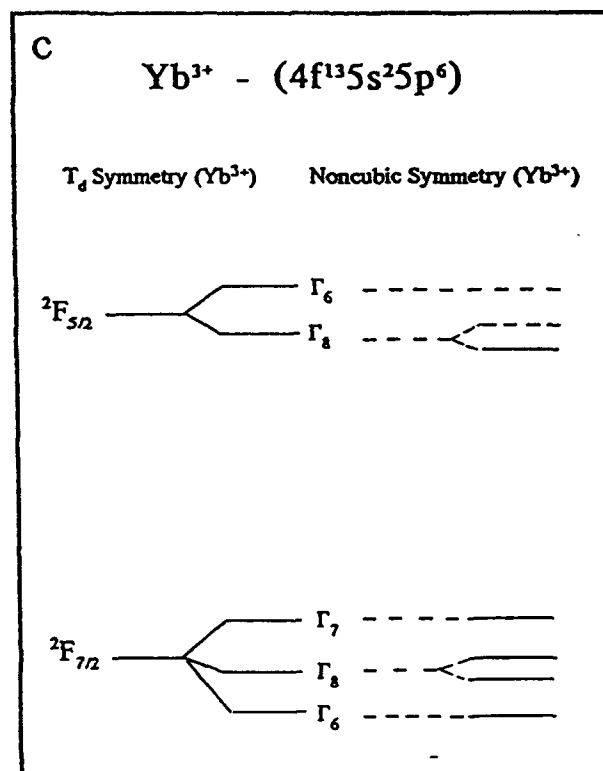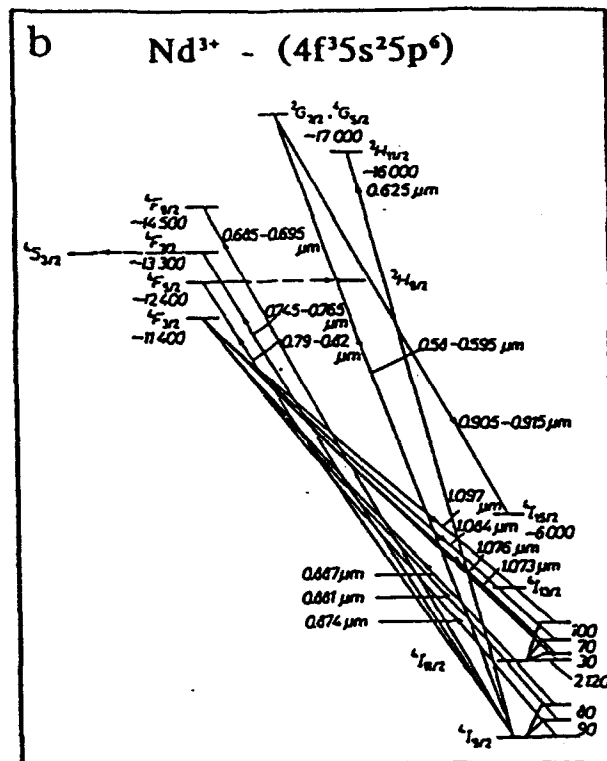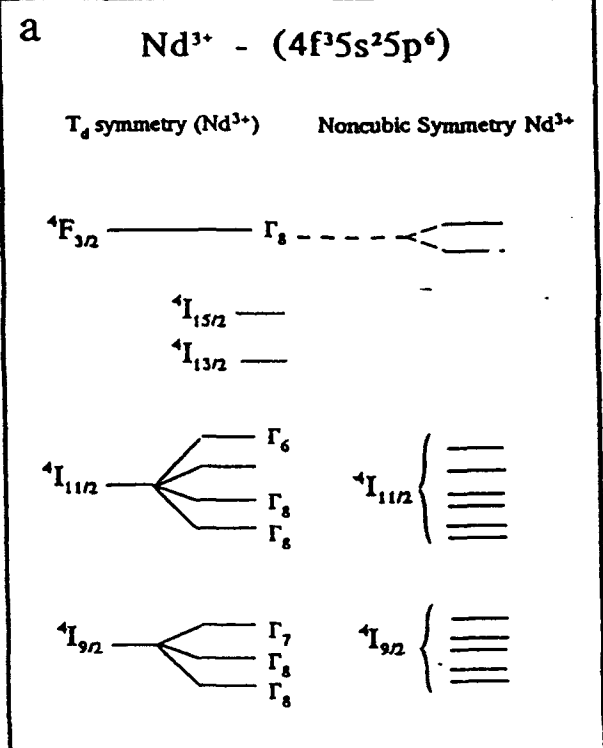
Figure 1 a,b,c,d

Nd^{3+} ion are split into two doublet each and the energy level structure is shown in the right part of Fig. la. The emission spectra for the $^4F_{3/2}$ - $^4I_{9/2}$ transitions of Nd^{3+} in noncubic symmetry should exhibit all ten transitions. At low temperature, when only the lower level of $^4F_{3/2}$ occupied, only 5 lines should be observed in luminescence emission. In absorption at low temperature such that only the lowest component of $^4I_{9/2}$ state is occupied, only two lines should be observed. In Fig. lb we show the possible absorption and emission transition with wavelength (in μm) for Nd^{3+} in cubic symmetry in semiconductors with band gap $E_g \geq 2.14$ eV. Figure 1 c shows energy level schemes for Yb^{3+} ion in cubic (Td) and noncubic symmetry, and the luminescence transition for Tm^{3+} ion in ZnS is shown in Fig.1 d.

During the period of Fall 1991 - Fall 1992, I was on my Faculty Fellowship Leave sponsored partially by Ohio University Faculty Fellowship, the Air Force Office of Scientific Research, and Nippon Telegraph and Telephone Basic Research Laboratory in Tokyo Japan.

The first part (4 months) of my sabbatical leave I spent at Wright Laboratory Solid State Electronics Directorate (WL / ELRA), Wright-Patterson AFB in Dayton Ohio. I collaborated with Dr. K. Evans (and his co-workers), and Dr. Reynolds. Part of published paper (4, see Ch. VIII) namely the streak camera measurement was done in Dr. Reynolds laboratory at AFB in Dayton. During this period I also worked on the theory of indirect photoluminescence excitation of rare earth ions in III-V semiconductors. I spent the second part of my Faculty Fellowship Leave (four and 1/2 months) at the Nippon Telegraph and Telephone Basic Research Laboratory in Tokyo, Japan. I collaborated with Dr. K. Takahei, M. Taniguchi, and A. Taguchi, continuing the research effort initiated at Dayton, on EL structures. The next two projects are: 1) Study the energy transfer mechanism from the host to rare earth isoelectronic traps in MOCVD grown GaAs: Nd, and InP: Yb by investigating the PL rise kinetics as the function of excitation intensity (in preparation). 2) Study of the lithium influences on the photoluminescence spectra of MOCVD grown GaAs: Er sample (see Chapter III).

During my sabbatical leave I presented several seminars on photoluminescence and its kinetics of rare earth doped semiconductors, at Wrigth Laboratory and at NTT Tokyo. Currently, Dr. T. Li and I collaborate with Drs. D. Reynolds, and K. Evans on polarization spectroscopy of coupled double quantum wells AlGaAs / GaAs (research in progress).

To study the electroluminescence, and especially the direct impact excitation mechanism of rare earth in III-V semiconductors I designed the four EL structures and Dr. K. Evans with coworkers grew them using MBE system. (The grown structures unfortunately were not doped with Er caused by depleted Er source in MBE machine). The reason why we are trying to excite the RE ions by direct impact is that, the RE^{3+} ions cannot be effectively excited by energy transfer from host to RE core states. We believe that this is a reason the efficiencies of the III-V: RE^{3+} crystals are low. Some materials such as GaAs: Yb and InP: Nd does not show luminescence under band to band host excitation. The direct excitation, either optically or electrically is the only way to excite these ions. We would also like to prove it experimentally. Some of the hetrostructures proposed below are the devices where the carriers can gain energy from the bandgap discontinuity (as was proposed in my publications [1,2]). Also, by using superlattice structure AlGaAs / GaAs: Er / AlGaAs, we could manipulate the band gap energy. In each case, more upper states of rare earth RE^{3+} (Er) could be used as the pumping levels that might result in a higher luminescence (EL, PL) efficiency. It will be important to compare this direct impact excited devices with the conventional LEDs to see the difference in excitation mechanisms and to see which of them are more efficient. It is interesting to understand what happens physically when the rare earth ions collide with hot carriers. The rare earth ions could be excited by the following mechanisms: (a) A hot electron, with energy equal to the RE^{3+} 4f-shell transition energy, collides with the RE^{3+} ions and directly transfers its energy to the RE 4f-shell electron, (b) If an electron gains enough energy, it might ionize a rare earth ion. The ionized RE^{3+} ions can then recapture another electron with RE 4f-shell in the excited state, and (c) The high electric field creates hot electrons which by collisions with the lattice can generate electron hole pairs. In such a case, the RE^{3+} ions could be excited through host energy transfer mechanism, similar to above bandgap photoluminescence (PL) excitation.

With a careful study, we can determine which excitation mechanism is dominant one, and can probably obtain information about the hot electron distribution. The most likely excitation mechanism is the (a) mechanism that uses the hot carriers (electrons) with energy equals or higher than the RE 4f-shell internal transition energy. The direct inelastic collision of such hot electrons with the RE^{3+} ions transfers its energy to the 4f electron, and creates the excited RE^{3+} ions. The designed electroluminescence structures are:

1. Figure 2a shows the metal - semiconductor (doped with RE) - insulator - semiconductor (doped with RE) - metal (MSISM) structure. The device operates based on tunneling of electrons through a thin (~150Å-200Å) dielectric layer. In the designed device based on GaAs instead of insulators with very wide bandgap, we used undoped $Al_{0.45}Ga_{0.55}As$ - 200Å thick layer. On both sides of the AlGaAs layer, we have 50Å GaAs layers and 0.4 μm thick GaAs layer doped with Er and Si (lightly n-type) covered by heavily doped (n^+) GaAs: Si layer. The ohmic contacts were applied to both n^+ GaAs sides completed the structure. The MSISM structure is symmetric and can operate by applying AC voltage as shown in Figure 2b. The hot electrons tunneled through the dielectric layer, (where most of the applied voltage dropped) should have sufficient energy to excite by impact the RE centers. The structure, should operate at low voltage.

Figure 3 shows the asymmetric structure in which the left side is the same as in Figure 2 while the right side contains the GaAs p-n junction with very thin (~ 150Å) p region. When the p-n junction is forward bias, an electron will be injected in the conduction band of the p-layer. The hot electrons will be tunneled across the AlGaAs layer into GaAs: Er, Si layer , and by direct impact will excite the RE^{3+} ions.

2. The p^+-i-n^+ structure grown by MBE on an n^+ GaAs substrate is shown in Figure 4. The p^+-i-n^+ diode consists of three semiconductor regions: the 2500 Å thick p^+ $Al_{0.45}Ga_{0.55}As$: Be ($\sim$ 5×10^{19} cm^{-3}), the n^+ GaAs: Si region and the semi-insulating linearly graded GaAs-AlGaAs 'i' region of width d doped with Er ($\sim$ 6×10^{18} cm^{-3}). The three regions are capped with a 50Å thick p^+ GaAs: Be layer. By applying the reverse bias, the depletion region and internal field is forming in the graded 'i' region. With a sufficiently large voltage, the depletion region can punch through from p^+ to n^+ layer as shown in Figure 4. The injected electrons (by light) through the thin p^+ region, are accelerated in a strong and well-defined electric field, and can gain energy equal to or larger than the RE 4f-shell internal transition energy. If such a hot electron collides with the RE^{3+} ion, it can directly transfer its energy to the RE 4f-shell electrons and therefore creates an excited RE^{3+} centers.
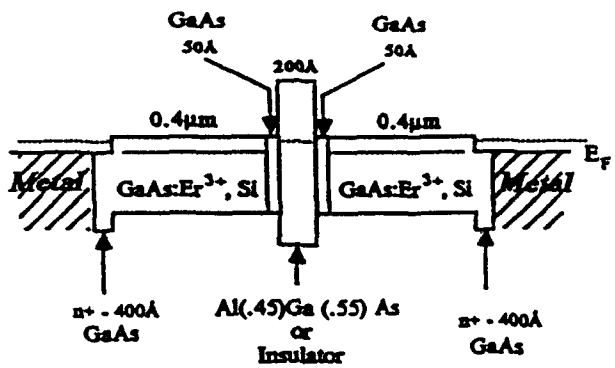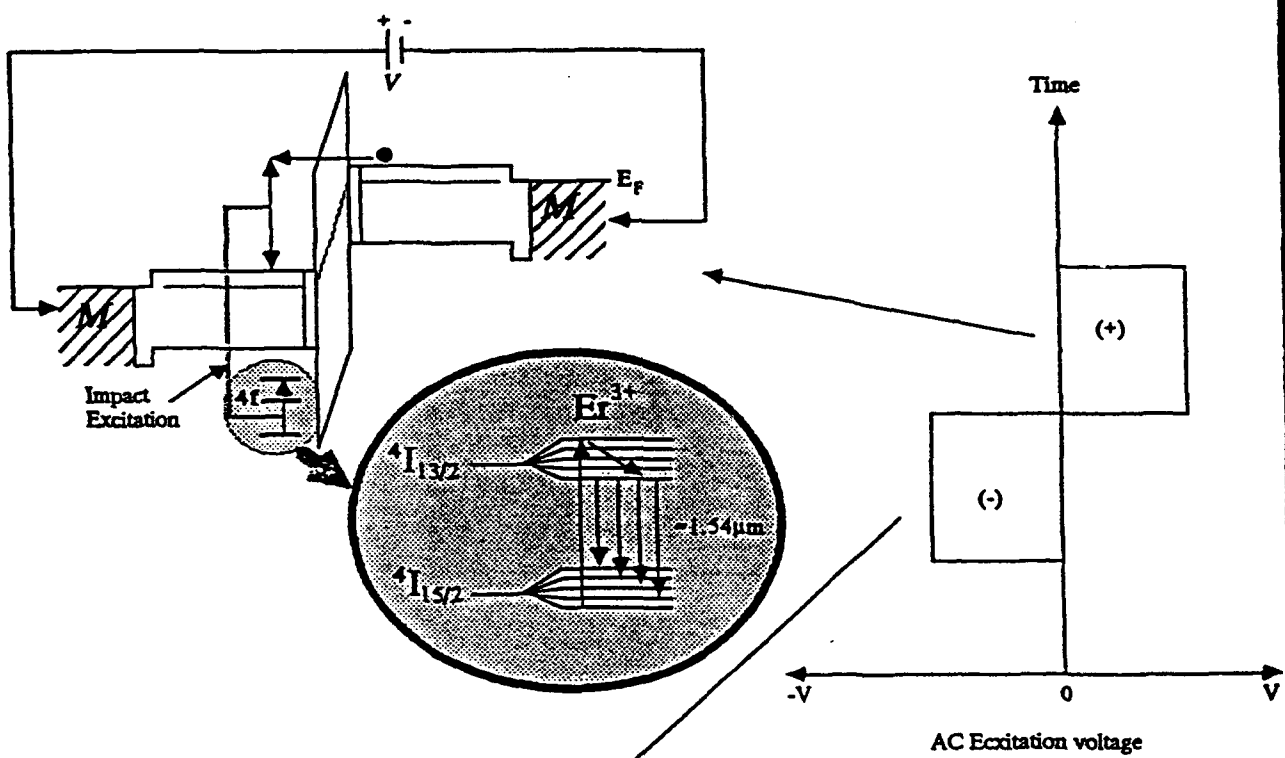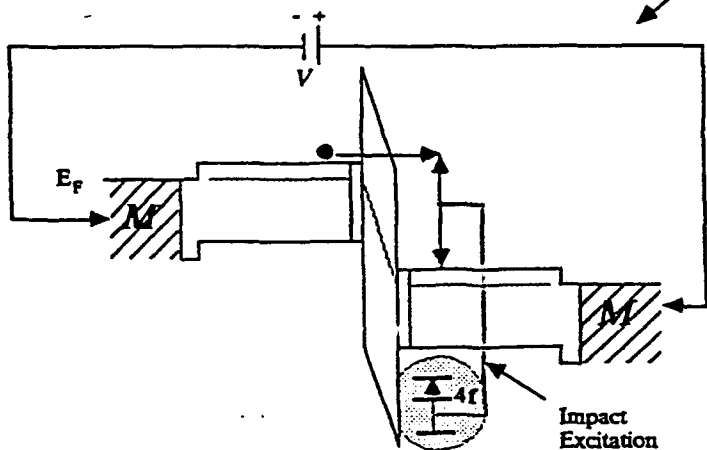
Figure 2 a, b
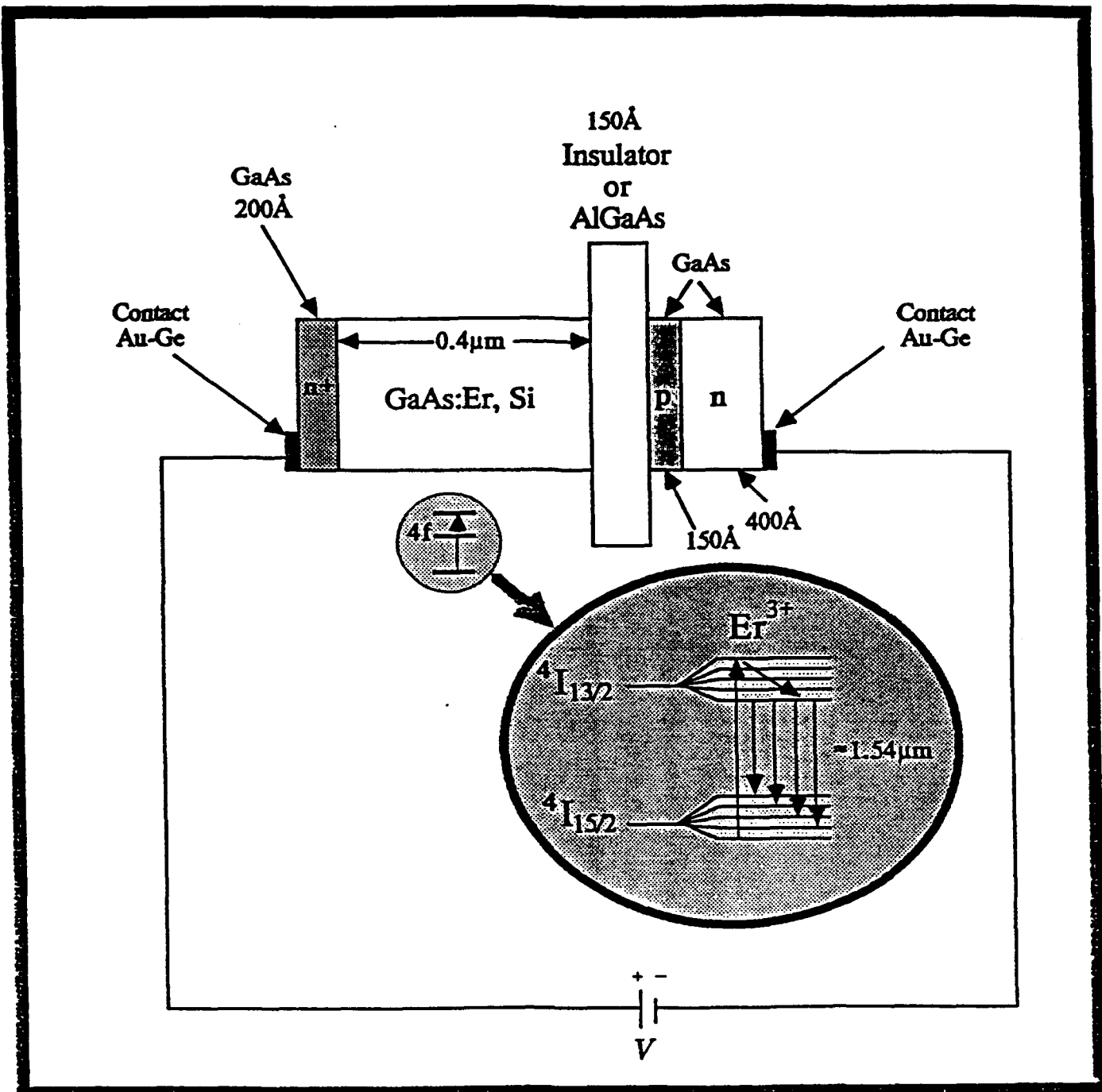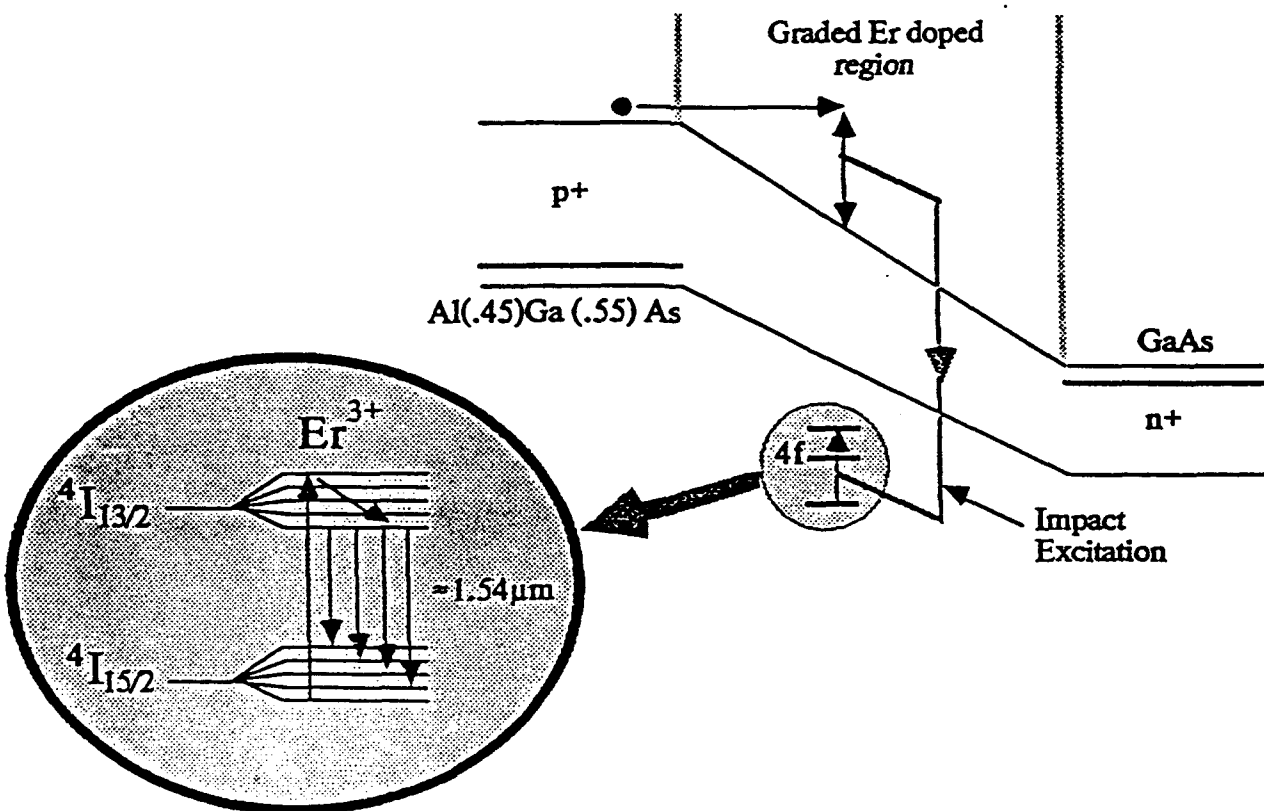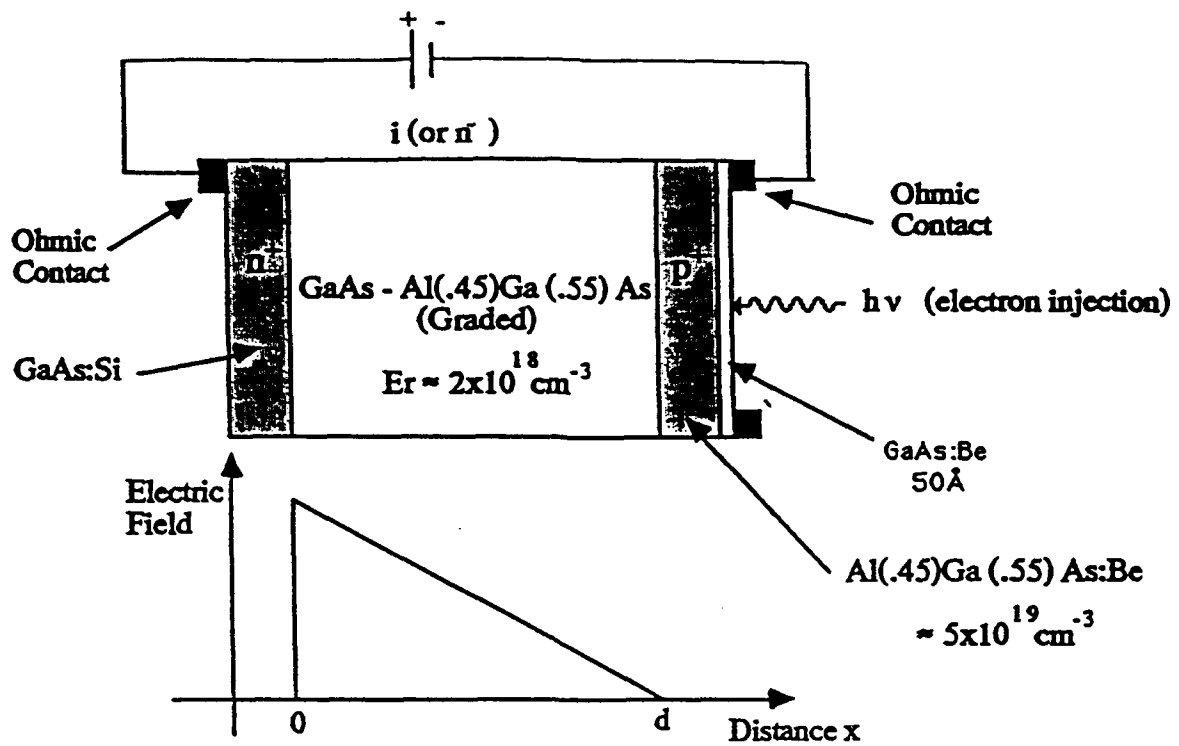
Figure 3

Figure 4 The p-i-n impact light emitting device

3.   The AlGaAs/GaAs: Er/AlGaAs superlattice structure. For the first time we designed the unipolar n^+ - superlattice - n^+ structure as shown in Figure 5. The GaAs: Er/$Al_{0.45}Ga_{0.55}As$ superlattice was grown by MBE on an n^+ GaAs: Si substrate. It consisted of 60 periods of nominally 350Å wide GaAs: Er (~ $2x10^{18}cm^{-3}$) quantum wells and 100 Å thick $Al_{0.45}Ga_{0.55}As$ barriers, sandwiched between 450 Å thick GaAs: Er, Si and 0.5 μm thick n^+ GaAs: Si cap layers. The calculation made for the above superlattice shows that because of thick barriers (100 Å), the confined levels are localized states rather than extended subbands. In Figure 6, we show the conduction and the valence band edge of the superlattice doped with Er^{3+} ($2x10^{18}$ cm^{-3}), at a bias voltage above the impact excitation threshold of 4f electrons. After further increase of the external bias, some electrons are accelerated until they will reach the threshold energy for impact generation of electrons-hole pairs, and electroluminescence of the superlattice should be observed.

The light emitting structure described in Figure 4 required for operation injection of electrons to region "i." It can be done by light generation of electron hole pairs in p^+ region. To overcome this drawback, I designed during my stay at NTT Tokyo new structure, the light emitting transistor (LET). The new LET structure is shown in Figure 7 (with and without bias). If the emitter base heterojunction is forward biased, the electrons are injecting through the base region to "i" region of the reverse bias p-i-n structure. The electrons are accelerated in a strong and well-controlled electric field existing in "i" region. The hot electron by direct impact with RE^{3+} ions, excite the core states of rare earth ions.

1.   H. J. Lozykowski, Solid State Comm. 66, 755 (1988)

2..   H. J. Lozykowski, in "Electroluminescence" Edited by S. Shionoya and H. Kobayashi, Springer Proceedings in Physics, 38, 60 (1989)

II   **Experimental Techniques**

A.   **Sample Preparation Ion Implantation**

The ion implantation of rare earth was done by Dr. I. G. Brown from Lawrence Berkeley Laboratory at the University of Califomia, Berkeley. Implantation of Nd ' Yb, and Tm was performed with an unconventional implantation technique using a new kind of high current metal ion source developed at Berkeley by Dr. Brown et al. This Metal Vapor Vacuum Arc (MEVVA)
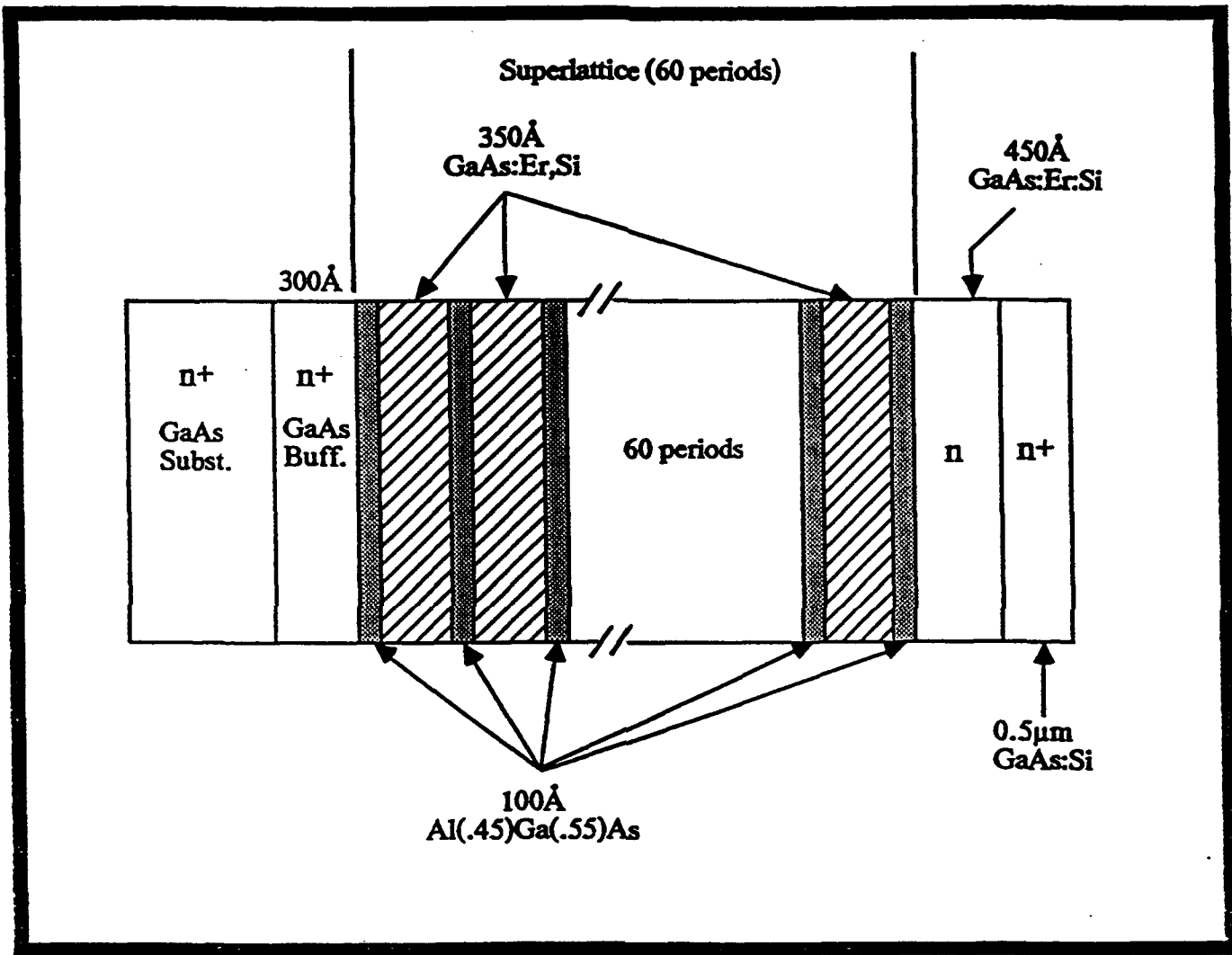
Figure 5 AlGaAs/GaAs:Er/AlGaAs, 60 periods superlattice doped with Er
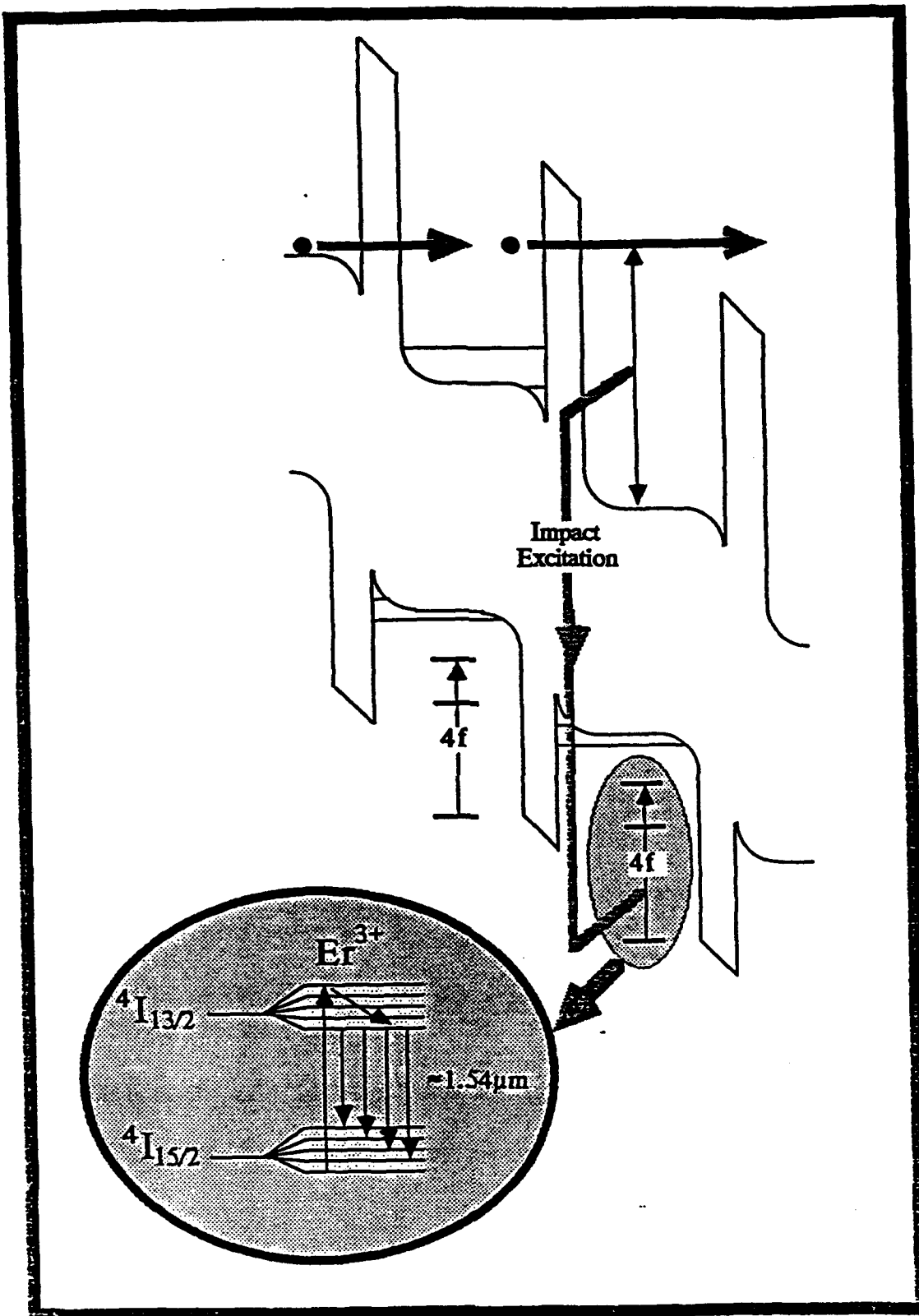
Figure 6 Conduction- and valence-band edge of the superlattice doped with rare-earth at a bias voltage above the impact excitation threshold of rare earth ions. The arrows indicate electron transport the impact excitation and recombination process.
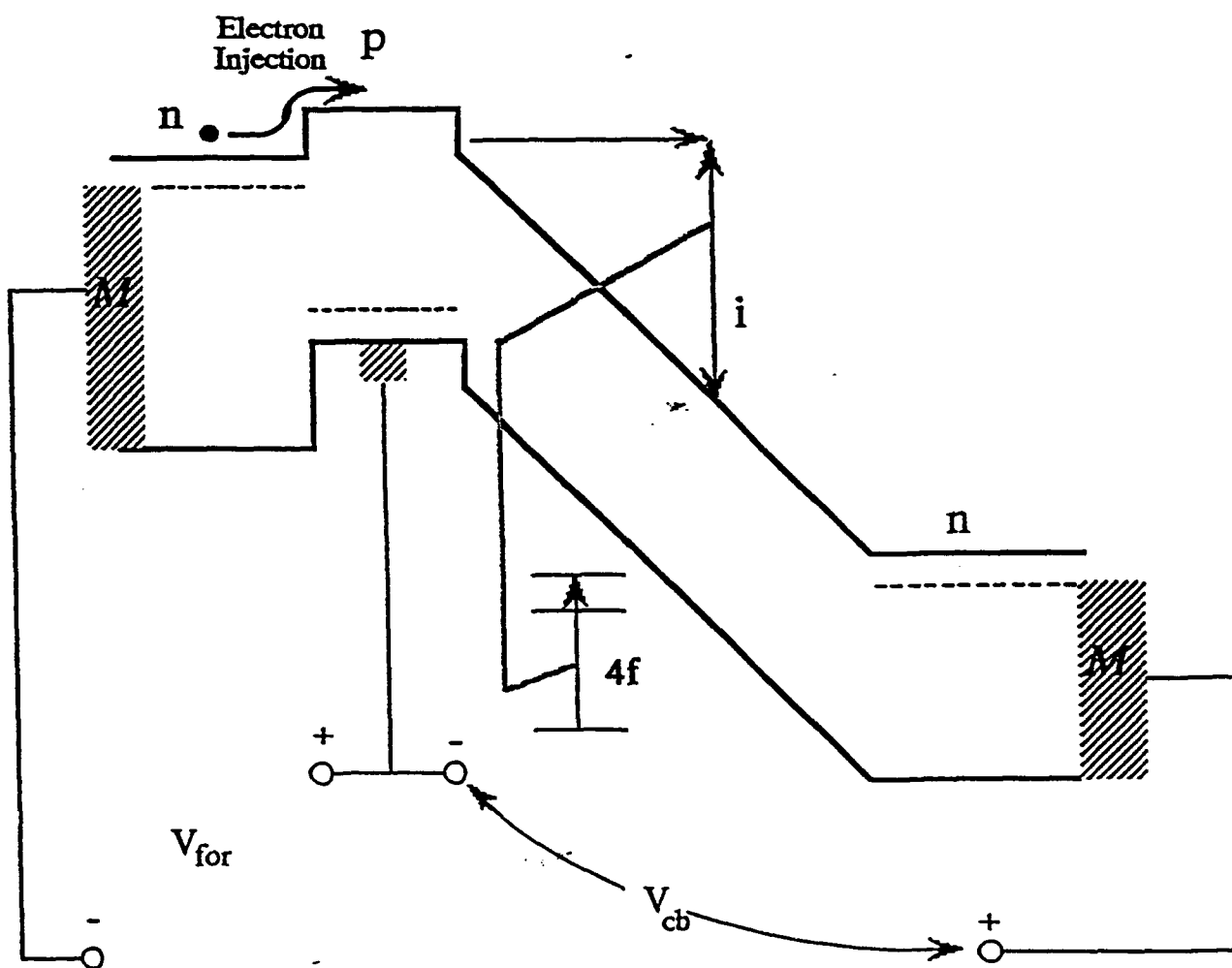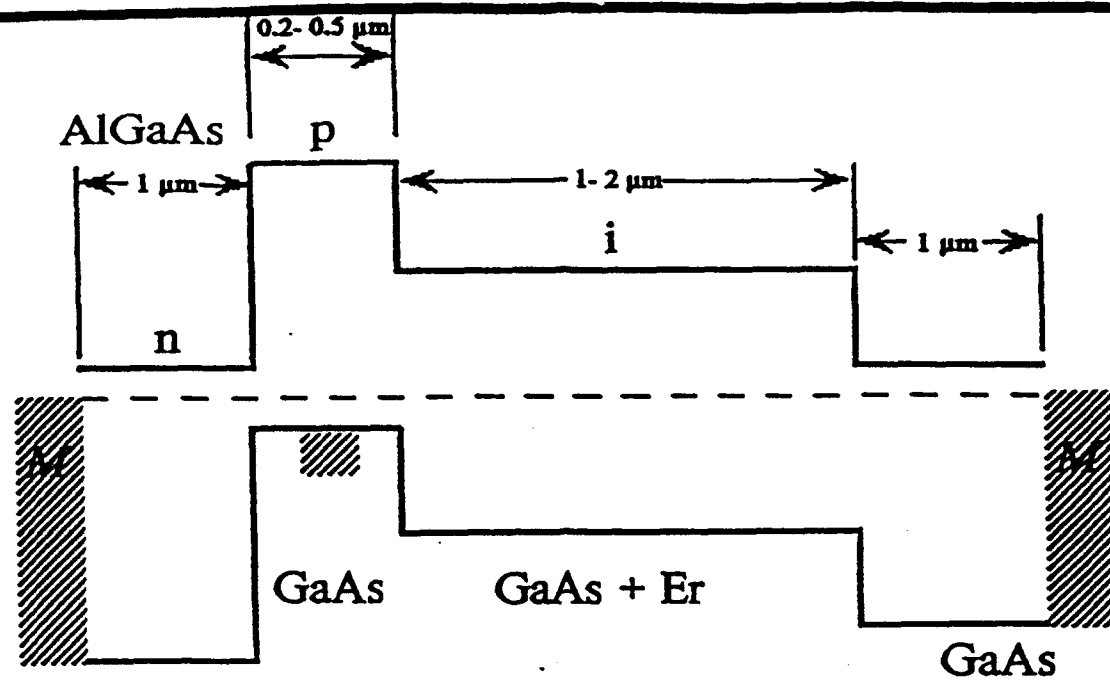
Figure 7 Light Emitting Transistor

ion source makes use of a dense metal plasma generated directly from the metal cathode material as the medium from which ions are extracted. The source is repetitively pulsed and the implantation is done on a broad beam mode, with a direct line -of-sight from the ion source to the target. High current beams of a wide range of multiply-charged metal ions can be produced. Beam extraction voltage is up to 100 kV, for a mean ion energy of up to several hundreds of key by virtue of a mean ion charge state that is typically 2 to 3. The beam current can be up to several amperes peak and around 10 mA time averaged delivered onto target. The source has been operated with virtually all of the solid metals of the periodic table. The high energy implants of 1 MeV were implanted at Universal Energy Systems (LYES), Dayton, OH.

B. Annealing

The samples were cut to small pieces (4 mm x 4 mm squares) and then cleaned by standard methods. Thermal heat-pulse using a strip heater was used to anneal the samples up to 900^0 C for 10- 15 sec. The annealing process was performed using the apparatus shown in Fig. 8 which we designed and built in our laboratory. A flat graphite plate of 3 mm thick is placed on the tantalum strip heater. The samples are placed with the implanted face down on the graphite plate and covered with a graphite lid of 1 mm thickness. The temperature is measured by microprocessor controlled temperature indicator OMEGA model 650 through a thermocoupie placed inside the bottom graphite plate. The variation of annealing temperature with time is recorded by an y-x recorder as shown in the insert of Fig. 1. The rise time of the temperature was controlled by the AC voltage applied to the strip heater. For temperatures up to 900 °C, our system maintains a rise time of 6 sec and a decay time from 900 °C to 500 °C of 22 sec.

C. Spectropolarimeter

For photoluminescence (electroluminescence) polarization measurements we modified our digital spectropolarimeter to operate at the spectral range from 450 nm to 2000 nm (in digital mode the range from 450 nm to 1200 nm is limited by the photomultiplier spectral response.) The modified optical range was accomplished utilizing Oriel Fresnel rhomb achromatic retarders. The
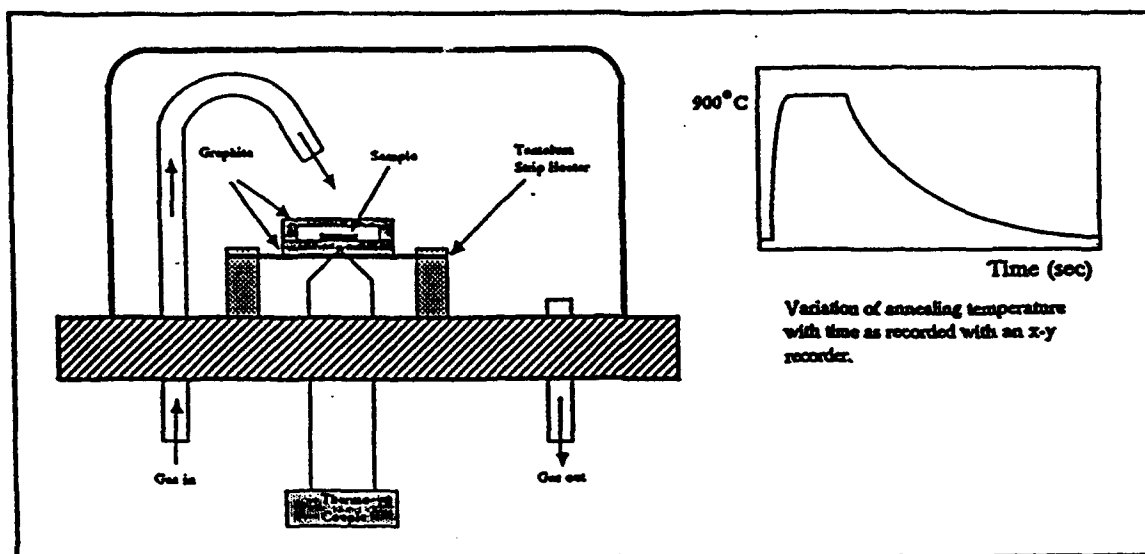
Figure 1 Thermal-Heat-Pulse Annealing System

quarter wave or the half wave achromatic retarders are in series with a Glan-Thompson crystal polarizer in the excitation channel to provide $90^0 \pm 2^0$ ($\sigma+$ or σ) or $180^0 \pm 2^0$ (linear polarization) phase retardation. The heart of the setup consists of a photo-elastic modulator (PEM-80) and a dual channel gated photon counter which has the capability to compensate the variation of excitation intensity with time and wavelength. The second important modification is automatic wavelength tracking of the modulator to insure the constant retardation phase ($\pi/2$ or $\pi/4$) when the wavelength of the analyzed light is scanned in wide range. The angular aperture of PEM-80 modulator comprises a 50 degree full-cone angle. Unlike the conventional lock-in or other analog systems, where the difference of two oppositely polarized light components (AC) and the average of these components (DC) are extracted electronically, and the ratio AC/DC is recorded as degree of polarization, our setup directly records theσ^+ and σ^- components (or, in the case of linear polarization, $I_{|}$ and $I_\perp$ components) of the light signal in the same run (of wavelength, temperature, etc.) A detailed description of the spectropolarimeter system is in paper Chapter VIII.

III   Photoluminescence Study of GaAs:Er diffused with Li

A. Introduction

II-VI semiconductors containing rare earth activators have been of interest for many years. Such materials have a discrete ion as the principle source of luminescence emission, the 4f-4f transitions yielding narrow emission band or lines. For all earliest investigations of rare earth in II-VI compounds see review[1]. The 4f-4f line emissions from many rare earths co-doped with Cu and Ag are accompanied by characteristic broad band emission of the host material. In 1965, Yocom and Larach [2] showed that the effect of charge compensation particularly by alkali metals reduces the band emission of ZnS and ZnCdS doped with rare earth and enhances the rare earth emission at room temperature. Shrader [3], extending the work of Yocom and Larach, reported on the details of charge-compensation effect in ZnS doped with dysprosium.

The proposed model [1-3] of rare earth center in II-VI compounds assumed that the trivalent rare earth was in a substitute lattice site for Zn with a near-neighbor vacancy being present for charge compensation purposes. They assumed that such a rare earth-vacancy system resulted in broad band emission, and that filling the vacancy by simplest type of cationic charge compensating species chosen from the group IS ions (the alkali metal ions) in particular lithium, would result in strong narrow line emission normally expected from 4f-4f transition. The experimental results indeed have shown that the addition of alkali metals ions to ZnS doped with rare earths decreases or eliminates the band emission of the host crystals while selectively intensifying the sharp emission line of 4f-4f transitions.

The fluoride ion also reduced the broad band emission and enhanced strongly the line emission of the rare earth. In this case (fluoride), it is assumed that interstitial fluorides compensate the rare earth eliminating the need for a vacancy. Despite the model for compensation mechanism, the several crystallographically nonequivalent positions exist for all the possible compensators to be found. The luminescence emissions from such nonequivalent sites cause the line broadening and the appearing of extra emission lines. The rare earth alkali metal ions' complex centers are responsible for the drastic intensification of certain 4f-4f transitions, as opposed to the non-alkali containing materials.

Studies of Li in GaAs were quite extensive in the early seventies, and they have provided

information about solubility, diffusion data and local mode energies from IR spectroscopy [4]. Recently photoluminescence studies of Cu_{Ga}--Li_i complexes and double ionize Li_{Ga} acceptor [5], and influence of Li incorporation on luminescence of n-type Si, Se or Sn doped, and p-type Zn doped, or SI GaAs ware reported [6a,b]. The interactions of Li and Cu in GaP create the neutral complexes of isoelectronic character [7,8]. Both these group-I species are fast interstitial diffusers, and in complexes both can occupy Ga sites. At least five different Cu-Li complex's ware observed in GaP after a subsequent Li diffusion into Cu doped material. These centers are characterized by their different bond exciton luminescence spectra, all of them being neutral associates of isoelectronic molecular type. In addition Li form neutral linear Li_i-Li_{Ga}-O_p <111>-oriented defect in GaP, which has been studied via its bound exciton spectra [9].

In view of the above strong enhancement role of Li on luminescence properties of rare earth in II-VI compounds, and involve in creation "isoelectronic" defects, we focus our attention on the behavior of Li in GaAs doped with Er. To our knowledge, no study on influence of Li on Er doped GaAs has been reported in the literature. Below, we present for the first time photoluminescence spectra for GaAs: Er, Li. In section B we describe the Li doping procedure used in this work emphasizing the different types of MOCVD samples used to avoid systematic errors. We also briefly describe the experimental techniques employed (section C). Section D contains the experimental results and discussion.

B. Sample Preparation

The GaAs : Er sample used in this study was grown by MOCVD at two different temperatures on a non doped GaAs substrate (orientation (100)). The epitaxial layers of about 1.3 μm and 1.1 μm with Er concentration 1.5 $\times$ 10^{18} /cm^3 were grown at temperature 500°C and 600°C respectively. Lithium diffusions were done into GaAs: Er, and into n-type and p-type MOCVD epitaxial layer at different temperatures. Table I, II and III summarize the properties of the starting materials and Li diffusion conditions. The Li (purity 99.9 %) diffusion was done in sealed quartz ampules, sample was in small crucible, the Li metal foil and As (purity 99.9999 %) were in additional quartz liner with one end closed in order to protect the ampule from chemical reaction with Li. The ampules and Li foil were cleaned in toluene (ultrasonic base), alcohol and deionized water and evacuated to 4 $\times$ 10^7 mbar. The As metal was added for protection of GaAs

from changing stoichiometry. The samples were rapidly cooled to room temperature after heat treatment by immersing the quartz ampule into water. The reference samples were given identical heat treatment as the Li-diffused one but without the Li source and only with As.

Table I

Sample [substrate GaAs SI (100)]	Dopant: Er concentration	Epitaxial layer thickness	Growth temperature V / III ratio ~30
P52 (1,2,3,4)	$1.5\ 10^{18}$ / cm^3	1.3 μm	500 °C
P4X (1,2,3,4)	$1.5\ 0^{18}$ / cm^3	1.1 μm	600 °C

Sample P52 & P4X

		6	5
1	2	3	4
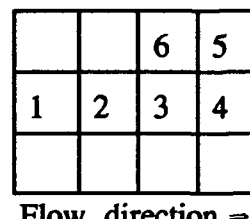
Flow direction ⇒

thicker   thinner

Table II

Sample GaAs (SI) (100)	Dopant : Er concentration	Epitaxial layer thickness	Diffusion conditions, (all sample cooled in water)
P52(1)	$1.5 \, 0^{18} / cm^3$	$1.3 \, \mu m$	Li+As,570 ^{0}C, 6h
P52(2)a	$1.5 \, 0^{18} / cm^3$	$1.3 \, \mu m$	Li+As,500 ^{0}C, 6h
P52(2)b	$1.5 \, 0^{18} / cm^3$	$1.3 \, \mu m$	Li+As,500 ^{0}C, 6h + Li+As,802 ^{0}C,1h
P52(3)	$1.5 \, 0^{18} / cm^3$	$1.3 \, \mu m$	
P52(4)	$1.5 \, 0^{18} / cm^3$	$1.3 \, \mu m$	Li+As,646 ^{0}C, 6h + Li+As,802 ^{0}C, 1h
P52(5)	$1.5 \, 0^{18} / cm^3$	$1.3 \, \mu m$	As, 802 ^{0}C, 1h
P52(6)	$1.5 \, 0^{18} / cm^3$	$1.3 \, \mu m$	
P4X(1)	$1.5 \, 0^{18} / cm^3$	$1.1 \, \mu m$	Li+As,802 ^{0}C, 6h
P4X(2)	$1.5 \, 0^{18} / cm^3$	$1.1 \, \mu m$	Li+As,500 ^{0}C, 6h
P4X(3)	$1.5 \, 0^{18} / cm^3$	$1.1 \, \mu m$	
P4X(4)	$1.5 \, 0^{18} / cm^3$	$1.1 \, \mu m$	Li+As,646 ^{0}C, 6h
P4X(5)	$1.5 \, 0^{18} / cm^3$	$1.1 \, \mu m$	As, 802 ^{0}C, 1h
P4X(6)	$1.5 \, 0^{18} / cm^3$	$1.1 \, \mu m$	

Table III

Sample GaAs (100)	Dopant and concentration	Epitaxial layer thickness	Diffusion conditions, (all sample cooled in water)
P5E (sub.:Si)	Se 7.7 1 0^{18}/cm^3	1.2 μm	Li+As, 800 ^{0}C, 1h
P5F (sub. undoped)	Se 7.7 1 0^{18}/cm^3	1.2 μm	Li+As, 802 ^{0}C, 80 min.
P5X (sub. undoped)	Zn 1.8 10^{19}/cm^3	2.3 μm	Li+As, 802 ^{0}C, 1h
P5Y (sub. undoped)	Zn 1.4 10^{17}/cm^3	2.3 μm	Li+As, 802 ^{0}C, 1h
P2A(1) (sub. undoped)	$n = 1.5 \, 0^{15}$/cm^3 $\mu = 4.110^3$ [cm^2/Vs]	3.5 μm	Li, 500 ^{0}C, 7h
P2A(2)	" "	3.5 μm	Li, 570 ^{0}C, 6h
P2A(3)	" "	3.5 μm	Li, 409 ^{0}C, 72h
P2A(4)	" "	3.5 μm	As, 570 ^{0}C, 6h (ref.)
P2A(5)	" "	3.5 μm	Li+As, 800 ^{0}C, 80 min.

C. Experimental Techniques and Results.

The photoluminescence measurements were done at 2 K and at 77 K. For excitation, the 632.8 nm line of He-Ne laser (10mW) and the 514.5 nm line of Ar^+ laser (20 mW) were used. The photoluminescence signal was analyzed with a 1.25-m monochromator and was detected with a Ge photodetector cooled to 77 K. Figure 1 shows an example of SIMS bulk analysis of two epilayers grown by MOCVD and diffused with Li. The concentrations of Li are 3 - 4 $\times$ 10^{18} cm^{-3} to 4 $\times$ 10^{18} cm^{-3} dependent on diffusion temperature and time. Figure 2 a, b, c shows photoluminescence spectra from sample P4X in the wavelength range of 800 nm to 1700 nm grown under condition shown in Table I. The reference spectrum for sample as grown is shown in figure 2a. The dominant is the RE emission, the near band edge bound exciton peak is also seen. The PL spectra after Li diffusion at temperature 500°C, and 646°C during 6 hours, are shown in Fig. 2 b, and c, respectively. Sample diffused at 500°C (Fig.2b) shows, beside the RE emission, new broad band with peak at 1.02 eV, and much weaker band edge emission. Figure 2c shows the drastic change in spectrum after Li diffusion at 646°C. Strong DA pair emission appears at 1.465 eV, and the Cu-Li peak at 1.41 eV [5] shows up. The strong band at 1.36 eV with the shoulder at 1.34 eV, and 1.02 eV band grows strongly. In Fig. 3 a, b, c we show the detail of rare earth spectra for above sample recorded in the spectral range of 1.5 μm to 1.6 μm. Spectra on figure 3a, b, for the sample as grown and Li diffused at 500°C are almost identical. The erbium spectrum of sample doped with Li at 646°C (Fig.3c) shows the different relative intensities of the emission lines in comparison with the first two samples. Figure 4 and Fig. 5 show the erbium spectra from samples P52 with grown condition described in Table I. In Fig.4a the PL spectrum of a reference sample (as grown) is shown, b and c are the spectra after diffusion of Li at 500 °C and 570 °C during 6 hours, respectively. The only differences between these samples are different relative intensities of the emission peaks, as seen on Fig. 4d where we overlap the spectrum (a) and (c). The difference reflects the Li doping of the GaAs:Er epilayers at different temperatures. PL spectra shown on Fig.5 a, b are recorded for samples P52(4) (a) and P52 (3). Sample P52 (4) was diffused with Li twice at 646°C for 6h and additionally at 802°C for 1 hour (Table II), sample P52 (3) as grown. The diffusion at 802°C reduced the intensity of Er emission and broadened the spectrum.
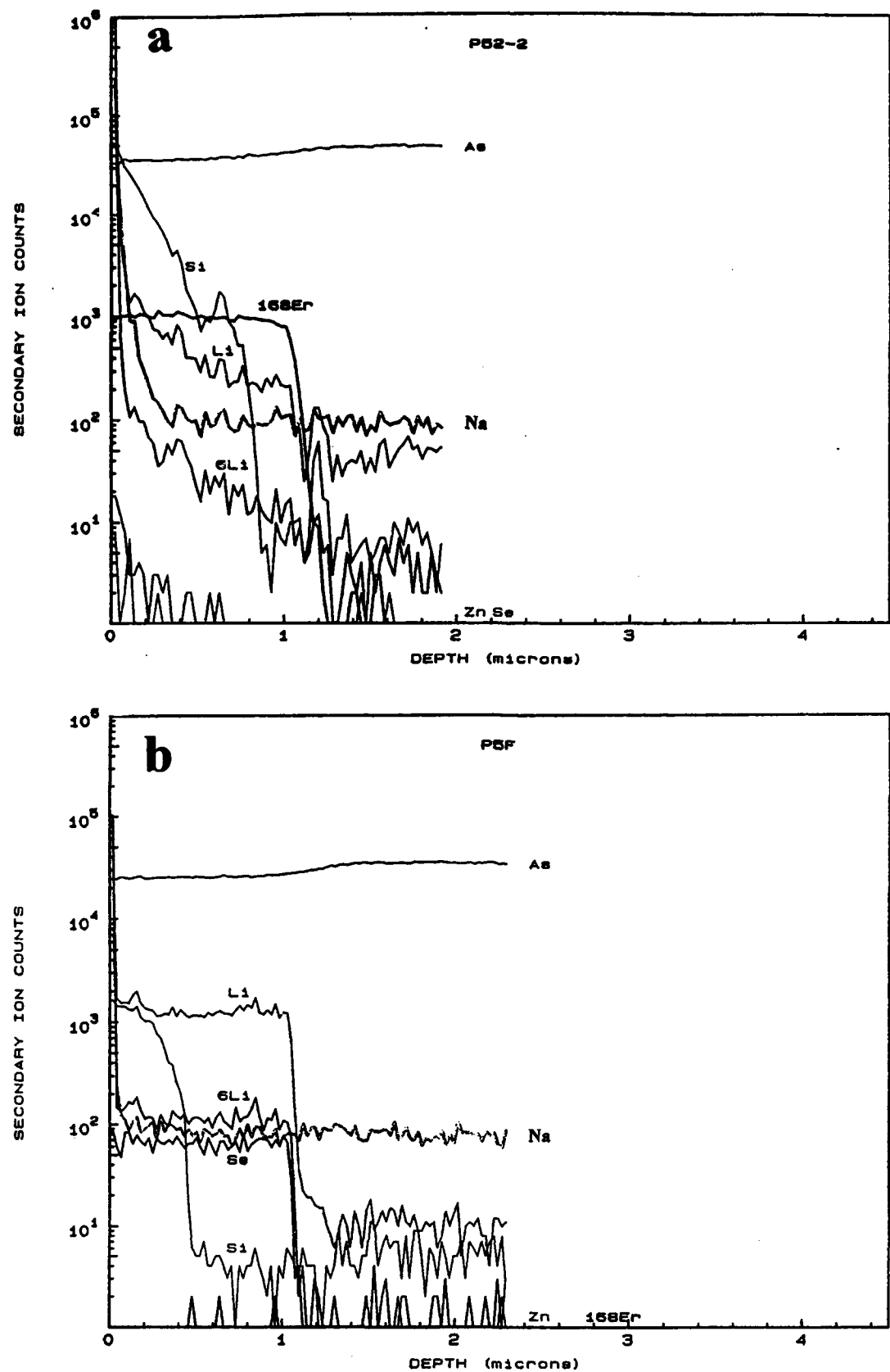
Fig. 1   Examples of SIMS bulk analysis of two epilayers grown by MOCVD and diffused with Li (concentration of 4×10^{18} cm^{-3}). (a) sample P5F and (b) P52(2) [see tables]
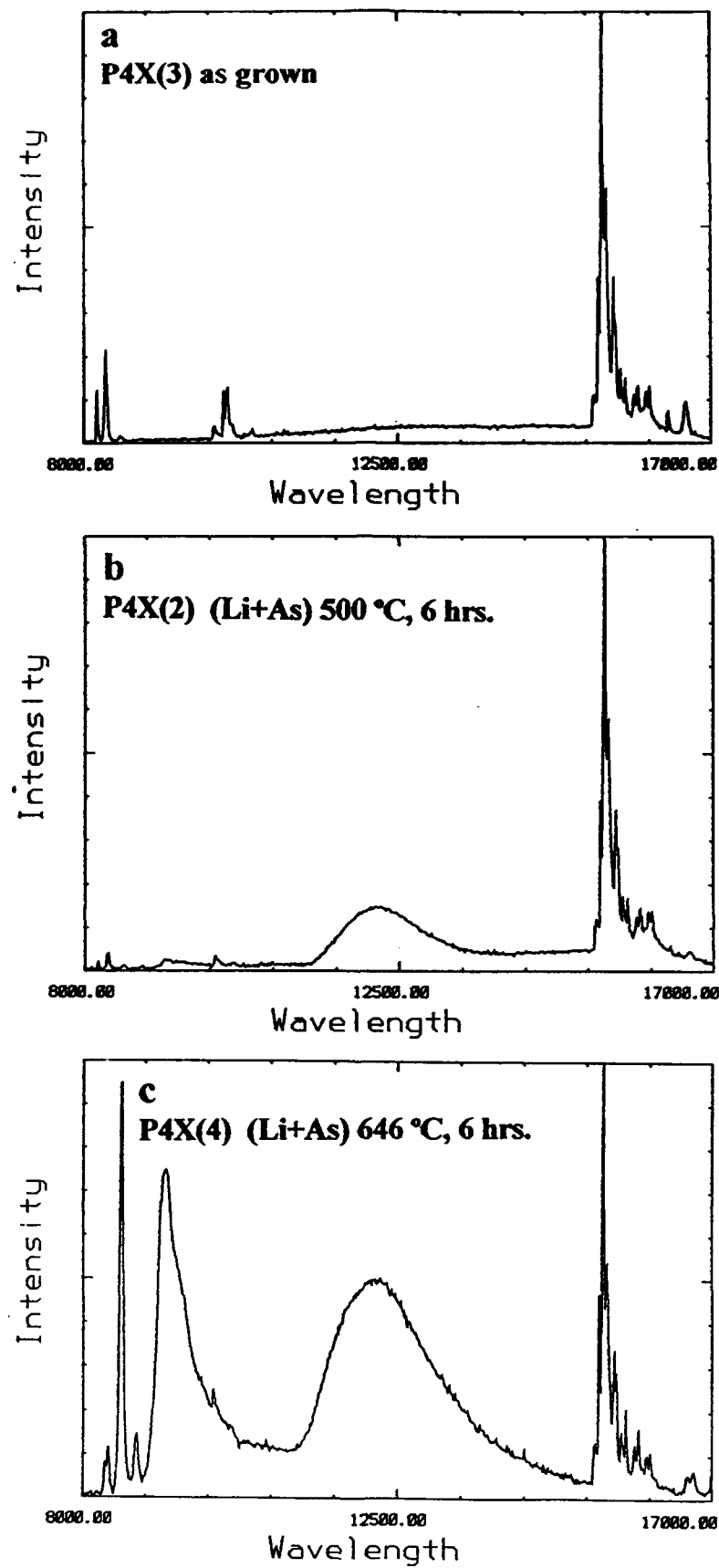
Fig. 2 The photoluminescence spectra of P4X samples recorded at 2 K in the range 800 - 1700 nm using He-Ne laser (10 mW). (a) is the reference spectrum of GaAs:Er as grown. In (b) and (c) the samples are diffused with Li at temperature 500 °C and 646 °C for 6 hours, respectively.
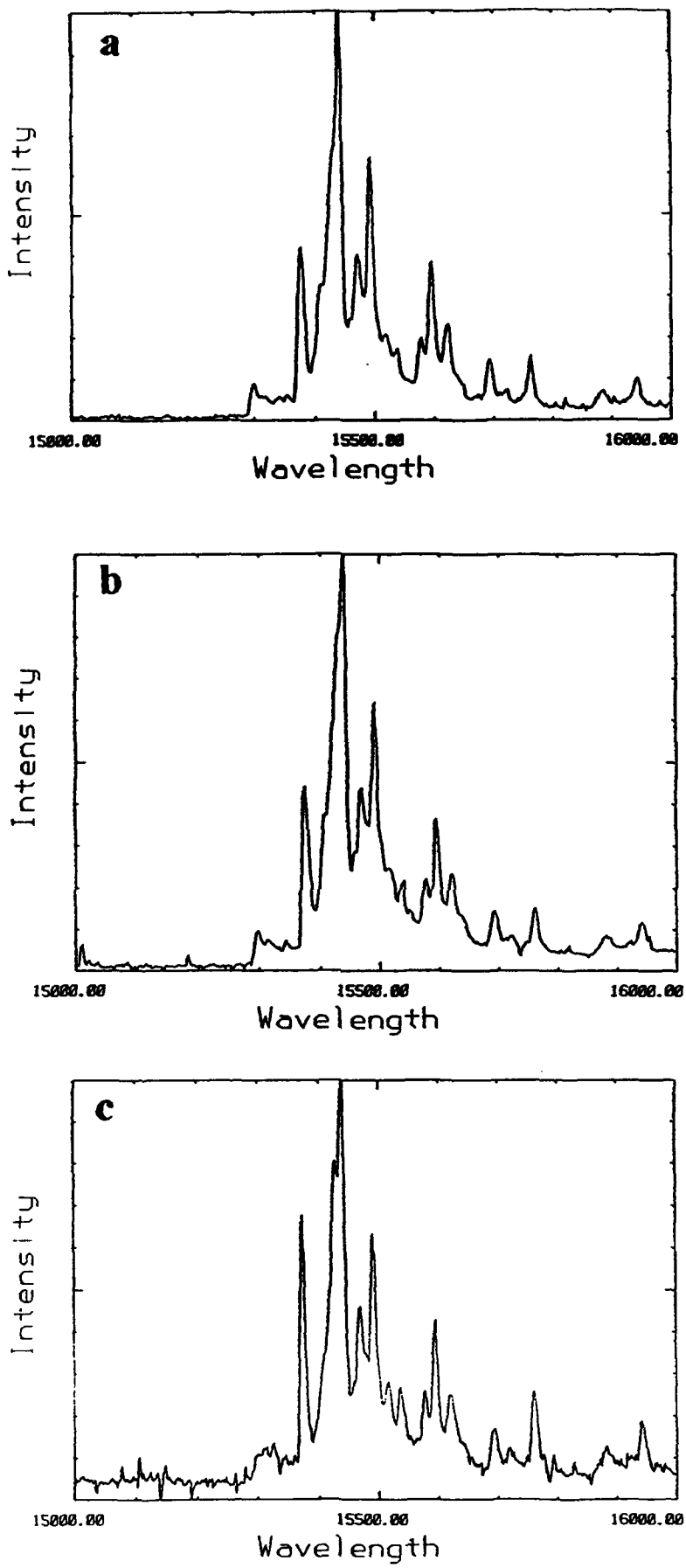
Fig. 3 The photoluminescence spectra of P4X samples recorded at 2 K in the range 1500 nm - 1600 nm using He-Ne laser (10 mW). (a) The reference spectrum of GaAs:Er as grown. In (b) and (c) the samples are diffused with Li at temperature 500 °C and 646 °C for 6 hours, respectively.
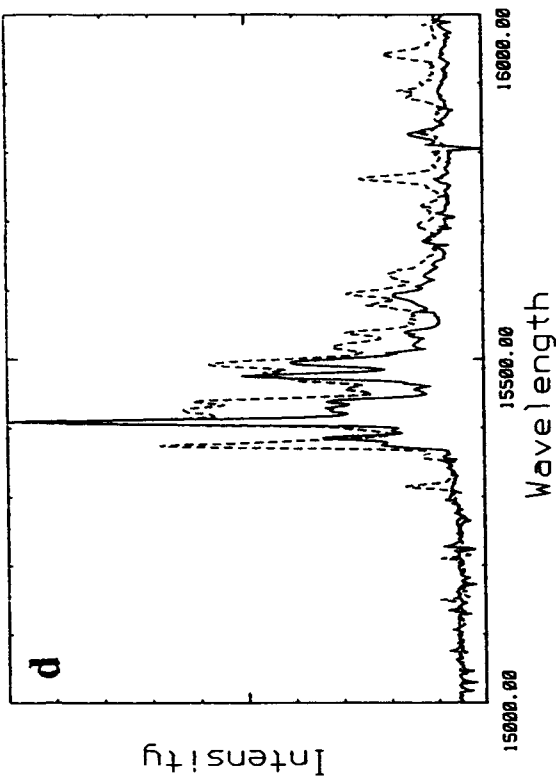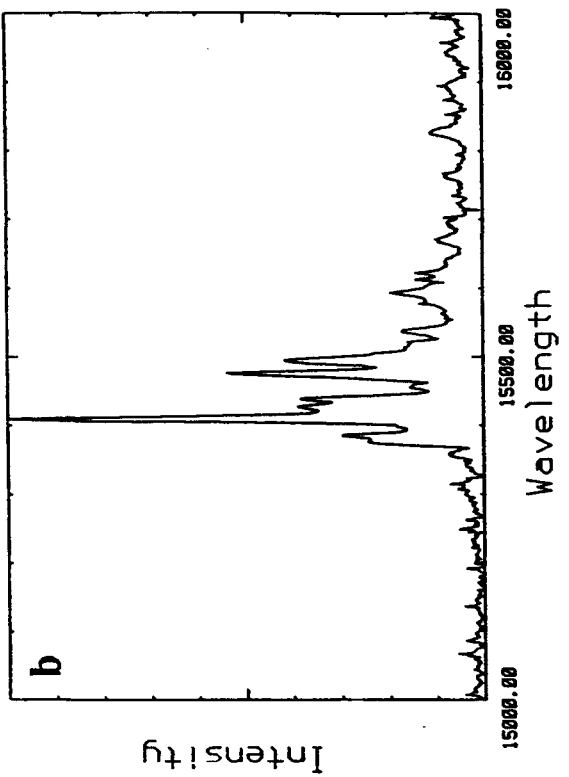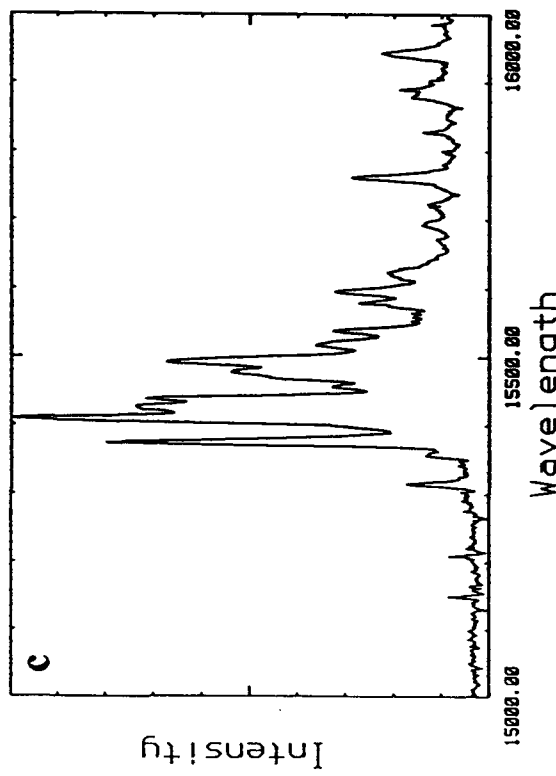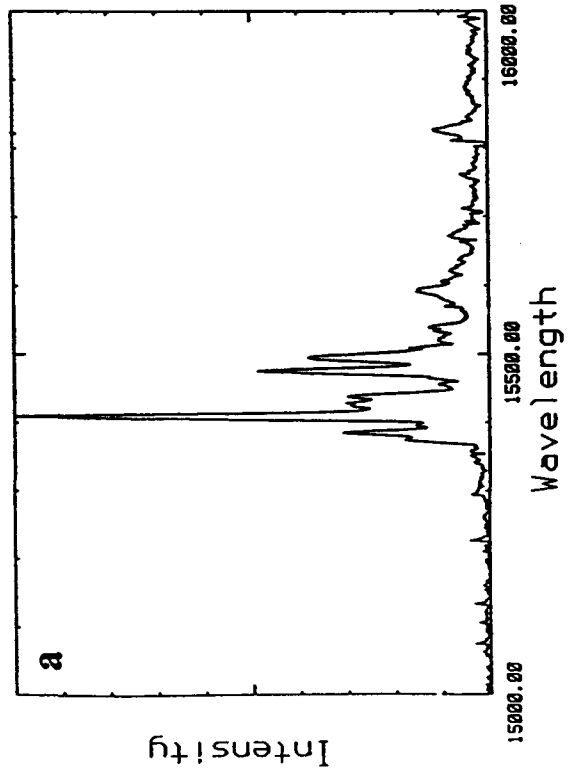
Fig. 4 The photoluminescence spectra of P52 samples recorded at 2 K in the range 1500 nm - 1600 nm using He-Ne laser (10 mW). In (a) the reference spectrum of GaAs:Er as grown, sample P52(3), (b) and (c) the samples are diffused with Li at temperature 500 °C (sample P52(2)) and 570 °C (sample P52(1)) for 6 hours, respectively. (d) is the overlapping of spectra (a) and (c).
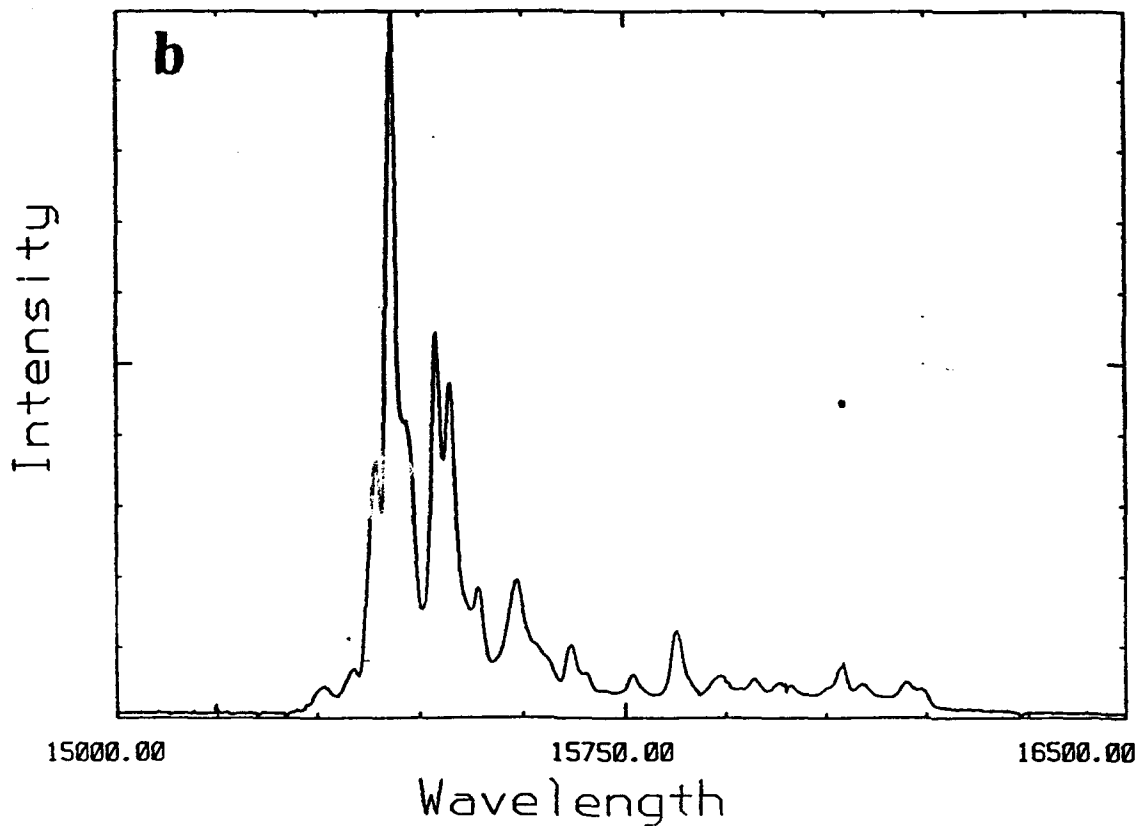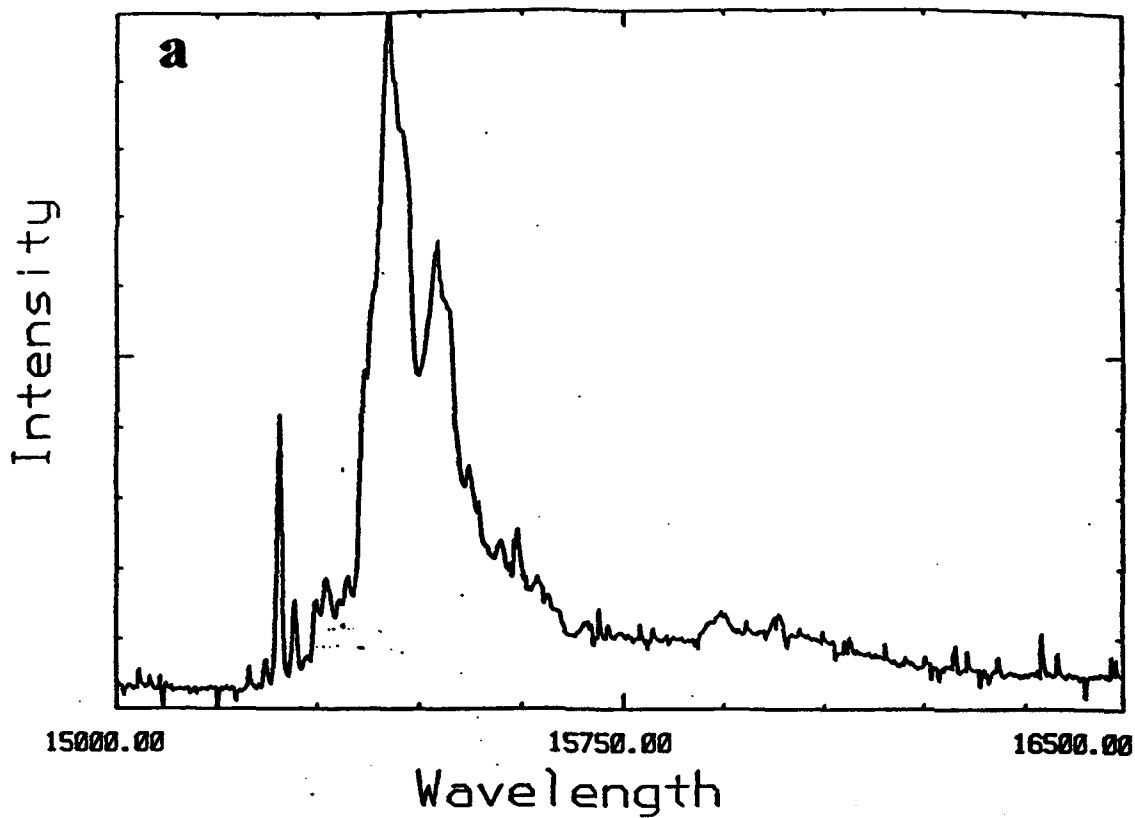
Fig. 5 The photoluminescence spectra of P52 samples recorded at 2 K in the range 1500 nm - 1600 nm using Ar⁺ laser at 514.5 nm (20 mW). In (a) sample P52(4) was diffused with Li twice at 646 oC for 6 hours and additionally at 802 oC for 1 hour, and (b) sample P52(3) as grown.

D. Summary and Conclusion

Photoluminescence spectra are reported in GaAs doped with Er and Li. A PL bands peaking at 1.41 eV involved a 0.11eV Cu_{Ga}-Li_i acceptor associate [5]. Similarly, a PL band peaking at 1.02 eV is ascribed to the 0.45 eV acceptor [10]. The strong band at 1.36eV is related to the 0.15 eV Cu acceptor [5], the shoulder at 1.34 eV is probably related to a double Li_{Ga} acceptor [6]. In the samples used in the study the Cu concentration is limited to accidental contamination during the heat treatment. The photoluminescence of Er co-doped with Li showed different changes in erbium spectrum for sample P4X and P52. The erbium spectrum of sample P4X doped with Li at 646^0C in Fig.3c, shows the different relative intensities of the emission lines in comparison with the samples as grown and doped with Li at 500^0C Fig.3a and b respectively. The line at 0.806 eV (1537.5 nm) increase twice in intensity comparing with as grown sample the other lines showed smaller increase in intensity. Spectra in Fig.4 a,-d, are for sample P52 grown at 500°C and doped with Li at different temperature. In figure 4d we overlap the spectrum (a) and (c) to shown the differences between these samples as grown and doped with Li at 570°C during 6 hours. PL spectra shown on Fig.5 a, b are recorded for samples P52(4) (a) and P52 (3). Sample P52 (4) was diffused with Li twice at 646°C for 6 hours and additionally at 802°C for 1 hour (Table II), sample P52 (3) as grown. The diffusion at 802°C reduced the intensity of Er emission and broadened the spectrum. In conclusion, we can say that the Li co-doping with Er in GaAs causes the difference in relative intensities of the emission peaks of Er. The biggest changes in spectra are observed for sample doped with Li at temperatures range 570°C to 650°C. More investigations must be done to understand the Li involvement in Er luminescent center.

References :

[1]   S. Larach, Proceeding of the International Conference on Luminescence, 1549, (1966)

[2]   P. N. Yocom and S. Larach, Extended Abstracts, Electrochemical Society, San Francisco Meeting, p. 15 (1965)

[3]   R. E. Shrader, S. M. Thomsen and P. N. Yocom, Extended Abstracts, Electrochemical Society, San Francisco Meeting May 9-13, p. 16 (1965).

[4]   M. E. Levy and W. G. Spitzer, J. Phys. Chem. Solids 6, 3223, (1973).

[5]   H. P. Gislason, Z.G. Wang, and B. Monemar, J. Appl. Phys. 58, 240, (1985).

[6]   a) H. P. Gislason, E.O. Sveinbjornsson, B. Monemar, and M. Linnarsson, Mat. Res. Soc. Symp. Proc. Vol. 163, 127, (1990). b) H.P. Gislason, B. Yang,L.S. Hauksson, J.T. Gudmundsson, M. Linnarsson, and E. Janzen, Materials Science Forum Vol.83-87, 985, (1992).

[7]   H. P. Gislason, B. Monemar, M.E. Pistol, P.J. Dean, D.C. Herbert, A. Kana'ah and B.C. Cavanett, Phys. Rev. B, 31, 3774, (1985).

[8]   H. P. Gislason, B. Monemar, M.E. Pistol, A. Kana'ah and B.C. Cavanett, Phys. Rev. B, 33, 1233, (1986).

[9]   P. J. Dean, Phys. Rev. B, 4, 2596, (1971).

[10]   H. J. Guislain, L. De Wolf, and P.Clauws, J. Electron. Mater. 7, 83, (1978).

IV. AC Electroluminescence of ZnS:Tm

A. K. Alshawa and H. J. Lozykowski, Department of Electrical & Computer Engineering, College of Engineering and Technology, Ohio University, Athens, Ohio 45701-2979

Abstract

The ac electroluminescence of thulium doped ZnS embedded in boric acid matrix was investigated. The El emission spectra were recorded as a function of voltage, frequency and temperature. The emission spectra at all temperatures show only strong sharp emission lines which were assigned to transitions within the 4f shell of Tm^{3+} ion. The emission spectra consisted of five groups of lines centered around 483 nm ($^1G_4 \rightarrow {}^3H_6$), 661.7 nm ($^1G_4 \rightarrow {}^3H_4$), 710.5 nm ($^3F_3 \rightarrow {}^3H_6$), 785 nm ($^1G_4 \rightarrow {}^3H_5$) and 805.5 nm ($^3F_4 \rightarrow {}^3H_6$). The emission intensities (I) of different peaks where recorded as a function of the applied voltage,V. The plot of natural logarithm of /emission intensity (I) versus $V^{-1/2}$ shows a straight line characteristic over many orders of emission intensity which indicates that the direct impact excitation mechanism is a dominant process. The experimental values of the 483 emission line (transition $^1G_4 \rightarrow {}^3H_6$) intensity versus the applied voltage were reproduced theoretically on the basis of the direct impact excitation mechanism.

Introduction

In recent years, there has been growing interest in rare earth doped ZnS due to their promising potential in obtaining thin film electroluminescent displays[l]. In particular several studies have been reported on the luminescence of Tm-doped ZnS. Thulium is of particular interest among all rare earth ions because it shows the most efficient cathodoluminescence (0.216 W/W) in the blue emission region around 478 nm, and the line centered around 800 nm has a power efficiency of 0.59 W/W as reported by Shrader, et al [2]. This means that if the electrons can be accelerated to ballistic energies, more efficient devices can be fabricated which use direct impact excitation of rare earth ions[3]. Tm^{3+} emission was first observed by Rothschild [4] who found emission lines centered at about 478 nm. Ibuki and Langer [5,6] reported four groups of emission lines around 365 nm, 480 nm, 650 nm and 800 nm. They investigated the optical absorption and emission spectra of the ZnS:Tm powder between 300 and 900 nm at different temperatures. Zimmermann and Boyn [7] applied the method of site selective excitation spectroscopy to Tm^{3+} ions in ZnS crystals. They were able to separate three different sites for which 4f-4f emission, excitation and absorption spectra were determined in the range of several 4f free-ion transitions. In another work [8], they studied the excitation and thermal quenching behavior of two Tm^{3+} centers. They also investigated [9,10] the excitation and deexcitation mechanisms of the blue emission of two Tm^{3+} centers and demonstrated that donor-acceptor pairs, involving the Tm centers as the donors, play an important role in the excitation process.

This paper reports the results of investigation of the ac electroluminescence of Tm-doped ZnS as a function of voltage, frequency and temperature. Strong electroluminescence emission (at all spectral regions) was observed at low temperature (8.5 K) as well as at room temperature (around 800 nm). At low temperature, the electroluminescence spectra of ZnS:Tm exhibit a fine structure that consists of a number of groups of narrow lines with a halfwidth of about 0.5 nm. By investigating the voltage dependence of the different emission lines, it has been found that the direct impact excitation mechanism is the dominant mechanism responsible for the electroluminescence.

Experimental

The power efficiency of the ZnS doped with Tm polycrystalline powder at 478 nm determined under cathode-ray excitation is 0.216 W/W, the highest yet reported for any rare-earth-activated phosphor especially in view of the very narrow emission bandwidth (6 nm) [2]. The preparation of the phosphors can be found elsewhere [11]. To obtain an electroluminophor from the Tm-doped ZnS powder, the insulating microcrystallites were coated with Cu_2S by immersing them in an aqueous solution of $CuCl_2$ (0.1 mol. %) at room temperature for 3 minutes [12]. Then, the mixture was filtered and the powder was dried at room temperature (or at 100°C). Next, the Cu_2S-coated ZnS:Tm microcrystallites were embedded into a meta-boric acid (HBO_2) glass matrix by heating the mixture of ZnS:Tm:Cu_2S and H_3BO_3 in weight proportion of 1:0.8, [13]. The mixture was heated to a temperature in the range of 170°C - 300°C (but it is not critical) to obtain the meta-boric acid glassy medium [13]. Boric acid is suitable host material for two reasons: first, it provides excellent transparency of emission in the visible region and second it has a low melting point (~169°C), which allows the powder luminophor to be embedded in a matrix, with a very small possibility that chemical reaction or induced thermal changes will occur in the ZnS:Tm phosphore. The electroluminescent cell, shown in figure 1, was prepared by pressing the glassy mixture at a temperature above the melting point, between
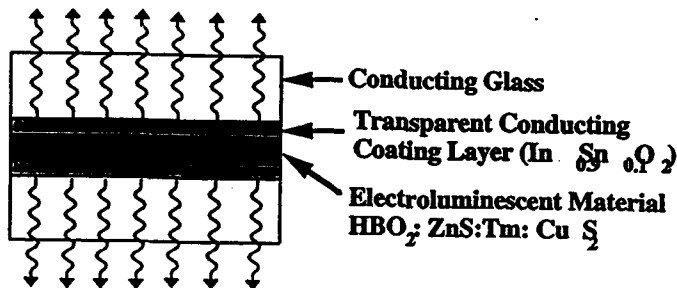

Fig. 1 Structure of the ZnS:Tm EL cell

$I_{483}/I_{661.7}$	$I_{487.8}/I_{661.7}$	$I_{659.7}/I_{661.7}$	$I_{662.7}/I_{661.7}$	$I_{671.8}/I_{661.7}$	$I_{701.2}/I_{661.7}$	$I_{805.5}/I_{661.7}$
0.85	0.37	0.38	0.87	0.44	0.05	0.41

Table I The emission intensity ratios of the main peaks to the peak at 661.7 nm at 10K.

two transparent conducting glasses (or conducting glass and stainless steal sheet). Electrical contacts to the conducting surfaces were made using silver paint. The thickness of the ZnS:Tm layer was about 50 μm (selected from a large number of samples) and the area of the cell was 4×4 mm^2. Some investigated samples were produced using the teflon spacer in order to control the thickness of the active layer. In order to exclude moisture, the samples were kept in a desiccator with a powerful drying agent (the samples can also be protected from the moisture by epoxy encapsulation).

A sinusoidal voltage generator was used as the excitation source. The sample was mounted on a cold finger cooled by a close-cycle helium cryostat down to 8.5 K. The emission was dispersed by a Jarrel Ash Model 78-490, 0.75 M, scanning monochrometor equipped with a 1180 grooves/mm grating. The signal was detected by a Hamamatsu R925 photomultiplier with a spectral response in the range of 400-930 nm. The total emission was detected by an RCA Model 7625 photomultiplier . The signal from the photomultiplier was fitted through a fast ORTEC 474 preamplifier to a single photon counting system, and then acquired by the ORTEC 7100 multichannel analyzer. The data were transferred to a computer for further manipulation and plotting.

Results and Discussion

The electroluminescence spectroscopic investigations of ZnS:Tm were performed in the wavelength range between 400 nm and 930 nm at different temperatures and for different applied voltages as shown in figures 2 and 4, respectively. The emission spectra show strong sharp emission lines of Tm^{3+} in the visible and near IR regions without any background emission attributed to the ZnS host. We observed five groups of emission lines centered around 483 nm, 661.7 nm, 710.5 nm, 785 nm and 805.5 nm which correspond to the transitions $^1G_4 \rightarrow {}^3H_6$, $^1G_4 \rightarrow {}^3H_4$, $^3F_3 \rightarrow {}^3H_6$, $^1G_4 \rightarrow {}^3H_5$, and $^3F_4 \rightarrow {}^3H_6$, respectively (all the spectra are normalized to the intensity value of the emission peak of 661.7 nm at 10 K, see Table I) . Figure 3 shows the energy levels scheme of Tm^{3+} ion assigned after [2,8]. Strong sharp emission lines have been observed at temperatures in the range of 8.5 - 290 K. In figure 2 (A, B, C, and D), the (a) curves show the spectra of ZnS:Tm recorded at 10 K and 270 volts. The spectrum in the region 475 - 500 nm (figure
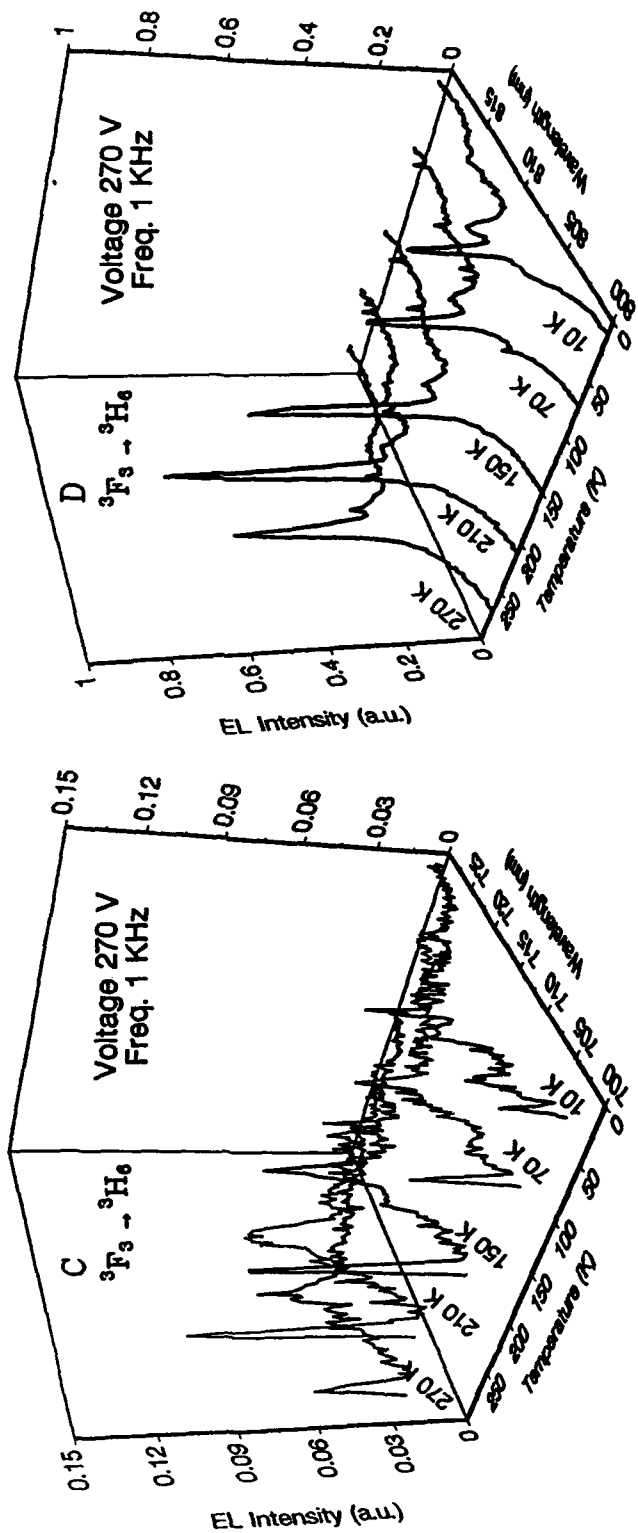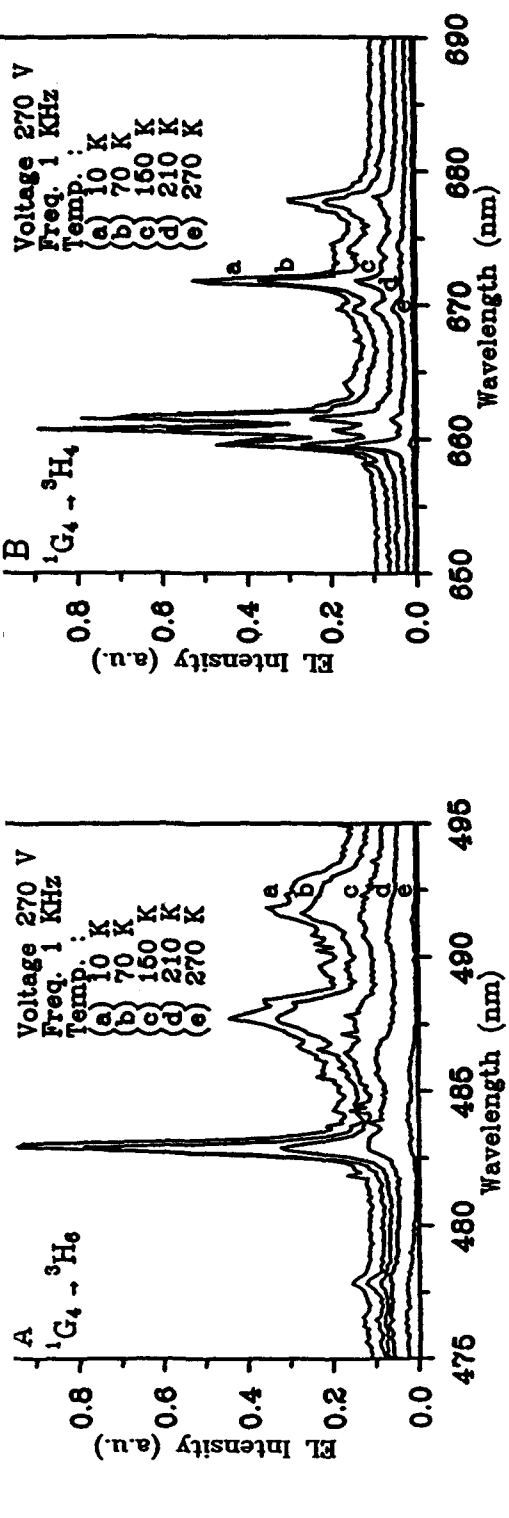
Fig. 2 AC EL spectra of Tm-doped ZnS for different temperatures at applied voltage 270

volts and frequency 1 kHz .(A) 476 - 493 nm (transition $^1G_4 \rightarrow {}^3H_6$), (B) 659 - 678 nm

(transition $^1G_4 \rightarrow {}^3H_4$), (C) 700 - 715 nm (transition $^3F_3 \rightarrow {}^3H_6$), and (D) 800 - 815

nm (transition $^3F_4 \rightarrow {}^3H_6$).
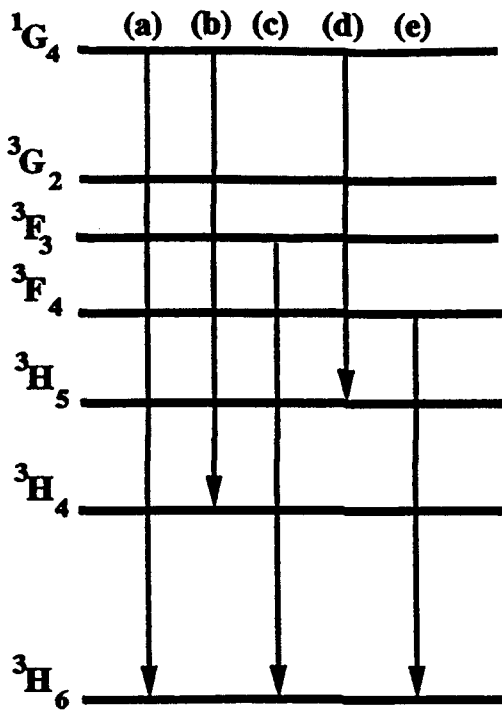
Fig. 3 Energy levels of Tm^{3+} corresponding to the emission regions of (a) 476 - 493 nm (b) 659 - 678 nm, (c) 700 - 715 nm, (d) 782 - 786 nm and (e) 800 - 815 nm.
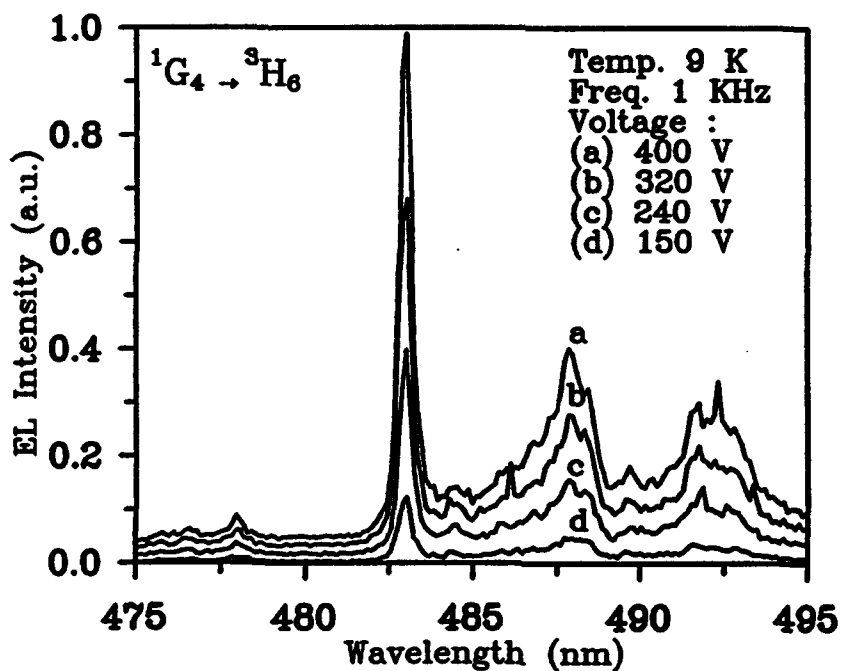
Fig. 4 AC EL spectra of Tm-doped ZnS (transition $^1G_4 \rightarrow {}^3H_6$) for different applied voltages at temperature 10 K and frequency 1 kHz.

2A, transition $^1G_4 \rightarrow ^3H_6$) reveals three major sharp peaks at 483 nm, 487 nm, and 492 nm. The emission line of 483 nm is narrower and about three times stronger than the other two peaks. The emission lines at 650 - 690 nm (figure 2B, transition $^1G_4 \rightarrow ^3H_4$) mainly consists of five very sharp peaks located at 659.7 nm, 660.7 nm, 661.7 nm, 671.8 nm and 678.2 nm. The emission line at 661.7 nm has the strongest intensity among other lines in this group as well as the other groups. Two small peaks were observed at 701.3 nm and 710.5 nm (figure 2C, transition $^3F_3 \rightarrow ^3H_6$). The two peaks are twenty times weaker than the emission lines at 661.7 nm and 483 nm. In the near IR region at 800-820 nm (figure 2D, transition $^3F_4 \rightarrow ^3H_6$) the emission line at 805.5 nm was four times weaker than the emission intensity of the 661.7 nm emission line. When the temperature is increased, another emission group centered at 785 nm (transition $^1G_4 \rightarrow ^3H_5$) appeared at 130 K and was observed. The peaks are sharp but very weak and disappeared with further increase of temperature above 170 K. Upon increasing the temperature up to room temperature, the emission intensities of all lines in the 483 nm and 661.7 nm regions. For the other two groups centered at 710.5 nm and 805.5 nm, the emission intensity increased with temperature until reaching the maximum at 210 K. The emission intensity of the 805.5 nm line at 210 K is five times larger than the emission intensity at 10 K. With further increase of temperature, emission intensities of all lines in the two groups decreased.

The Tm^{3+} in ZnS can form luminescence centers of several types, depending on its surroundings. All these centers may be differentiated by the symmetry or strength of the crystal field. On the other hand, this field defines the probabilities of transitions between sublevels of Tm^{3+} terms. Since the relative concentration of various types of centers depends on the preparation conditions, the different ZnS:Tm samples can differ strongly in the relative line intensity of the luminescence spectrum. It was report by [5, 6a,b] that Tm^{3+} mainly occupies a site with T_d symmetry.

The electroluminescence intensity of ZnS:Tm as a function of frequency (at constant voltage) was recorded in the frequency range 1-16 kHz. The intensities of all emission lines increased with frequency until reaching maximum at 7 kHz and then started decreasing with further frequency increase. For the 483 nm, 661.7 nm and 805.5 nm emission lines, intensities at 7 kHz were about three times larger than at 1 and 16 kHz.

The electroluminescence spectra were recorded at different applied voltages of 150 V, 240 V, 320 V, and 400 V. The intensities of all the Tm^{3+} emission lines increased with increase of the applied voltage as shown in figure 4 for the range 475 - 495 nm (transition $^1G_4 - ^3H_6$). To obtain information about the excitation mechanism of electroluminescence in ZnS:Tm, we have investigated the intensities of different emission lines as a function of the applied voltage. The integrated intensity of all emission lines was measured as a function of the applied peak voltages between 40 and 300 volts and for different temperatures in the range of 10 - 290 K. Figure 5 shows a plot of the logarithm of integrated intensity, I, versus the applied voltage, V, at temperatures 10 K and 290 K.

The emission intensity, I, of electroluminescence due to the impact excitation mechanism has often been described, following Alfrey and Taylor [14], by

$$I = I_o \exp(-bV^{-1/2})$$

where I_o and b are constants and V is the applied voltage. The plots of the logarithm of the intensity, I, against $V^{-1/2}$ for the integrated and single-line emissions at 8.5 K are shown in figure 6. These plots show that the emission intensity as a function of the applied voltage satisfies the above equation for several orders of magnitude. This proves that ZnS:Tm direct impact excitation mechanism by hot electrons dominates in the electroluminescence of ZnS:Tm crystals.

For more quantitative proof of the direct impact excitation mechanism of electroluminescence, we performed the numerical calculation of the electroluminescence intensity as a function of applied voltage. If the direct impact of accelerated electrons with Tm^{3+} centers is the excitation mechanism responsible for the electroluminescence in $ZnS:Tm^{3+}-Cu_2S$ system, then the theoretical model proposed by [3,15,16,17] gives the expression for the electroluminescence intensity of the Stark multiplet as:

$$I = \eta_q nN \int f(\varepsilon, E)\varepsilon^{1/2}\sigma(\varepsilon, \varepsilon_r)d\varepsilon$$

where

$$f(\varepsilon, E) = \varepsilon^{-a+0.5} \exp(-b\varepsilon)$$

$$a = (E_p - eE\lambda)(2E_p + eE\lambda)^{-1}$$

$$b^{-1} = 2/3 \, eE\lambda + 1/3((eE\lambda)^2/E_p)$$
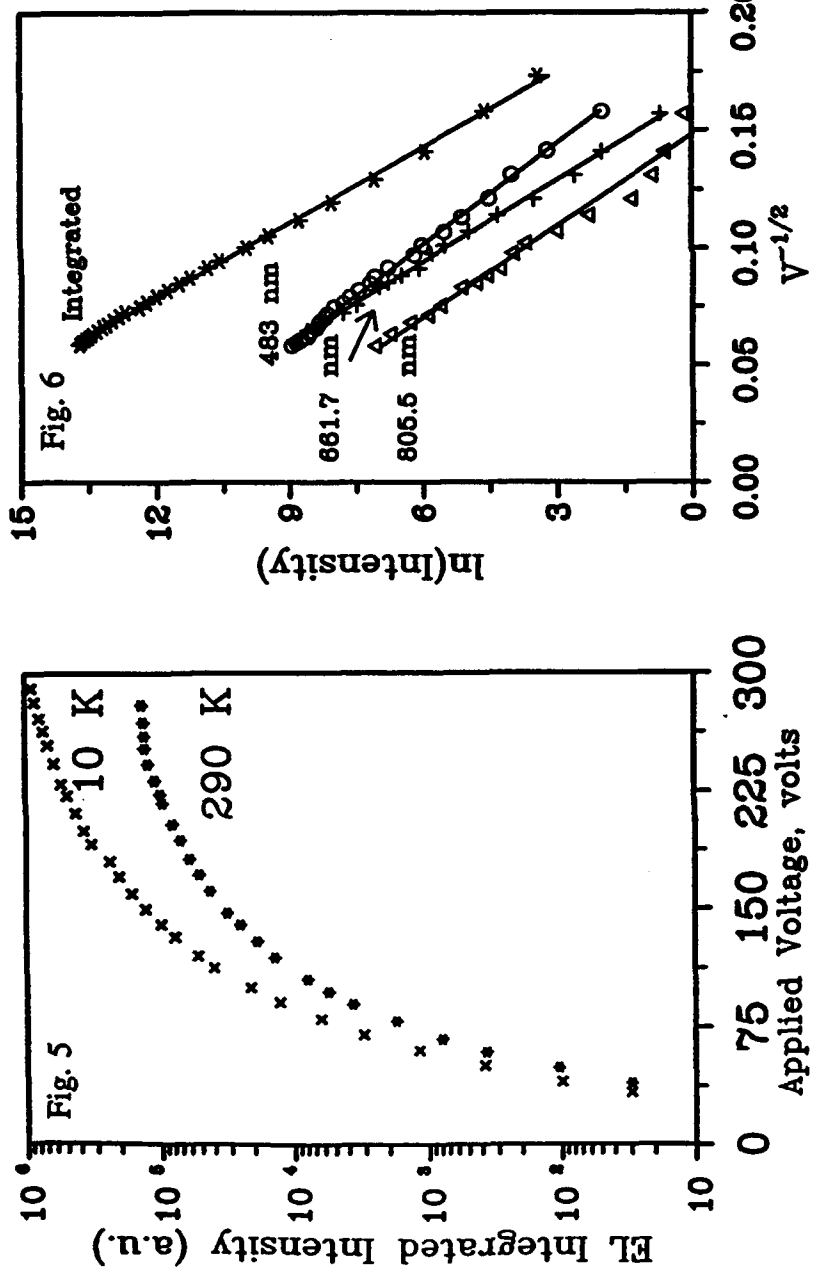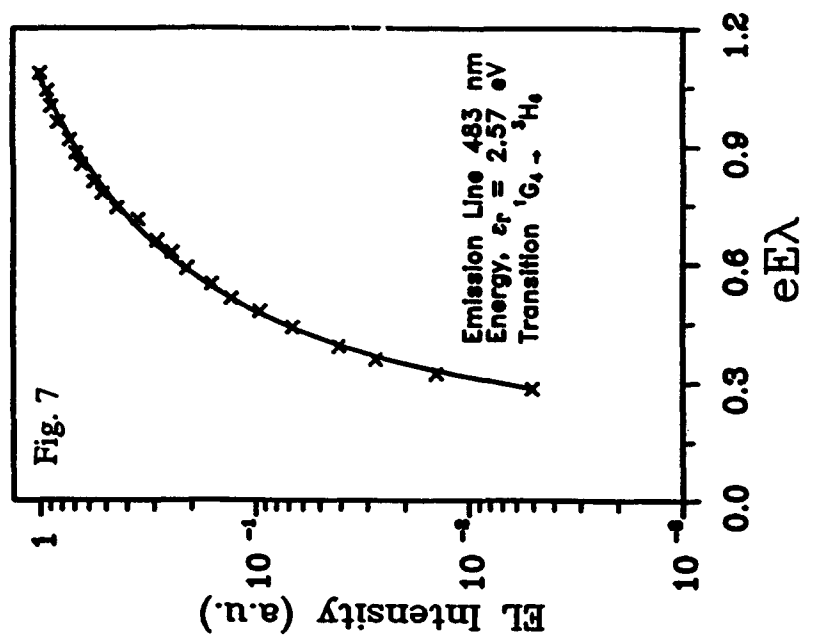
Fig. 5 Integrated emission intensity versus applied voltage at a temperature of (a) 10 K and (b) 290 K and frequency 1 kHz.

Fig. 6 Logarithm of the emission intensity versus the applied voltage ($V^{-1/2}$). (a) Integrated intensity (all lines), (b) 483 nm (transition $^1G_4 \rightarrow {}^3H_6$), (c) 661.7 nm (transition $^1G_4 \rightarrow {}^3H_4$), and (d) 805.5 nm (transition $^3F_4 \rightarrow {}^3H_6$) at temperature 8.5 K and frequency 1 kHz.

Fig. 7 Comparison of Experimental (star) and calculated (solid line) Intensities versus eEλ, for ZnS:Tm emission line of 483 nm (transition $^1G_4 \rightarrow {}^3H_6$).

η_q is the quantum efficiency, n is the density of hot electrons, N is the density of luminescence centers, f (ε, E) is the Baraff's distribution function of the electron energy, ε_Γ is the energy of the Γ multiplet of the Tm^{3+} ion, e is the electron charge, E is the electric field in ZnS, and λ is the electron mean free path . E_p is the optical (LO) phonon energy (0.04 eV) in ZnS, assuming that the hot electrons are scattered by the optical phonons of the ZnS lattice.

The analytical expression for the inelastic scattering cross sections based on the Born approximation considering the coulomb interaction between hot free electron and the 4f electrons of the rare earth ion was derived by Yu and Shen [18]. The impact cross section corresponding to the transition from i state to f state is given by

$$\sigma(\varepsilon, \varepsilon_\Gamma) = \frac{18\pi^2 m e^2 h^2 c^3}{n(n^2+2)^2 e^3_\Gamma} \frac{1}{\varepsilon} [\ln \frac{\sqrt{\varepsilon} + (\varepsilon - \varepsilon_\Gamma)^{\frac{1}{2}}}{\sqrt{\varepsilon} - (\varepsilon - \varepsilon_\Gamma)^{\frac{1}{2}}}]^{\frac{1}{2}} \frac{g_f}{g_i} A_{fi}$$

where m is the mass of the electron, c is the speed of light in vacuum, n is the refractive index of ZnS, ε is the energy of the incident electrons, ε_Γ is the energy corresponding to the transition from the final state f to the initial state i, $g_{i,f}$ is the degeneracy of the initial and final states and A_{fi} is the electric dipole transition probability.

To compare with the experimental results, the above calculations were carried out for the emission line of 483 nm which corresponds to transition $^1G_4 \rightarrow {}^3H_6$. The threshold energy of this transition, ϵ_Γ is 2.57 eV, E_p is 0.04 eV and the degeneracy of the initial and final state are g_f = 9 and g_i = 13 respectively. The refractive index, n, of ZnS is 2.4 and the electron mass, m, is the free-electron mass. The calculated intensity (solid line) with the experimental points are shown in figure 7. The mean free path of the electron, λ, was found to be about 5.5 nm, and for the best fit, eEλ is in the range 0.3 - 1.1 eV (which corresponds to the electric field in the range 1.33 x 10^7 - 9.86 x 10^7 V/m). The computed intensity increase with eEλ follows the experimental data well. More quantitative considerations cannot be drawn because we do not know the exact value of the electrical field in the system, the concentration of the RE^{3+} Centers and the quantum efficiency η_q.

Conclusion

The study of the ac electroluminescence of $ZnS:Tm^{3+}$ embedded in boric acid matrix are presented. The electroluminescence spectra at low and room temperatures show strong sharp emission lines of Tm^{3+}, in the visible and IR regions without any background emission attributed to the ZnS host semiconductor. The direct impact excitation mechanism has been proved to be the dominant mechanism responsible for the electroluminescence in the $ZnS:Tm^{3+}$-Cu_2S system. In our current going research[1], the powder ZnS:Tm luminophore was embedded in acrylic binder as well as boric acid. Strong blue electroluminescence emission was observed at room temperature and is visible in an illuminated room. These results show the potential for a blue electroluminescence large area displays made from powder $ZnS:Tm^{3+}$ luminophor.

---

[1] The results will be published elsewhere

References

1. V. P. Singh, and J. C. McClure, Proceedings of the Sixth International Workshop on Electroluminescence, El Paso, Texas, 1992 (Cingo Puntos Press, El Paso, Texas, 1992), and references therein.

2. R. E. Shrader, S. Larach, and P. N. Yocom, J. Appl. Phys., **42** (11) (1971) 4529.

3. H. J. Lozykowski, Springer Proceeding in Physics, **38** (1989) 60.

4. S. Rothschild, *In Proceedings of the International Conference on Solid-State Physics in Electronics and Telecommunication, Brussels*, 1958 (Academic, New York (1960) **4** 705.

5. S. Ibuki and D. W. Langer, Appl. Phys. Lett. **2** (5) (1963) 95.

6. a) S. Ibuki and D. Langer, J. Chem. Phys., **40** (3) (1969) 796. b) Y. Charreire and P. Porcher, J. Electrochem. Soc. : Solid State Science And Technology, **130**, No. 1, (1983) 175

7. H. Zimmermann, and R. Boyn, Phys. Stat. Sol. (b) **130** (1985) 315.

8. H. Zimmermann, and R. Boyn, Phys. Stat. Sol. (b) **135** (1986) 379.

9. H. Zimmermann, and R. Boyn, Phys. Stat. Sol.. (b) **139** (1987) 533.

10. H. Zimmermann, and R. Boyn, Phys. Stat. Sol. (b) **163** (1987) 163.

11. S. Larach and P. N. Yocom, U.S. Patent No; 3459667.

12. T. Minami, M. Komano, H. Nanto, and S. Takata, Jap. J. Appl. Phys. **25** (12) (1986) L961.

13. E. Walentynowicz and M. A. Czajkowski, Phys. Stat. Sol. **57** (a) (1980) K21.

14. G. F. Alfrey and J. B. Taylor, Brit. J. Appl. Phys. (Supt) **4** (1955) 594.

15. H. J. Lozykowski, Solid Stat. Com. **66** No. 7 (1988) 755.

16. D. C. Krupka, J. Appl. Phys., **43** (2) (1972) 476.

17. I. Szczurek, H. J. Lozykowski and T. Szczurek, J. Lumin., **23** (1981) 315

18. J. Yu and Y. Shen, J. Phys. C: Solid Stat. Phys. **21** (1988) 3381.

Kinetics of luminescence of isoelectronic rare-earth ions in III-V semiconductors

H. J. Lozykowski

Department of Electrical and Computer Engineering, and Condensed Matter & Surface Sciences Program,
Ohio University, Athens, Ohio 45701

In this work we have developed a kinetics model of energy transfer from the host lattice to the local-ized core excited states of rare-earth isoelectronic structured traps (REI traps). The presence of low-lying empty core orbitals in rare-earth impurities introduces new excitation and recombination phenom-ena. To adequately describe the energy transfer to a REI trap, the buildup and decay kinetics of rare-earth luminescence, we consider six separate states of the REI impurity (unoccupied, electron occupied, electron occupied excited, exciton occupied, excited electron occupied, and excited exciton occupied). The energy-transfer processes occur through an Auger mechanism where the recombination energy of the bound electron with a free hole is transferred nonradiatively to the core states, or energy can be transferred from the bound exciton on a REI trap to the core states. If the initial and final states are not resonant (in both mechanisms), the energy mismatch must be accommodated by emission or absorption of phonons. Furthermore we discuss details of several quenching processes, which are incorporated into the kinetics equations. We derive two sets of differential equations for semi-insulating and n-type semi-conductors governing the kinetics of rare-earth luminescence. Equations have been solved by a numeri-cal method to derive the time dependence of the rise and decay kinetics as a function of excitation inten-sity. The numerically simulated luminescence rise and decay times show a good overall quantitative agreement with experimental data obtained for InP:Yb, over a wide range of generation rates.

I. INTRODUCTION

The investigation of the luminescence properties of rare-earth-doped III-V and II-VI semiconductors is of great interest both from the scientific and application points of view. The scientific interest is related to the uniqueness of optical and electrical properties of rare-earth impurities in semiconductor hosts. It is well known that rare-earth luminescence depends only slightly on the nature of the host and on the temperature. The $4f$ orbit-als of rare-earth ions incorporated in semiconductors are so deeply buried within the electronic shell that the ener-gy levels of the $4f^n$ configuration are only slightly per-turbed compared to free ion energy levels. The electronic structure of the rare-earth luminescence centers and their electrical activities as well as their indirect photolumines-cence and electroluminescence excitation mechanisms, are still not well understood. Among the rare-earth-doped III-V semiconductors, InP:Yb has been the most extensively studied.[1-9]

Ytterbium in InP replaced indium on a substitutional site,[10,11] and acts as an isoelectronic trap. It was original-ly proposed by Whitney et al.[5(a)] and confirmed by others[6,7,12(a)] that the Yb ion creates an electron trap at 30 meV below the bottom of the conduction band. Re-cently, admittance spectroscopy[12(a)] was used to identify the electrical activity of Yb in n- and p-type InP. It was found that Yb in InP creates a hole trap at 50 meV above the valence band, and an electron trap at 29 meV below the conduction band. The 50-meV trap may be related to other impurities unintentionally incorporated into the crystal. This interesting result required confirmation us-ing a sample grown by a more refined crystal growth

technique to ensure the high purity of the crystal. Re-cently it has been reported that Er in InP [Ref. 12(b)] and Yb in GaAs [Refs. 12(c) and 12(d)] introduced electron traps at 60 and 63 meV, respectively, below the conduc-tion band. Colon et al.[12(e)] investigated low-temperature photoluminescence, selectively exited luminescence, and deep-level transient spectroscopy on erbium-implanted GaAs. Conclusions of these measurements is that Er im-plantation introduces in GaAs two hole traps at 84 and 340 meV above the valence band. Several authors[5(a),5(b),6,8,9,13(a),13(b)] have proposed a model that involves recombination of electron-hole pairs at the rare-earth (RE) traps to explain the excitation of RE core states.

In this paper we discuss only the structured isoelect-ronic traps in III-V semiconductors introduced by triply charged rare-earth ions replacing the element from column III (or another more complex RE isoelectronic traps). Furthermore, we develop the luminescence kinet-ic models that describe the energy-transfer and recom-bination processes. The presence of low-lying empty core orbitals in rare-earth impurities introduces new excita-tion and recombination phenomena, which will be dis-cussed in detail. The RE luminescence rise time of the rare-earth-doped semiconductors, excited indirectly above the band gap, contain information about the energy-transfer processes from the host to the $4f^n$ elec-tron system. It is shown that the study of the rise time at different temperatures, excitation intensities, and excita-tion pulse durations can provide important information about the energy-transfer, radiative, and nonradiative processes, respectively. The numerically simulated luminescence rise and decay profiles show a good quanti-

tative agreement with experiment over a wide range of generation rates. Finally, the possible quenching mechanisms and the temperature dependence of rare-earth luminescence are discussed.

II. THEORETICAL FORMULATION

It is well known that isoelectronic impurities in semiconductors produce bound states in the forbidden gap, binding an electron or a hole.[14,15] An isoelectronic center can form bound states because of a short range central-cell potential. According to Thomas,[15] the primary factors affecting the binding potential are the electronegativity and the size differences between the impurity and the host ion which it replaces. It is found experimentally that only very large atoms or very small atoms produce isoelectronic traps because they create large lattice distortion induced by the substitution. Thomas and co-workers[16,15] have pointed out that to create a large binding potential, the substituted atom must generate a noticeable change in the local properties of the lattice. This is likely to produce an unfavorable free energy of the solution, and hence a rather low solubility can be observed. For instance, the maximum concentration seen for bismuth in GaP was less than 10^{18} cm^{-3}.[17] Low solubility is also observed for rare earths in III-V semiconductors.[18]

Allen[19] proposed different binding mechanisms for isoelectronic traps. According to Allen the isoelectronic impurity potential does not come from a pseudopotential difference of two isoelectronic atoms. Other possible sources are the spin-orbit coupling, and the strain field in the close vicinity of the impurity due to the size difference between the impurity and the host atom which it replaces. The main results of this theory are that the perturbing potential at an isoelectronic impurity may be attracted simultaneously to both the electron and the holes, so bound exciton states can occur without bound single-particle states. Baldereschi and Hopfield[20] have proposed a theory of isoelectronic traps assuming that the short-range potential arises from core differences, including spin-orbit interaction between the dopant atom and the host atom it replaces. The relaxation of the host crystal around the impurity as well as the screening model considered appear to be important for the binding energy. However, discrepancies between experimental binding energies and those calculated from the differences in the atomic pseudopotentials are observed. Excellent reviews of existing theories and experimental data of isoelectronics impurities were given by Baldereschi[21] and Dean[22] and Czaja.[23] In GaP two isoelectronic traps have been extensively investigated, namely a nitrogen electron trap, and a bismuth hole trap formed by substituting Bi and N for phosphorus.[22] In the direct-band-gap III-V semiconductors, isoelectronic impurities have been investigated only in InP doped with bismuth.[24,25] The neutral Bi, in a P site, creates a hole trap, and the isoelectronic complex (Bi,X)-(Bi,X) bound-excitonic molecules.[25] In II-VI semiconductors, ZnTe doped with oxygen-electron traps, and CdS doped with tellurium hole traps, were investigated in detail.[23]

It is notable that all isoelectronic impurities discussed

above involve substitutions on the anion sites. The previous investigation[26] of cationic isoelectronic substituent (Mg, Ca, Sr, Ba) in ZnSe and ZnTe found no evidence of the presence of isoelectronic traps. A strong photoluminescence (PL) was reported recently from Mg-doped ZnSe [Refs. 27(a) and 27(b)] and ZnS (Ref. 28) which may arise from a new isoelectronic center generated by magnesium. We observed[27] sharp emission with a half-width of 16–60 meV (for $Mg_xZn_{1-x}Se$, $x=0.04$), as required for exciton transitions at low temperatures. Furthermore the PL characteristics shift dramatically from deeper extrinsic emission in ZnSe to be dominated by narrow near-band-gap emission at all temperatures in the range 2–300 K in $Mg_{0.04}Zn_{0.96}Se$. The temperature dependence of the energy position of this peak follows the expected behavior for a free exciton transition in ZnSe. This peak remains strong in the PL spectrum all the way up to room temperature. This kind of behavior is not usually observed for bound exciton transitions related to neutral donor or acceptor centers. However, this behavior is typical for excitons bound to isoelectronic traps for which the dominant decay mode is radiative. The presence of the third electronic particle in the first two cases, but not in the third, was shown to introduce a dominant Auger decay mode for the bound exciton. In the Auger quenching, all the recombination energy is transferred to this third electronic particle that is expelled deep into the conduction (electron) or valence band (hole), respectively.

The striking feature of excitons bound to isoelectronic traps is a long luminescence decay time, ranging from a few hundred to a few thousand nanoseconds.[25,29–33] The lifetimes of a neutral donor or acceptor bound excitons in direct-gap semiconductors are in the range of nanoseconds. For example the decay time of excitons bound to neutral donors or acceptors in InP are 0.5 and 1.5 ns, respectively.[34(a)] The lifetime of an exciton bound to a neutral donor in GaAs is 1.07 ns.[34(b)] In contrast the lifetime of an exciton bound to a Bi isoelectronic trap in InP is about 200 ns.[25]

Table I shows that the outer electron configurations of RE^{3+} ions are the same $(5s^25p^6)$. If the rare-earth ions replace the element from column III in III-V compounds that are isovalent concerning outer electrons of RE^{3+} ions (see Table I), they create isoelectronic traps in III-V semiconductors. This does not require association with other near distant charge compensating lattice defects or impurities, as is so common in II-VI semiconductors. The above conclusion is supported by the fact that the atomic covalent radii (ionic RE^{3+}) for all rare earths are bigger than atomic radii of Ga and In that they are replacing. Pauling's electronegativity of rare-earth elements is in the range of 1.1–1.25, and is smaller than Ga (1.81) and In (1.78) for which it substitutes. We known from different investigations that Yb substituted for In in InP behaves according to the above experimental rule and creates an isoelectronic trap. We have evidence that the other RE ions in III-V semiconductors can occupy different sites (not only substitutional). The rare-earth isoelectronic trap must not necessarily be the "pure" substitutional center. if the rare-earth ions are very active

TABLE I. Electron configuration of RE atoms, RE³⁺ ions (and some elements), ionic, covalent radii, and electronegativity.

Element	Electron configuration	Electron configuration RE³⁺ & others	Ionic radius (Å) charge 2⁺	3⁺	Covalent radius (Å)		Electronegativity a: (Pauling's)
Cerium	$4f^25s^25p^66s^2$	$4f^15s^25p^6$		1.02	1.65		1.12[a]
Praseodymium	$4f^35s^25p^66s^2$	$4f^25s^25p^6$		1.00	1.65		1.13[a]
Neodymium	$4f^45s^25p^66s^2$	$4f^35s^25p^6$		0.99	1.64		1.14[a]
Promethium	$4f^55s^25p^66s^2$	$4f^45s^25p^6$		0.98	1.63		1.13[a]
Samarium	$4f^65s^25p^66s^2$	$4f^55s^25p^6$		0.97	1.62		1.17[a]
Europium	$4f^75s^25p^66s^2$	$4f^65s^25p^6$		0.97	1.85		1.20[a]
Gadolinium	$4f^75s^25p^65d^16s^2$	$4f^75s^25p^6$		0.97	1.61		1.20[a]
Terbium	$4f^95s^25p^66s^2$	$4f^85s^25p^6$		1.00	1.59		1.20[a]
Dysprosium	$4f^{10}5s^25p^66s^2$	$4f^95s^25p^6$		0.99	1.59		1.22[a]
Holmium	$4f^{11}5s^25p^66s^2$	$4f^{10}5s^25p^6$		0.97	1.58		1.23[a]
Erbium	$4f^{12}5s^25p^66s^2$	$4f^{11}5s^25p^6$		0.96	1.57		1.24[a]
Thulium	$4f^{13}5s^25p^66s^2$	$4f^{12}5s^25p^6$		0.95	1.56		1.25[a]
Ytterbium	$4f^{14}5s^25p^66s^2$	$4f^{13}5s^25p^6$		0.94	1.74		1.10[a]
Gallium	$3d^{10}4s^24p$			0.62	1.26	1.13[b]	1.81[a]
Indium	$4d^{10}5s^25p$			0.81	1.44	0.99[b]	1.78[a]
Zinc	$3d^{10}4s^2$		0.74		1.23	0.91[b]	1.65[a]
Cadmium	$4d^{10}5s^2$		0.97		1.48	0.83[b]	1.69[a]
Mercury	$5d^{10}6s^2$		1.10		1.49	0.79[b]	2.00[a]

[a]Elemental electronegativity in tetrahedrally coordinated environments (Ref. 35).
[b]Reference 36.

chemically, they can create a more complex center involving other impurity or native defects. The recent experimental data discussed in Sec. I shows that RE ions introduce electron or hole traps in III-V semiconductors, and we do not have evidence that RE ions act as donors or acceptors. The important roles of oxygen on RE luminescence have been discussed recently. Clearly we need more experimental and theoretical investigations devoted to rare-earth impurities to gain knowledge about the electrical activities of RE ions in semiconductors.

The rare-earth isovalent traps that we call isoelectronic "structured" impurities[17] possess unfilled $4f^n$ core shells. The luminescence structure arises from intraconfigurational f-f transitions in the core of the isoelectronic "structured" impurities. The presence of low-lying empty core orbitals in rare-earth impurities introduces new excitation and recombination phenomena (which will be discussed in detail below). It distinguishes these impurities from the "simple" impurities (from the main group of elements of the Periodic Table). The "simple" impurity typically introduces only effective-mass-like states in the forbidden gap of the host crystals. According to Robbins and Dean,[17] the formation of a bound state at the structured cationic isoelectronic impurities is fairly common, which is in contrast to the situation normally found for the anionic substituent in semiconductors discussed above.

The isoelectronic trap can be attractive either for electrons or for holes, and according to Allen's theory it can bind the exciton as a single entity. Since there is no charge involved, the isoelectronic center forms the bound states by a short-range central-cell potential. It is generally accepted that the formation of bound states is a specific property of the impurity and lattice combinations

discussed above. After an isoelectronic trap has captured an electron or a hole, the isoelectronic trap is negatively or positively charged, and by Coulomb interaction it will capture a carrier of the opposite charge, creating a bound exciton.

It has been well established that the "simple" isoelectronic traps can act as very efficient centers for radiative recombination in semiconductors. The structured isoelectronic cationic substitutional impurities (trivalent RE³⁺) in many phosphors lead to efficient characteristic luminescence.[17] The trivalent rare-earth ions also create structured substitutional isoelectronic traps (REI trap) in some III-V semiconductors.

The "simple" isoelectronic center in III-V materials can exist in three possible states (to be identified later), instead of two as in the case of the Shockley-Read-Hall (SRH) recombination model.[32] In the case of rare-earth isoelectronic traps the kinetics model is even more complicated because of energy-transfer processes between the localized state in the forbidden gap of the host, and the localized core states of structured isoelectronic impurities. There are three possible mechanisms of energy transfer. The first is the energy-transfer process from excitons bound to "structured" isoelectronic centers to the core electrons. It takes place as a result of the electrostatic perturbation between the core electrons of the "structured" impurity and the exciton effective-mass-like particle.[17] This model is a modification of the Shaffer-Williams model of intrapair energy transfer to "structured" isoelectronic traps.[37] The second mechanism is transfer of energy to the core electrons involving the "structured" isoelectronic trap occupied by electron (hole) and free hole (electron) in the valence (conduction) band. The third mechanism is the transfer through an in-

elastic scattering process in which the energy of a free exciton near a "structured" trap is given to the localized core excited states.[17] If the initial and final states are not resonant, the energy mismatch must be distributed in some way, e.g., by phonon emission or absorption.[17,59(b)] According to Robbins and Dean,[17] if the atomic core excitations are strongly coupled to the host phonons, the energy-transfer probability is likely to be higher. Strong phonon coupling may also be desirable in ensuring that relaxation down the ladder of core excited states occurs quickly, thus preventing back transfer. However, for efficient radiative recombination, the phonon coupling should not be strong, in order to prevent core deexcitation by nonradiative multiphonon emission. In this regard the rare-earth "structured" impurity seems to be ideal.

III. KINETIC MODELS

The SRH model that allows for only two possible states fails to give the correct general description of recombination kinetics of isoelectronic traps.[32] The above discussion shows that isoelectronic impurities, both "simple" or "structured," can act as efficient centers for radiative recombination. The "simple" traps can exist in three possible states: (1) empty, (2) electron (hole) occupied, and (3) exciton occupied. In the case of RE^{3+} "structured" isoelectronic centers, the model is more complicated because the center can exist in six possible states. Furthermore the energy-transfer processes between the localized states in the forbidden gap and core states complicate the model. In our model, we assume that the isoelectronic trap is an electron trap such as Yb^{3+} in semi-insulating (SI) InP. When isoelectronic traps are present in n- or p-type materials the model will be different, especially at high temperature, and must be modified separately for n- and p-type material. The asymmetry between n- and p-type semiconductors results from the fact that the isoelectronic center binds only an electron (hole). Thus in an n-type material, a fraction of the isoelectronic traps will be occupied by electrons even before the sample is excited, while in p-type material all the isoelectronic electron centers will be empty.[39,40] At low temperature (~4 K) there will be no difference between the n, p, or SI samples because the electrons or holes will be frozen. The donor and acceptor will act as "shunt" recombination centers. Figures 1–5 show the symbols' definitions, and physical models used in the kinetic analysis of the energy-transfer processes and recombination involving "structured" isoelectronic impurities. The proposed model accounts for energy transfer from the host to the core states through localized states in the forbidden gap, and for the dependence of the rise time on excitation intensities and temperature, including nonradiative recombination centers. In cases of n- or p-type semiconductors, we incorporate donor or acceptor centers to the model [see Figs. 1(d) and 1(e)].

By fitting the calculation to the experimental data, we can estimate important parameters related to energy transfer from the lattice to RE^{3+} centers, the Auger processes, temperature quenching mechanisms, and other
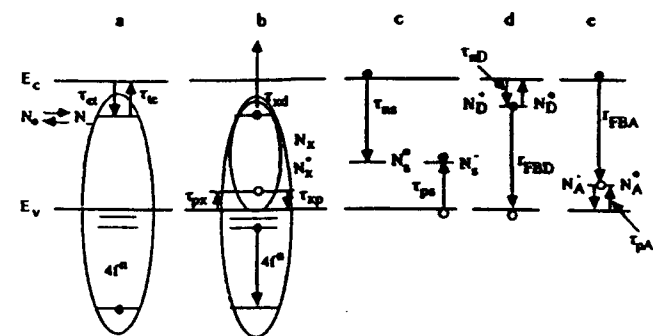

FIG. 1. Schematic diagram of recombination, trapping (thermalization), and exciton formation and dissociation processes involving structured rare-earth isoelectronic electron traps (represented by ellipse) with the atomiclike $4f^n$ core states. (a) Trapping (liberation) $\tau_{et}(\tau_{te})$ of electron on REI traps. (b) Formation of exciton (shadow ellipse) by hole capture (τ_{px}); liberation of hole (τ_{xp}); dissociation of exciton (τ_{xd}) on the REI trap. (c) Shunt electron (hole) trapping time τ_{es} (τ_{ps}). (d) and (e) The trapping times for electron, τ_{nD}, and hole, τ_{pA}, by a donor (ionized), and an acceptor (neutral), respectively, and bound electron (hole) to free holes (electrons) recombination rates are $r_{FBD}=B_{FBD}(N_D^0)p$ [$r_{FBA}=B_{FBA}(N_A^0)n$].

important parameters that we discuss below. We take the depth of the Yb^{3+} REI trap (electron isoelectronic trap) from the experiment to be 30 meV below the conduction band, because we wish to apply results of the calculations to InP:Yb. This trap may exist in six distinct states: (1) the neutral unoccupied trap (concentration N_0), (2) the negatively charged (concentration N_-), (3) the exciton occupied (concentration N_X), (4) the neutral excited (concentration N_0^*), (5) the excited negatively charged (concentration N_-^*), and (6) the excited exciton occupied (concentration N_X^*). The total concentration of isoelectronic traps N is given by
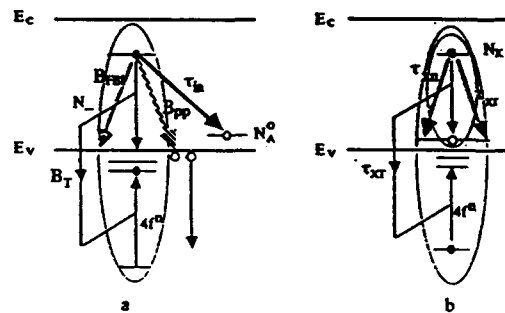

FIG. 2. A schematic representation of energy-transfer processes to core states of structured impurity and radiative and nonradiative transitions. (a) Auger energy-transfer process where the recombination energy of the bound electron with the free hole is transferred to the REI impurity core states (coefficient B_T). B_{pp} is the nonradiative Auger process coefficient involving bound electron and two free holes, B_{FBI} the coefficient of radiative recombination of bound electron to free hole, and τ_{ia} the recombination of bound electron with a hole on a distant acceptor. (b) The energy-transfer process from a bound exciton on a REI trap (shadow ellipse) to core states (B_{XT} transfer coefficient) and τ_{xr} and τ_{xn} are the bound exciton radiative and nonradiative recombination times, respectively ($1/\tau_2=1/\tau_{xr}+1/\tau_{xn}$).
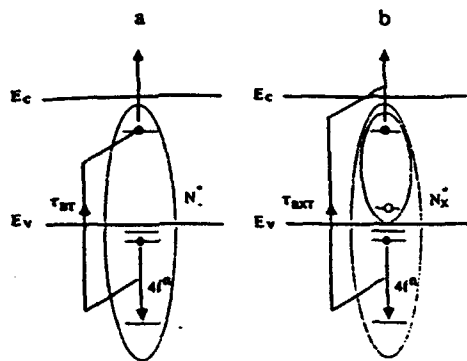
FIG. 3. Energy back transfer processes. (a) The auto deionization Auger quenching mechanism and its characteristic time τ_{BT} (Auger transfer rate $\tau_{BT}=B_{BT}N^*_-$). (b) The energy back transfer process from the excited REI trap to a bound exciton with characteristic time τ_{BXT} (Auger transfer rate $\tau_{BXT}=B_{BXT}N^*_X$).

FIG. 5. Auger quenching processes involving interaction of the core excited REI trap with (a) and (b) free electrons or holes and their coefficients B_{BT3} and B_{BT4}. Interaction of the core excited REI trap with an electron (c) [hole (d)] on neutral donor (acceptor) and their coefficients B_{BT5} and B_{BT6}.

$$N=N_0+N_-+N_X+N^*_0+N^*_-+N^*_X .$$

Many of the symbols are the same as those defined in Refs. 31–33. Figure 1(a) shows how the neutral isoelectronic trap is transformed into an N_- state: an electron is captured within a time defined by $\tau_{et}=(v_{th}\sigma_{RE}N)^{-1}$, where v_{th} is the thermal velocity of the free electron, and σ_{RE} is the cross section for the capture of electrons by unoccupied traps. The capture rate of electrons by the isoelectronic trap is $(n/\tau_{et})(N_0/N)$, where n is the free electron density. The N_- center can be transformed to the neutral rare-earth core excited center N^*_0 through an Auger process where the recombination energy of the bound electron with free hole is transferred nonradiatively to the core states with a rate

$$r_T=B_T N_- p ,$$

where B_T is the energy-transfer coefficient, and p is the free hole density. If the initial and final states are not resonant, the energy mismatch must be distributed in some way such as phonon emission or absorption [Figs. 2(a) and 2(b)]. The N_- may also recombine radiatively or nonradiatively (via the Auger process) with a hole in the


FIG. 4. Auger nonradiative recombination involving the interaction of the core excited REI trap (N^*_0) with an electron trapped on separate centers N_- (a) and N^*_- (b), where B_{BT1} and B_{BT2} are the Auger coefficients.

valence band with transition rate $r_{FBI}=B_{FBI}$ (N_- or N^*_-)p and $r_{pp}=B_{pp}(N_-$ or $N^*_-)p^2$, respectively [Fig. 2(a)], or recombine radiatively with a hole trapped on a distant acceptor (in the case of p-type material). The last three processes transform the N_- center into the N_0 neutral trap. The N^*_0 may capture an electron and be transformed into an N^*_- center. The N^*_- may lose the electron through processes described above, or by ion autodeionization Auger process ($N^*_-\rightarrow N_0+e$-kinetic energy). This is the Auger nonradiative luminescence quenching mechanism of the excited rare-earth isoelectronic trap, with characteristic time τ_{BT} as shown in Fig. 3(a). The exciton bound to a REI trap with exited core states (N^*_X), can back transfer energy from core excitations to the exciton, and dissociate it with liberation of an electron or hole. Once formed, the N_- and N^*_- states can also be converted into N_0 and N^*_0 states, respectively, by thermal ionization (time τ_{te}), or to N_X and N^*_X, respectively, by capturing a hole from the valence band with time defined by $\tau_{px}=(v_{th}\sigma_{Rx}N)^{-1}$ [see Fig. 1(b)].

The second important energy-transfer process from an exciton bound to a REI trap to core states is shown in Fig. 2(b). In this process energy is transferred from the bound exciton (on isoelectronic trap N_X) to the core states with the rate $r_{XT}=B_{XT}N_X$, where B_{XT} is the transfer coefficient, and τ_{XT} is the characteristic time. If the initial and final states are not resonant, the energy mismatch must be accommodated by emission or absorption of phonons. At sufficiently high temperatures, the electron from N_- and N^*_- may be thermally emitted to the conduction band at a rate $(n_t/\tau_{te})(N_-/N$ or $N^*_-/N)$, where $n_t=N_c\beta_t\exp[-E_{RET}/kT]$, $(1/\beta_t)$ is the degeneracy of the structured isoelectronic trap level at energy E_{RET} below the conduction band, and N_c is the conduction-band density of states.

The exciton bound to isoelectronic traps N_X and N^*_X can thermally dissociate by either of two processes: (1) it can dissociate into a free exciton (X) and neutral N_0, or an neutral excited (N^*_0) REI trap, respectively; or (2) it can dissociate with the liberation of a hole, with the time
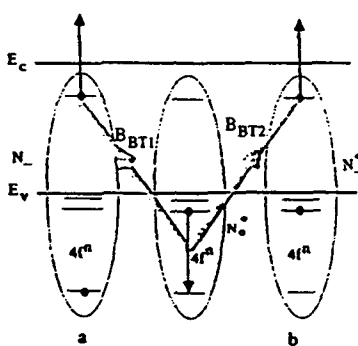
$1/\tau_{xp} = (1/\tau_{px})(p_h/N)$, where $p_h = N_v\beta_h^{-1}\exp[-E_h/kT]$, N_v is the effective density of state in the valence band, and β_h is the degeneracy of the hole component of the exciton having binding energy E_h.[32,49]

The REI traps N_0^*, N_-^*, and N_X^* may also be deexcited to N_0, N_-, and N_X, respectively, by desirable radiative transitions between the $4f^n$ core states, emitting photons with a decay time τ_3.

The nonradiative decay channel of free carriers through an additional type of trap N_s, the "shunt path" with two states, is shown in Fig. 1(c). The concentrations of traps in these two states are denoted N_s^0, the neutral unoccupied, and N_s^-, the negatively charged (bound electron), respectively $(N_s = N_s^0 + N_s^-)$. The probability per unit time for an electron (hole) to be captured by an empty (electron occupied) shunt is $1/\tau_{ns}$ and $(1/\tau_{ps})$, respectively. For intrinsic excitation (band to band) the shunt paths deplete the express electron-hole pairs. Under such excitation the shunt paths can be either partially or completely saturated, depending on the concentration, the time constants, and the generation rate of electron-hole pairs. Figures 1(d) and 1(e) show the characteristic parameters for donors and acceptors incorporated into the model, in cases of n- or p-type samples, respectively.

All the above discussed Auger processes [Figs. 4(a) and 4(b) and Figs. 5(a)–5(d)] are similar to the two center problems analyzed in some papers.[32,50,41–43,51,45,46] Figure 4(a) shows an example of nonradiative recombination involving the interaction of a core excited isoelectronic trap (N_0^*) with an electron trapped on a separate center (N_-), or an electron trapped on a core excited REI trap (N_-^*). The recombination rates for these processes are proportional to N_0^*, and the concentrations of N_- or N_-^* traps such that

$$r_{BT1} = B_{BT1}N_0^*N_- , \quad r_{BT2} = B_{BT2}N_0^*N_-^* ,$$

where B_{BT1}, and B_{BT2}, are the Auger coefficients.

According to the theory developed by Langer,[45,48] the two additional paths of energy transfer from the excited REI trap are the first to free electrons (holes) with Auger coefficients B_{BT3} (B_{BT4}), and second to electrons bound at the shallow donors (acceptors) [Figs. 5(a)–5(d)], and are also attributed to the luminescence quenching. The two processes shown in Figs. 5(c), and 5(d) involve interaction of a core-excited REI trap with an electron (hole) on a neutral donor (acceptor), and are characterized by Auger coefficients B_{BT5} and B_{BT6}, respectively. The first process is important during the exciting pulse, and the second processes are expected to be important at low temperatures where all electrons (holes) are frozen out onto neutral donors (acceptors).

We can now complete the formal description of the models by deriving the differential equations for the REI-trap energy-transfer processes and recombination kinetics. The differential equations govern the variations with the time of the concentrations of various components under band-to-band excitation. By consulting Figs. 1–5 (there are six possible states in REI traps, and two in shunt paths and generated free carriers), they may be readily written down:

$$\frac{dN_-}{dt} = \frac{n}{\tau_{el}}\left[\frac{N_0}{N}\right] + \frac{N_-^*}{\tau_3} + \frac{1}{\tau_{xp}}\left[\frac{N_X}{N}\right]\frac{N_v}{\beta_h}\exp\left[-\frac{E_h}{kT}\right]$$
$$- \frac{1}{\tau_{le}}\left[\frac{N_-}{N}\right]\beta_t N_c\exp\left[-\frac{E_t}{kT}\right]$$
$$- \frac{p}{\tau_{px}}\left[\frac{N_-}{N}\right] - B_{FBI}(N_-)p$$
$$- B_T(N_-)p - B_{BT1}(N_0^*)N_- , \tag{1}$$

$$\frac{dN_X}{dt} = \frac{N_X^*}{\tau_3} + \frac{p}{\tau_{px}}\left[\frac{N_-}{N}\right] - N_X\left[\frac{1}{\tau_2} + \frac{1}{\tau_{XT}} + \frac{1}{\tau_{xd}}\right]$$
$$- \frac{1}{\tau_{xp}}\left[\frac{N_X}{N}\right]\frac{N_v}{\beta_h}\exp\left[-\frac{E_h}{kT}\right] , \tag{2}$$

$$\frac{dN_0^*}{dt} = \frac{N_X}{\tau_{XT}} + B_T(N_-)p + \frac{1}{\tau_{le}}\left[\frac{N_-^*}{N}\right]\beta_t N_c\exp\left[-\frac{E_t}{kT}\right]$$
$$- \frac{n}{\tau_{el}}\left[\frac{N_0^*}{N}\right] - \frac{N_0^*}{\tau_3} - B_{BT1}(N_0^*)N_-$$
$$- B_{BT3}(N_0^*)n - B_{BT4}(N_0^*)p , \tag{3}$$

$$\frac{dN_-^*}{dt} = \frac{n}{\tau_{el}}\left[\frac{N_0^*}{N}\right] + \frac{1}{\tau_{xp}}\left[\frac{N_X^*}{N}\right]\frac{N_v}{\beta_h}\exp\left[-\frac{E_h}{kT}\right]$$
$$- \left[\frac{1}{\tau_3} + \frac{1}{\tau_{BT}}\right]N_-^* - \frac{p}{\tau_{px}}\left[\frac{N_-^*}{N}\right]$$
$$- \frac{1}{\tau_{le}}\left[\frac{N_-^*}{N}\right]\beta_t N_c\exp\left[-\frac{E_t}{kT}\right]$$
$$- B_{BT2}(N_0^*)N_-^* - B_{FBI}(N_-^*)p , \tag{4}$$

$$\frac{dN_X^*}{dt} = \frac{p}{\tau_{px}}\left[\frac{N_-^*}{N}\right] - N_X^*\left[\frac{1}{\tau_2} + \frac{1}{\tau_3} + \frac{1}{\tau_{BXT}} + \frac{1}{\tau_{xd}}\right]$$
$$- \frac{1}{\tau_{xp}}\left[\frac{N_X^*}{N}\right]\frac{N_v}{\beta_h}\exp\left[-\frac{E_h}{kT}\right] , \tag{5}$$

$$\frac{dn}{dt} = G + N_X^*\left[\frac{1}{\tau_{xd}} + \frac{1}{\tau_{BXT}}\right]$$
$$+ \left[\frac{N_- + N_-^*}{N}\right]\frac{1}{\tau_{le}}\beta_t N_c\exp\left[-\frac{E_t}{kT}\right]$$
$$+ \frac{N_X}{\tau_{xd}} + \frac{N_-^*}{\tau_{BT}} - \frac{n}{\tau_{el}}\left[\frac{N_0 + N_0^*}{N}\right] - \frac{n}{\tau_{ns}}\left[\frac{N_s^0}{N_s}\right]$$
$$+ B_{BT2}(N_0^*)N_-^* + B_{BT1}(N_0^*)N_- , \tag{6}$$

$$\frac{dp}{dt} = G + \frac{1}{\tau_{xp}}\frac{N_v}{\beta_h}\exp\left[-\frac{E_h}{kT}\right]\left[\frac{N_X + N_X^*}{N}\right]$$
$$- \frac{p}{\tau_{px}}\left[\frac{N_- + N_-^*}{N}\right] - \frac{p}{\tau_{ps}}\left[\frac{N_s - N_s^0}{N_s}\right]$$
$$- B_T(N_-)p - B_{FB}(N_- + N_-^*)p , \tag{7}$$

$$\frac{dN_s^0}{dt} = \frac{p}{\tau_{ps}}\left[1 - \frac{N_s^0}{N_s}\right] - \frac{n}{\tau_{ns}}\left[\frac{N_s^0}{n_s}\right],$$ (8)

$$N_0 = N - N_- - N_X - N_0^* - N_-^* - N_X^*,$$ (9a)

$$N_s = N_s^0 + N_s^-,$$ (9b)

$$p = n + N_- + N_-^* + \left[1 - \frac{N_s^0}{N_s}\right]N_s.$$ (10)

Equations (1)–(5) govern the negatively charged-rare earth isoelectronic trap populations (1), the neutral exciton occupied rare-earth isoelectronic trap populations (2), the neutral core excited rare-earth isoelectronic trap populations (3), the negatively charged core exited rare-earth isoelectronic trap populations (4), and the exciton occupied core excited rare-earth isoelectronic trap populations (5), respectively. Equations (6) and (7) represent the changes in the total free electron (n) and hole (p) populations, respectively. *Equation (8) governs the density of shunt path traps.* Equations (9a) and (9b) state the constancy of the total concentrations of REI traps and shunt paths, respectively, and Eq. (10) is the neutrality condition equation. $G = gf(t - T)$ is the generation rate of free electrons and holes by above band-gap laser excitation. The electron-hole pair generation rate is controlled by a unit step function $f(t - T)$, (T is the pulsewidth) which takes on the value of zero or unity according to whether its argument is less than or equal to zero or greater than zero. The volume generation rate is approximated by $g(z) \simeq \alpha I \exp[-\alpha z]$, where α is the absorption coefficient, and I is photon flux in # photons/(cm²/sec).

For n-type material the equations are even more complicated (see the Appendix); similar equations hold for p-type material. Such systems of coupled, first-order stiff nonlinear differential equations require specialized numerical integration routines designed specifically for stiff systems. The kinetic equations were solved numerically as a function of excitation intensities, using as fitting parameters the time constants and rate coefficients defined in Table II. To describe the buildup and decay kinetics of rare-earth luminescence in a semiconductor host, we assumed only band-band pulse excitation. The above set of ten equations (1)–(10) was reduced to eight dimensionless differential equations which is more convenient for numerical solutions. To solve this system we assumed, for simplicity, that the above band-gap excitations take place at low enough temperatures (in our experiment 8.6 K) so that thermal activation of the trapped carriers is negligible. That is, terms explicitly dependent on temperature were ignored, and only trapping, transferring, and recombination transitions were considered. The radiative recombination of excitons bound to "simple" isoelectronic impurities has a long lifetime ranging from a few hundred to a few thousand nanoseconds.[24,28-32] That time is much longer than the energy-transfer time τ_{XT} from an exciton bound to a REI trap to core states. The measurements on n-type InP:Yb show that this transfer time is much less than 10 ns.[7] The above facts explain why we do not observe the luminescence of excitons bound to REI traps. The numerical solution of Eqs. (1)–(10) was obtained using the parameters shown in Table II. Gor-

TABLE II. Parameters describing rise and decay kinetics of InP:Yb.

Symbol	Unit	Parameter value	References
τ_2	s	2×10^{-7}	24,28-32
τ_3	s	11.6×10^{-6}	9,44
τ_{BT}	s	5×10^{-7}	31,32,41-43
τ_{BXT}	s	5×10^{-7}	31,32,41-43
τ_{ns}	s	5×10^{-8}	33(b),33(c)
τ_{ps}	s	3×10^{-8}	33(b),33(c)
τ_{XT}	s	1.25×10^{-9}	7
τ_{n}	s	5×10^{-11}	33(b),33(c)
τ_{px}	s	5×10^{-11}	33(b),33(c)
B_T	cm³/s	4×10^{-10}	
B_{FBI}	cm³/s	1×10^{-11}	31,32,41-43
B_{BT1}	cm³/s	1.2×10^{-13}	31,32,41-43
B_{BT2}	cm³/s	1.2×10^{-13}	31,32,41-43
B_{BT3}	cm³/s	4×10^{-13}	45-48
B_{BT4}	cm³/s	4×10^{-13}	45-48
N_s	cm⁻³	8×10^{16}	
N	cm⁻³	5×10^{17}	
G	# photons/(cm³ s)	$2 \times 10^{20} - 1.5 \times 10^{23}$	

don and Allen[46(a)] and Ayling and Allen[46(b)] and Langer, Van Hong[45,48(a),48(b)] made quantitative measurements of the luminescence efficiency and lifetime in ZnS:Mn, ZnSe:Mn, CdF₂:Mn, and CdF₂:Gd, where they obtained a value for the Auger quenching coefficients by free electrons and an electron bound on shallow donors.[48] A surprising result is that the value of Auger coefficients for centers in CdF₂ ($\approx 5 \times 10^{-15}$ cm³ s⁻¹) is about four order of magnitude smaller than the value for ZnS and ZnSe (5×10^{-10} cm³ s⁻¹). Klein, Ferneaux, and Henry[46(c)] estimated the Auger coefficient for the InP:Fe system to be $\approx 6.7 \times 10^{-10}$ cm³ s⁻¹. Excellent reviews of theory and experimental data of Auger processes and values of coefficients are given by Landsberg and Adams.[42,43] The values of the parameters chosen for the calculations are estimated from experimental data obtained from similar "simple" isoelectronic traps (see references in Table II). We believe that all constants are realistic, and characteristic for InP:Yb. The volume generation range G of e-h pairs wa chosen in the same range as in the experiment.[44] The kinetics of luminescence of InP:Yb as the functions of excitation intensity was simulated by repeating the numerical calculations for several different values of the generation rate. We simulated the kinetics of the photoluminescence measurement by choosing square generating pulses with 60-μs duration, adequate to establish a quasiequilibrium luminescence intensity during excitation. The luminescence intensities are proportional to N_0^*, N_-^*, and N_X^*. The last two terms can be ignored because they introduce very small contributions to the total luminescence intensity, mainly during the excitation pulse. The numerically simulated luminescence rise and decay are shown in Fig. 6 as a function of generation rates (G), and sets of the parameters from Table II. The profiles shown the buildup of luminescence, allowing the process to reach a steady-state value for a given excitation intensity, and the decay after switching off the exci-

tation pulse. All profiles shown on Fig. 6 are normalized to unity at maximum. The rise times given in the figure decrease with the increasing generation rates. At the low generation rate of 2×10^{20} photon/(cm³s) the buildup curve (which can be well approximated by a single exponential curve) has a rise time of 11.98 μs, while at the generation rate of 1.5×10^{23} photons/(cm³s) the rise time is 1.7 μs. The decay profiles for the above two generation rates shown in Fig 6 are 11.7 μ and 6.9 μs, respectively. The remaining four decay times fall in that window. The rise and decay times for simulated kinetics are well approximated by single exponential processes, while the experimental data are described better by double exponential functions. Figure 7 shows the computed rise and decay times as a function of excitation intensities (generation rate). The experimental data are imposed on the computed curve. The circle shown in Fig. 7 represents experimental rise times obtained from fitting to a single exponential function (with the coefficient of determination $r^2 \approx 0.98$). The squares stand for the rise times of the dominant component of the experimental data fitted to a double exponential function. In Fig. 7 the upper solid line is the computed decay time and the dots represent the experimental decay times of the dominant component of the double exponential fitting. The second small exponential component has the decay times in the range 0.9–1.8 μs. The double exponential rise and decay times observed in the experiment are probably related to other energy-transfer processes (not incorporated to our model) from Yb to other accidental impurities where the energy is dissipated nonradiatively. Iron is a common contaminant in metal-organic chemical-vapor deposition (MOCVD) grown Yb-doped InP crystals. The energy-transfer process from Yb^{3+} to Fe ions is attributed to thermal quenching of the luminescence intensity and decay time with an increase in temperature.[44] The detailed analysis of the parameters and their influence on the rise
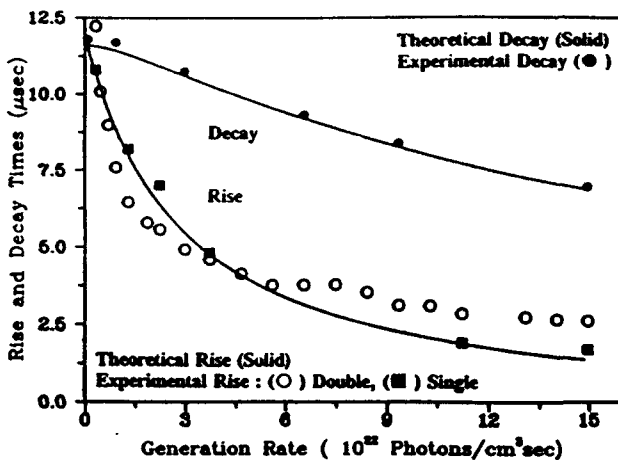
FIG. 7. The numerically computed rise time (solid line) of rare-earth luminescence (InP:Yb) as a function of generation rates. The circles represent the experimental values of the rise-time constants of ytterbium luminescence in InP at 8.4 K (fitted to single exponential function, with the coefficient of determination $r^2 \approx 0.986$). The squares stand for the rise-time constants of the dominant component of the experimental data fitted to the double exponential function. The dots stand for the decay-time constants of the dominant component of the experimental data fitted to double exponential function.

time, and the efficiency of the steady-state luminescence and decay time will be published elsewhere. The numerically simulated luminescence rise and decay measurements show a good overall quantitative agreement with the experiment over a wide range of generation rates (Figs. 6 and 7). Finally, the proposed model can be refined by taking into account the surface recombination and carrier diffusion processes, which may play important roles in the reduction of the overall photoluminescence emission.[53]

IV. POSSIBLE QUENCHING MECHANISMS AND TEMPERATURE DEPENDENCE

Discussed below are several possible nonradiative processes that quantitatively explain the kinetics (rise and decay of luminescence of the REI trap) and temperature dependence of the observed quenching. The Auger quenching processes defined in Sec. III are shown in Figs. 3–5. Processes [Figs. 4(a) and 4(b) and 5(a) and 5(b)] nonradiative recombination involving the interaction of a core excited REI trap, with an electron trapped on a separate REI trap. The next two-center recombination involves the interaction of the excited REI trap with an electron (hole) on a separate neutral donor (acceptor), respectively. The rate equations describe the nonradiative recombination involving the interaction of a core exited REI trap, with a free electron or hole, respectively. The last process is a very efficient nonradiative deexcitation mechanism of localized centers (Mn^{2+}) in ZnS, ZnSe, and CdF_2[45,47] and Gd^{3+} and Tb^{3+} in CdF_2.[48] The free-carrier Auger quenching processes are important at higher temperatures, and were shown to be much more efficient than the Auger process due to the shallow
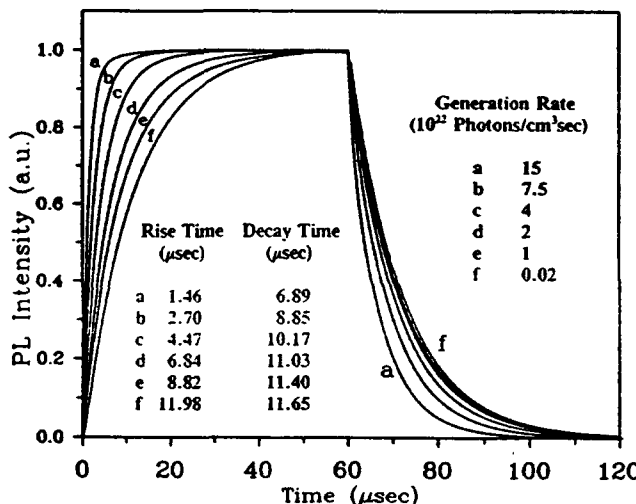

FIG. 6. Numerical solutions of Eqs. (1)–(10). The rare-earth luminescence intensity vs time for different generation rates and the set of parameters shown in Table II. The set of curves $a-f$ represents computed profiles (normalized to unity at maximum), showing the buildup of luminescence, the steady-state value, and the decay after switching off (at 60 μs) the excitation pulse.

donors. The last one is important only at low temperatures.[47] The most probable nonradiative mechanism quenching the rare-earth luminescence in III-V semiconductors is the Auger energy back transfer mechanism shown schematically in Figs. 3(a) and 3(b). The rare-earth-excited isoelectronic trap occupied by electron N^*_- or exciton N^*_X can transfer energy to the trapped electron or exciton rather than to the radiative field; the electron is consequently ejected deep into the conduction band. It is emphasized that at low temperatures the only electrons in the conduction band come from either the exciting source or from Auger ionization of the REI traps or neutral donors (in the case of n-type samples). The nonradiative recombination involving the interaction of the core-excited REI trap with a free electron (or hole) is important in seminsulating InP crystals only during the excitation pulse. In the dark the electron concentration at a temperature of 300 K is in the range 1×10^8 cm^{-3}. However, the experimental decay time of Yb luminescence is ~ 12 μs in SI-, n-, and p-type InP:Yb.[3,4,6]

The other mechanisms of the nonradiative recombination of the excited states of localized centers in semiconductors are first, the multiphonon relaxation processes,[55] and second, a migration of energy and cross relaxation processes.[56,57] The probability of the multiphonon relaxation processes is dependent upon the type of coupling with the lattice vibrations and the phonon frequency distribution. The ion-host lattice interaction for RE^{3+} $4f^n$ electrons is characteristic of weak coupling, and the multiphonon emission rates exhibit an approximately exponential dependence on the energy gap to the next lowest level. For a single frequency p phonon process the nonradiative rate for narrow-line emission is described by Kiel's formula[58]

$$W^p_{nr}(T) = W^p_{nf}(0)[1+n]^p ,$$

where $W^p_{nf}(0)$ is the rate at low temperature, p is the number of phonons involved, n is the occupancy of the phonon modes:

$$n = [\exp(\hbar\omega/kT) - 1]^{-1} ,$$

and the average phonon energy $\hbar\omega = \Delta E/p$. The single frequency model seems to be an oversimplification, and taking a weighted average over the phonon's spectrum, or consideration of the continuous nature of the phonon spectrum would be more appropriate.[59]

The results of many studies demonstrate that for given host crystals, the most critical parameter affecting the rate of multiphonon emission is the energy gap to the nearest- lower level. If the energy gap to the next lower state is sufficiently large the nonradiative multiphonon rate is negligible compared to the radiative rate, and this is the situation for most rare-earth ions in III-V semiconductors. For example, in InP: Yb^{3+} the $^2F_{3/2} - {}^2F_{7/2}$ energy gap is 9895 cm^{-1}, in GaAs: Er^{3+} the $^4I_{13/2} - {}^4I_{15/2}$ energy gap is 6051 cm^{-1}, and in GaAs:Nd^{3+} the $^4F_{3/2} - {}^4I_{11/2}$ energy gap is 10 636 cm^{-1}. The highest energy phonons in InP and GaAs are 345.2 and 292.7 cm^{-1} LO phonons, respectively. Nonradiative decay for the three cases above would require the generation of 27, 21,

and 36 LO phonons, respectively. Studies in different host materials,[55(a),55(b)] show that nonradiative decay involving the generation of more than five phonons is weaker than the radiative process.

When the concentrations of the rare-earth luminescent ions are higher, or centers create pairs, allowance must be made of the possibility of interaction between centers. This interaction may be too weak to modify the energy levels, but yet be adequately strong to enable transfer of energy from one to another.[38(b),57]

The migration of energy in InP doped with Yb^{3+} occurs through resonant interaction. The energy level diagram of Yb^{3+} in a crystal field of the tetrahedral symmetry (T_d) in InP indicates that the only possible interaction between the Yb^{3+} ions at low temperature is resonant interaction between the lower Stark sublevel of the ground state $^2F_{7/2}$ and the lower Stark to the accidental impurity with an absorption spectrum overlapping with that of the Yb^{3+} ion, emission is the most probable quenching mechanism. In Nd^{3+}-doped GaAs the energy of a single excited ion may be transferred to the same level of an identical ion (resonant energy migration), and finally to the quenching center.[52,54,60,61,44] The second possible degradation of excitation energy is the cross relaxation process. The presence of appropriate intermediate levels in the Nd^{3+} ion ($^4I_{11/2}$ and $^4I_{13/2}$) between the ground $^4I_{9/2}$ and excited $^4I_{3/2}$ states makes effective the cross relaxation process and increases the probability of nonradiative quenching processes.[38,62,63] All the above-discussed transfer processes are temperature dependent and can be useful in explaining the quenching of luminescence of rare earths in semiconductors. A full account of our results on the temperature dependence of rise, decay, and quenching mechanisms will be published at a latter data.

V. SUMMARY

In this work we have developed a kinetics model of energy transfer from the host lattice to the localized core excited states of rare-earth isoelectronic structured traps. According to Robbins and Dean[17] the formation of bound states at the structured cationic isoelectronic impurities is fairly common, which is in contrast to the situation normally found for anionic substituents in semiconductors. The outer electron configurations of RE^{3+} ions are the same $(5s^2 5p^6)$. Among rare-earth ions are those that, upon replacing the element from column III in III-V compounds that are isovalent concerning outer electrons of RE^{3+} ions, create isoelectronic traps in III-V semiconductors. We have evidence that the other RE ions in III-V semiconductors can occupy different sites (not only substitutional). The rare-earth isoelectronic trap must not necessarily be the "pure" substitutional center; if the rare-earth ions are very active chemically, they can create a more complex center involving other impurity or native defects. This conclusion is supported by the fact that the atomic covalent radii (ionic RE^{3+}) for all rare earths are bigger than atomic radii of Ga in In that they replace. Pauling's electronegativity of rare-earth elements are in the range of 1.1–1.25, and are

smaller than Ga (1.81) and In (1.78) for which they substitute. The rare-earth isovalent traps that we can call isoelectronic "structured" impurities[17] posse·s the unfilled $4f^n$ core shell. The structured luminescence arises from intraconfiguration f-f transitions in the core of the isoelectronic "structured" impurities.

The presence of low-lying empty core orbitals in rare-earth impurities introduces new excitation and recombination phenomena. To adequately describe the energy transfer to the REI trap, and the buildup and decay kinetics of rare-earth luminescence, we have considered six separate states of the REI impurity (unoccupied, electron occupied, electron occupied excited, neutral exciton occupied, exited electron occupied, and excited exciton occupied). The energy-transfer processes occur through an Auger mechanism, where the recombination energy of the bound electron with the free hole is transferred non-radiatively to the core states. The second energy-transfer process is the transfer of energy from the bound exciton on the REI trap to the core states. If the initial and final states are not resonant (in both mechanisms), the energy mismatch must be accommodated by emission or absorption of phonons.[17,38(b),56] Furthermore, we discussed the details of several quenching processes which are incorporated into the kinetics equations. We derive two sets of differential equations for SI-, and n- (p-) type semiconductors governing the kinetics of rare-earth luminescence. The nonradiative pathways present alternative recombination possibilities for the electrons and holes and are incorporated in both models. Equations governing the transfer of energy processes and recombination kinetics have been determined and solved by a numerical method

to derive the time dependence of the rise and decay kinetics as a function of excitation intensity. The parameters used are realistic, but only approximately known (see Table II). The numerically simulated luminescence rise and decay times show a good overall quantitative agreement with experiment over a wide range of generation rate values (see Figs. 6 and 7). Finally, the proposed model can be refined by taking into account the quenching processes discussed above, and the surface recombination and carrier diffusion processes, which plays an important role in reduction of the overall photoluminescence emission.[53]

APPENDIX

Consulting Figs. 1–5, the equations describing the transfer and recombination kinetics in n-type semiconductor may be written as follows:

$$\frac{dN_-}{dt} = \frac{n}{\tau_{et}}\left[\frac{N_0}{N}\right] + \frac{N_-^*}{\tau_3} + \frac{1}{\tau_{xp}}\left[\frac{N_X}{N}\right]\frac{N_v}{\beta_h}\exp\left[-\frac{E_h}{kT}\right] - \frac{1}{\tau_{te}}\left[\frac{N_-}{N}\right]\beta_t N_c\exp\left[-\frac{E_t}{kT}\right]$$

$$- \frac{p}{\tau_{px}}\left[\frac{N_-}{N}\right] - B_{FBI}(N_-)p - B_{BT1}N_0^*(N_-) - B_T(N_-)p \ , \tag{A1}$$

$$\frac{dN_X}{dt} = \frac{N_X^*}{\tau_3} + \frac{p}{\tau_{px}}\left[\frac{N_-}{N}\right] - N_X\left[\frac{1}{\tau_2} + \frac{1}{\tau_{XT}} + \frac{1}{\tau_{xd}}\right] - \frac{1}{\tau_{xp}}\left[\frac{N_X}{N}\right]\frac{N_v}{\beta_h}\exp\left[-\frac{E_h}{kT}\right] \ , \tag{A2}$$

$$\frac{dN_0^*}{dt} = \frac{N_X}{\tau_{XT}} + B_T(N_-)p + \frac{1}{\tau_{te}}\left[\frac{N_-^*}{N}\right]\beta_t N_c\exp\left[-\frac{E_t}{kT}\right] - \frac{n}{\tau_{et}}\left[\frac{N_0^*}{N}\right] - \frac{N_0^*}{\tau_3}$$

$$- B_{BT5}(N_D^0)(N_0^*) - B_{BT1}(N_-)(N_0^*) - B_{BT3}(n)(N_0^*) - B_{BT4}(p)(N_0^*) \tag{A3}$$

$$\frac{dN_-^*}{dt} = \frac{n}{\tau_{et}}\left[\frac{N_0^*}{N}\right] + \frac{1}{\tau_{xp}}\left[\frac{N_X^*}{N}\right]\frac{N_v}{\beta_h}\exp\left[-\frac{E_h}{kT}\right] - N_-^*\left[\frac{1}{\tau_3} + \frac{1}{\tau_{BT}}\right] - B_{FBI}(N_-^*)p$$

$$- \frac{p}{\tau_{px}}\left[\frac{N_-^*}{N}\right] - \frac{1}{\tau_{te}}\left[\frac{N_-^*}{N}\right]\beta_t N_c\exp\left[-\frac{E_t}{kT}\right] - B_{BT2}(N_0^*)(N_-^*) \ , \tag{A4}$$

$$\frac{dN_X^*}{dt} = \frac{p}{\tau_{px}}\left[\frac{N_-^*}{N}\right] - N_X^*\left[\frac{1}{\tau_2} + \frac{1}{\tau_3} + \frac{1}{\tau_{BXT}} + \frac{1}{\tau_{xd}}\right] - \frac{1}{\tau_{xp}}\left[\frac{N_X^*}{N}\right]\frac{N_v}{\beta_h}\exp\left[-\frac{E_h}{kT}\right] \ . \tag{A5}$$

$$\frac{dn}{dt} = G + N_x^* \left[\frac{1}{\tau_{xd}} + \frac{1}{\tau_{BXT}} \right] + \left[\frac{N_- + N_-^*}{N} \right] \frac{1}{\tau_{te}} \beta_t N_c \exp\left[-\frac{E_t}{kT} \right] + \frac{N_x}{\tau_{xd}} + \frac{N_-^*}{\tau_{BT}} - \frac{n}{\tau_{et}} \left[\frac{N_0 + N_0^*}{N} \right] - \frac{n}{\tau_{ns}} \left[\frac{N_s^0}{N_s} \right]$$

$$+ B_{BT1}(N_-)(N_0^*) + B_{BTS}(N_0^*)N_D^0 + \left[\frac{N_D^0}{N_D} \right] \frac{N_c}{\tau_{nD}} \beta_D \exp\left[-\frac{E_D}{kT} \right] - \left[1 - \frac{N_D^0}{N_D} \right] \frac{n}{\tau_{nD}} + B_{BT2}(N_0^*)N_-^* , \qquad (A6)$$

$$\frac{dp}{dt} = G + \frac{p_h}{\tau_{xp}} \left[\frac{N_x}{N} \right] + \frac{p_h}{\tau_{xp}} \left[\frac{N_x^*}{N} \right] - \frac{p}{\tau_{px}} \left[\frac{N_-}{N} \right] - \frac{p}{\tau_{px}} \left[\frac{N_-^*}{N} \right] - B_{FBI}(N_- + N_-^*)p - \frac{p}{\tau_{ps}} \left[\frac{N_s - N_s^0}{N_s} \right] - B_{FBD}(N_D^0)p , \qquad (A7)$$

$$\frac{dN_s^0}{dt} = \frac{p}{\tau_{ps}} \left[1 - \frac{N_s^0}{N_s} \right] - \frac{n}{\tau_{ns}} \left[\frac{N_s^0}{n_s} \right] , \qquad (A8)$$

$$\frac{dN_D^0}{dt} = \left[1 - \frac{N_D^0}{N_D} \right] \frac{n}{\tau_{nD}} - \left[\frac{N_D^0}{N_D} \right] \frac{\beta_D N_c}{\tau_{nD}} \exp\left[-\frac{E_D}{kT} \right] - B_{BTS}(N_D^0)N_0^* - B_{FBD}(N_D^0)p , \qquad (A9)$$

$$N_0 = N - N_- - N_x - N_0^* - N_-^* - N_x^* ,$$

$$N_s = N_s^0 + N_s^- ,$$

$$N_D = N_D^0 + N_D^+ , \qquad (A10)$$

$$p + N_D^+ = n + N_- + N_-^* + \left[1 - \frac{N_s^0}{N_s} \right] N_s .$$

Finally, the equation indicating the neutrality condition is

$$p = n + N_- + N_-^* + \left[1 - \frac{N_s^0}{N_s} \right] N_s - \left[1 - \frac{N_D^0}{N_D} \right] N_D \qquad (A11)$$

Equations (A1)–(A5) govern the negatively charged REI-trap population (A1), the neutral exciton occupied REI-trap population (A2), the neutral core excited REI-trap population (A3), the negatively charged core excited REI-trap population (A4), and the exciton occupied core excited (A5) rare-earth isoelectronic trap populations, respectively. Equations (A6) and (A7) represent the changes in the total free-electron and hole populations, respectively. Equation (A8), governs the density of neutral shunt path traps. Equation (A9) governs the density of neutral donors. Equations (A10) state the constancy of the total concentrations of REI traps, shunt paths, and donors, respectively, and Eq. (A11) is the neutrality condition equation. The symbols used in this set of equations are the same as for SI semiconductors.

[1]H. Ennen, G. Pomrenke, and A. Axmann, J. Appl. Phys. 57, 2182 (1985).

[2]G. Aszodi, J. Weber, Ch. Uihlein, L. Pu-lin, H. Ennen, U. Kaufmann, J. Schneider, and J. Windscheif, Phys. Rev. 31, 7767 (1985).

[3]P. B. Klein, Solid State Commun. 65, 1097 (1988).

[4]V. I. Masterov and L. F. Zakharenkov, Fiz. Tekh. Polopruvudu, 24, 610 (1990)], and references cited therein.

[5](a) P. S. Whitney, K. Uwai, H. Nakagome, and K. Takahei, Appl. Phys. Lett. 53, 2074 (1988); (b) K. Takahei and A. Taguchi, in Materials Science Forum, edited by G. Davies, G. DeLeo, and M. Stavola (Trans Tech, Zürich, Switzerland, 1992), Vols. 83–87, p. 641, and references therein; (c) M. Godlewski, K. Swiatek, A. Suchocki, and J. M. Langer, J. Lumin. 48&49, 23 (1991).

[6]K. Thonke, K. Pressel, G. Bohnert, A. Stapor, J. Weber, M. Moser, A. Malassioti, A. Hangleiter, and F. Scholz, Semicond. Sci. Technol. 5, 1124 (1990).

[7]C. Lhomer, B. Lambert, Y. Toudic, A. Le Corre, M. Gauneau, F. Clerot, and B. Sermage, Semicond. Sci. Technol. 6, 916 (1991).

[8]A. Taguchi, H. Nakagome, and K. Takahei, J. Appl. Phys. 70, 5604 (1991).

[9]H. J. Lozykowski, A. K. Alshawa, G. Pomrenke, and I. Brown, Bull. Am. Phys. Soc. 36, 2167 (1991).

[10]J. Wagner, J. Windschief, and H. Ennen, Phys. Rev. B 30, 6230 (1984).

[11]A. Stapor, J. Raczynska, H. Przybylinska, K. Fronc, and J. M. Langer, in Material Science Forum, edited by H. J. von Bardeleben (Trans Tech, Zürich, Switzerland, 1986), Vols. 10–12, p. 633.

[12](a) D. Seghier, T. Benyattou, G. Bremond, F. Ducroquet, J. Gregoire, G. Guillot, C. Lhomer, B. Lambert, Y. Toudic, and A. Le Corre, Appl. Phys. Lett. 60, 983 (1992); (b) B. Lambert, A. Le Corre, Y. Toudic, C. Lhomer, G. Grandpierre, and M. Gauneau, J. Phys. Condens. Matter. 2, 479 (1990); (c) S. N. Mustafaeva and M. M. Asadov, Inorg. Matter. 25, 180 (1989); (d) A. Tagushi, H. Nakagome, and K. Takahei, J. Appl. Phys. 68, 330 (1990); (e) J. E. Colon, D. W. Elsaesser, Y. K. Yeo, R. L. Hengehold, and G. S. Pomrenke, in Material Science Forum [Ref. 5(b)], Vols. 83–87, p. 671.

[13](a) T. Benyattou, D. Seghier, G. Guillot, R. Moncorge, P. Gal-

tier, and M. N. Charasse, in *Impurities, Defects and Diffusion in Semiconductors: Bulk and Layered Structures*, edited by D. J. Wolford, J. Bernholc, and EE. Maller, MRS Symposia Proceedings No. 163 (Materials Research Society, Pittsburgh, 1990); p. 69; (b) T. Benyattou, D. Seghier, G. Guillot, R. Moncorge, P. Galtier, and M. N. Charasse, Appl. Phys. Lett. 58, 2132 (1991).

[14]A. C. Aten, J. H. Haanstra, and H. de Vries, Philips Res. Rep. 20, 395 (1965).

[15]D. G. Thomas, J. Phys. Soc. Jpn. 21, 265 (1966).

[16]D. G. Thomas, J. J. Hopfield, and C. J. Frosch, Phys. Rev. Lett. 15, 857 (1965).

[17]D. J. Robbins and P. J. Dean, Adv. Phys. 27, 499 (1978), and references therein.

[18]H. C. Casey, Jr. and G. L. Pearson, J. Appl. Phys. 35, 3401 (1964).

[19]J. W. Allen, J. Phys. C 4, 1936 (1971).

[20]A. Baldereschi and J. J. Hopfield, Phys. Rev. Lett. 28, 171 (1972).

[21]A. Baldereschi, J. Lumin. 7, 79 (1973).

[22]P. J. Dean, J. Lumin. 7, 51 (1973).

[23]W. Czaja, in *Advances in Solid State Physics XI*, edited by O. Madelung (Pergamon, New York, 1971) p. 65, and references therein.

[24]P. J. Dean, A. M. White, E. W. Williams, and M. G. Astles, Solid State Commun. 9, 1555 (1971).

[25]W. Ruhle, W. Schmid, R. Meck, N. Stath, J. U Fischbach, I. Strottner, K. W. Benz, and M. Pilkuhn, Phys. Rev. B 18, 7022 (1978).

[26]J. L. Merz and R. T. Lynch, in *II-VI Semiconducting Compounds*, edited by D. G. Thomas (Benjamin, New York, 1967), p. 730.

[27](a) H. J. Lozykowski, P. O. Holtz, and B. Monemar, J. Electron. Mater. 12, 653 (1983); (b) H. J. Lozykowski and J. L. Merz, in *Properties of II-VI Semiconductors: Bulk Crystals, Epitaxial Films, Quantum Well Structures, and Dilute Magnetic Systems*, edited by F. J. Bartoli, Jr., H. F. Schaaler, and J. F. Schetzina, MRS Symposia Proceedings No. 161 (Materials Research Society, Pittsburgh, 1990), p. 171.

[28]T. R. N. Kutty and R. Revathi, Solid State Commun. 55, 197 (1985).

[29]J. D. Cuthbert and D. G. Thomas, Phys. Rev. 154, 763 (1967).

[30]J. D. Cuthbert, C. H. Henry, and P. J. Dean, Phys. Rev. 170, 739 (1968).

[31]J. S. Jayson, R. N. Bhargava, and R. W. Dixon, J. Appl. Phys. 41, 4972 (1970).

[32]J. M. Dishman and M. DiDomenico, Jr., Phys. Rev. B 1, 3381 (1970); J. M. Dishman, M. DiDomenico, Jr., and R. Caruso, *ibid*. 2, 1988 (1970); R. H. Bube, J. Phys. Chem. Solids, 1, 234 (1957).

[33](a) J. S. Jayson and R. Z. Bachrach, Phys. Rev. B 4, 477 (1971); (b) M. Sternheim and E. Cohen, Solid-State Electron. 21, 1343 (1978); (c) Phys. Rev. B 22, 1875 (1980).

[34](a) U. Heim, Phys. Status Solidi B 48, 629 (1971), (b) C. J. Hwang and L. R. Dawson, Solid State Commun. 10, 443 (1972).

[35]*Table of Periodic Properties of the Elements* (Sargent-Welch, Skokie, IL, 1980).

[36]J. C. Phillips, *Bonds and Bands in Semiconductors* (Academic, New York, 1973), p. 54

[37]J. Shaffer and F. Williams, Phys. Status Solidi 38, 657 (1970).

[38]For a review, see (a) D. L. Huber, in *Laser Spectroscopy of Solids*, edited by W. M. Yen and P. M. Selzer (Springer-

Verlag, Berlin, 1981), p. 83; (b) T. Holstein, S. K. Lyo, and R. Orbach, *ibid*; p. 39.

[39]P. D. Dapkus, W. H. Hackett, Jr., O. G. Lorimor, and R. Z. Bachrach, J. Appl. Phys. 45, 4920 (1974).

[40]R. Z. Bachrach and O. G. Lorimor, J. Appl. Phys. 43, 500 (1972).

[41]J. M. Dishman, Phys. Rev. 3, 2588 (1971); K. P. Sinha and M. DiDomenico, Jr., Phys. Rev. B 1, 2623 (1970).

[42]P. T. Landsberg and M. J. Adams, J. Lumin. 7, 3 (1973).

[43]P. T. Landsberg, *Recombination in Semiconductors* (Cambridge University Press, Cambridge, 1991), and references cited therein.

[44]H. J. Lozykowski, A. K. Alshawa, G. S. Pomrenke, and I. Brown, in *Rare Earth Doped Semiconductors*, edited by G. S. Pomrenke, P. B. Klein, and D. W. Langer, MRS Symposia Proceedings Vol. 301 (Materials Research Society, Pittsburgh, 1993), p. 263.

[45]J. M. Langer, in *Electroluminescence*, edited by S. Shinoya and H. Kobayasi, Springer Proceedings in Physics Vol. 38 (Springer-Verlag, Berlin, 1989), and references cited therein.

[46](a) N. T. Gordon and J. W. Allen, Solid State Commun. 37, 441 (1981); (b) S. G. Ayling and J. W. Allen, J. Phys. C 20, 4251 (1987); (c) P. B. Klein, J. E. Furneaux, and R. L. Henry, Phys. Rev. B 29, 1947 (1984).

[47]A. Suchocki and J. M. Langer, Phys. Rev. B 39, 7905 (1989).

[48](a) J. M. Langer, J. Lumin. 23, 141 (1981). (b) J. M. Langer and Le Van Hong, J. Phys. C 17, L923 (1984).

[49]E. W. Williams and H. B. Bebb, in *Semiconductors and Semimetals*, edited by R. K. Willardson and A. C. Beer (Academic, New York, 1972), Vol. 8, Chap. 5, p. 321, and references cited therein.

[50]E. I. Tolpygo, K. B. Tolpygo, and M. K. Sheinkman, Fiz. Tverd. Tela (Leningrad) 7, 1790 (1965) [Sov. Phys. Solid State 7, 1442 (1965)].

[51]G. F. Neumark, D. J. DeBitetto, R. N. Bhargava, and P. M. Harnack, Phys. Rev. B 15, 3147 (1977); 1, 3156 (1977).

[52]M. J. Weber, Phys. Rev. B 4, 2932 (1971).

[53]M. Boulou and D. Bois, J. Appl. Phys. 48, 4713 (1977).

[54]J. P. van der Ziel, L. Kopf, and L. G. Van Uitert, Phys. Rev. B 6, 615 (1972).

[55](a) H. W. Moss, J. Lumin. 1-2, 106 (1970); (b) L. A. Riseberg and M. J. Weber, in *Progress in Optics*, edited by E. Wolf (North-Holland, Amsterdam, 1975), Vol. 14.

[56]For a review, see (a) R. K. Watts, in *Optical Properties of Ionsin Solids*, edited by B. DiBartolo (Plenum, New York, 1975), pp. 307-336; (b) B. Henderson and G. F. Imbusch, *Optical Spectroscopy of Inorganic Solids* (Oxford University Press, New York, 1989).

[57]G. P. Morgan and W. M. Yen, in *Laser Spectroscopy of Solids II*. edited by W. M. Yen (Springer-Verlag, Berlin, 1989), p. 77.

[58]A. Kiel, in *Proceedings of the Third International Conference on Quantum Electronics, Paris, 1963*, edited by P. Grivet and N. Bloembergen (Columbia University Press, New York, 1964).

[59]M. D. Sturge, Phys. Rev. B 8, 6 (1973).

[60]B. A. Wilson, W. M. Yen, J. Hagarty, and G. F. Imbusch, Phys. Rev. B 19, 4238 (1979).

[61]F. Kellendonk, and G. Blasse, J. Chem. Phys. 75, 561 (1981).

[62]Yu. K. Voron'ko, V. V. Osiko, N. V. Savost'yanova, V. S. Fedorov, and I. A. Shcherbakov, Fiz. Tverd. Tela (Leningrad) 14, 2656 (1973) [Sov. Phys. Solid State 14, 2294 (1973)].

[63]H. J. Lozykowsi and K. Takahei (unpublished).

KINETICS OF THE LUMINESCENCE OF ISOELECTRONIC RARE-EARTH IONS IN III-V SEMICONDUCTORS

H .J. Lozykowski , Department of Electrical and Computer Engineering, and Condensed
Matter & Surface Sciences Program Ohio University Athens, Ohio 45701

ABSTRACT

In this work we have developed a model for the kinetics of the energy transfer from the host lattice to the localized core excited states of rare earth isoelectronic structured traps (REI-trap). We have derive a set of differential equations for semi-insulating semiconductor governing the kinetics of rare earth luminescence. The numerically simulated rise and decay times of luminescence show a good quantitative agreement with the experimental data obtained for InP:Yb, over a wide range of generation rates.

INTRODUCTION

The investigation of the luminescence properties of rare earth doped III-V is of great interest both from scientific and application points of view. The scientific interest is related to the uniqueness of optical and electrical properties of rare earth impurities in semiconductor hosts. Among the rare earth doped III-V semiconductors InP:Yb has been the most extensively studied [1-6]. In this paper we discuss only the structured isoelectronic traps (REI-trap) in III-V semiconductors introduced by RE^{+3} ions replacing the element from column III. Furthermore, we develop a model of the luminescence kinetic that describes the energy transfer from the host to the REI-trap core states, and the recombination and quenching processes. Study of the rise and decay times at different excitation intensities, temperatures, can provide important information about the energy transfer and recombination (radiative, and non-radiative) processes.

THEORETICAL FORMULATION

An isoelectronic center can form bound states because of a short range central-cell potential. According to Thomas [7], the primary factors affecting the binding potential are the electronegativity and the size differences between the impurity and the host ion which it replaces. It is found experimentally that only very large atoms or very small atoms produce isoelectronic traps because they create large lattice distortion induced by the substitution. The above conclusion is supported by the fact that the atomic covalent radii (ionic RE^{+3}) for all rare earths are bigger than atomic radii of Ga and In that they are replacing. Pauling's electronegativity of rare earth elements is in the range of 1.1-1.25, and is smaller than Ga (1.81) and In (1.78) for which it substitutes. If the rare earth ions replace the element from column III in III-V compounds (that are isovalent concerning outer electrons of RE^{+3} ions) , they create isoelectronic traps. The rare earth isovalent traps that we can call isoelectronic "structured" impurities [8] possess unfilled $4f^n$ core shells. The luminescence structure arises from intra-configurational f-f transitions in the core of the isoelectronic "structured" impurities.

The striking feature of excitons bound to the isoelectronic traps is a long luminescence decay time, ranging from a few hundred to few thousand nanoseconds [9,10-12]. The lifetimes of neutral donor or acceptor bound excitons in direct gap semiconductors are in the range of nanoseconds. The "simple" isoelectronic center in III-V materials can exist in three possible states instead of two as in the case of the Shockley-Read-Hall (SRH) recombination model [11]. In the case of rare earth isoelectronic traps, the kinetics model is even more complicated because of an energy transfer processes between the localized state in the forbidden gap of the host, and the localized core state of structured isoelectronic impurities. There are three possible mechanisms of energy transfer. The first is the energy transfer from excitons bound to "structured" isoelectronic centers to the core electrons. It takes place as a result of the electrostatic perturbation between the core electrons and the

398
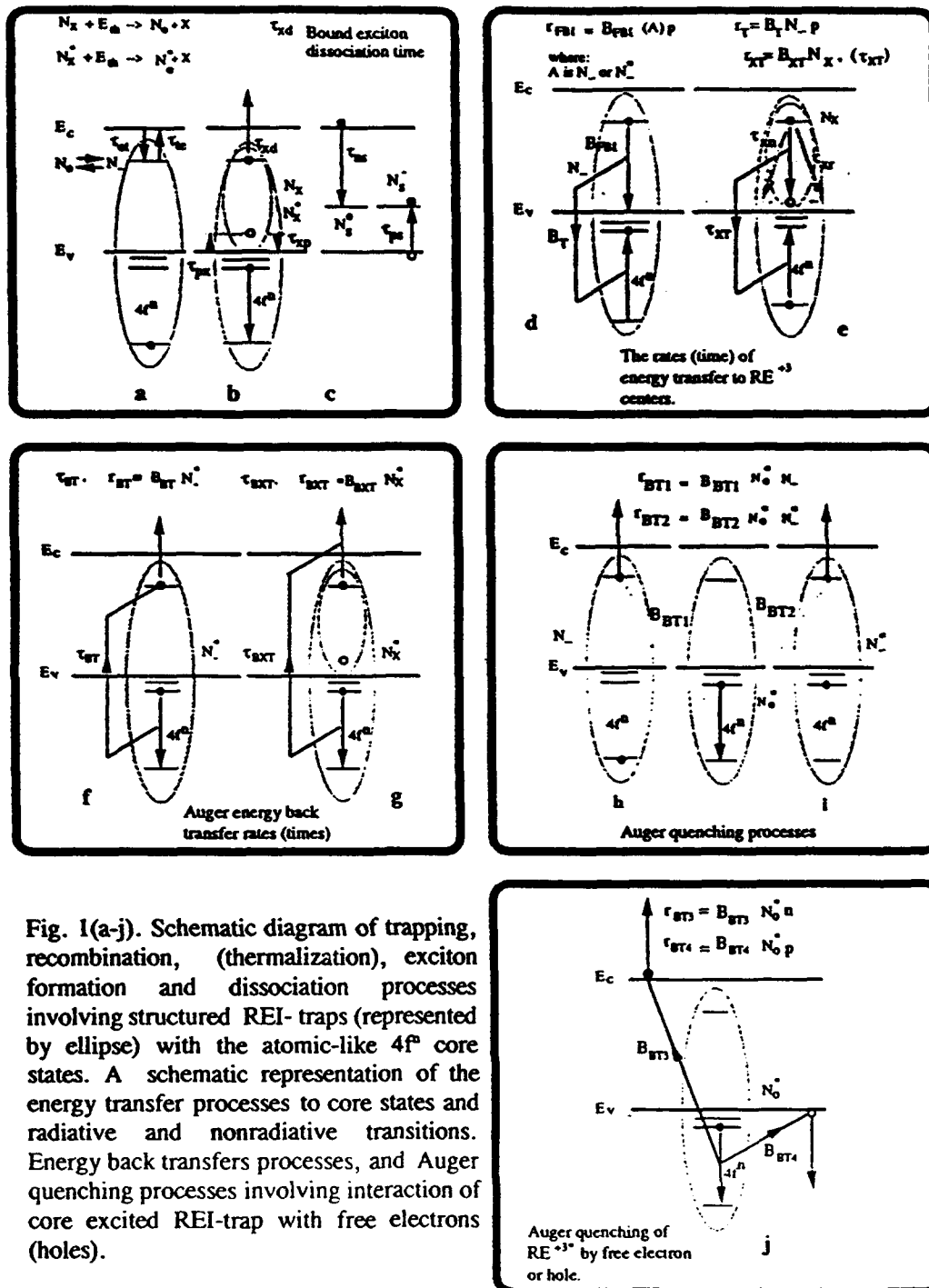
Fig. 1(a-j). Schematic diagram of trapping, recombination, (thermalization), exciton formation and dissociation processes involving structured REI- traps (represented by ellipse) with the atomic-like $4f^n$ core states. A schematic representation of the energy transfer processes to core states and radiative and nonradiative transitions. Energy back transfers processes, and Auger quenching processes involving interaction of core excited REI-trap with free electrons (holes).

exciton, (effective-mass-like particles) [8]. The second mechanism is the transfer of energy
to the core electrons involving the "structured" isoelectronic trap occupied by electron (hole)
and free hole (electron) in the valence (conduction) band. The third mechanism is the transfer
through an inelastic scattering process in which the energy of a free exciton near a
"structured" trap is given to the localized core excited states [8]. If the initial and final states
are not resonant, the energy mismatch must be distributed in some way, e.g. by phonon
emission or absorption [8,13]. If the atomic core excitations are strongly coupled to the host
phonons, the energy transfer probability is likely to be higher [8]. Strong phonon coupling
may also be desirable in ensuring that relaxation down the ladder of core excited states occurs
quickly, thus preventing back transfer. However, for efficient radiative recombination, the
phonon coupling should not be strong, in order to prevent core de-excitation by nonradiative
multiphonon emission. In this regard the rare earth "structured" impurity seems to be ideal.

KINETIC MODEL AND COMPUTATION RESULTS

The luminescence kinetic model involving RE^{+3} "structured" isoelectronic centers,
is complicated because the center can exist in six possible states. Furthermore the energy
transfer processes between the localized state in the forbidden gap and core states complicate
the model. We assume that the isoelectronic trap is an electron trap such as Yb^{+3} in semi-
insulating (SI) InP. This trap may exist in six distinct states: (1) neutral unoccupied trap
(concentration N_o), (2) negatively charged (concentration N_-), (3) exciton occupied
3(concentration N_x), (4) neutral excited (concentration N_o^*), (5) excited negatively charged
(concentration N_-^*), and (6) excited exciton occupied (concentration N_x^*). When isoelectronic
traps are present in n or p-type materials the model will be different. The asymmetry between
n and p type semiconductors results from the fact that the isoelectronic center binds only an
electron (hole). Thus in a n-type material, a fraction of the isoelectronic traps will be
occupied by electrons even before the sample is excited, while in p -type material, all the
isoelectronic centers will be empty . Figure 1 shows the physical models, symbols, and
definitions used in the analysis of excitation, recombination and quenching of "structured"
isoelectronic centers. By fitting the calculation to the experimental data, we can estimate
important parameters related to energy transfer from the lattice to RE^{+3} centers, the Auger
processes, and the temperature quenching mechanisms. The N_- center can be transformed
to the neutral rare earth core excited center N_o^*, through an Auger process where the
recombination energy of the bound electron with free hole is transferred nonradiatively to the
core states. The N_- may also recombine radiatively or nonradiatively with a hole in the
valence band. The last three processes transform N_- center into N_o neutral trap. The N_o^* may
capture an electron and be transformed into N_-^* center. The N_-^* may lose the electron through
processes described above, or by auto de-ionization Auger process. This Auger nonradiative
luminescence quenching mechanism of the excited REI-trap with characteristic time τ_{BT} is
shown in Fig.1f. The exciton bound to a REI-trap with excited core states (N_x^*), can back
transfer energy from core excitations to the exciton, and dissociate it, with the liberation of
an electron or hole. Once formed, the N_-, and N_-^* states can also be converted into N_o, and
N_o^* states, respectively, by thermal ionization or to N_x, and N_x^* , respectively, by capturing
a hole from the valence band with time τ_{px}. The second most important energy transfer
process is shown in Fig.1e. In this process energy is transferred from the bound exciton (on
isoelectronic trap N_x) to the core states with the rate r_{xT}. The exciton bound to isoelectronic
traps N_x and N_x^* can thermally dissociate by several processes. It can dissociate into a free
exciton (X) and neutral N_o, or neutral excited (N_o^*) REI-trap respectively. The REI-traps N_o^*,
N_-^* and N_x^* may also be de-excited to N_o, N_- and N_x respectively by radiative transitions
(time τ_3) between the $4f^n$, core states .The nonradiative decay channel of free carriers through
an additional type of trap N_s the "shunt path" is shown in Fig.1c. Figure 1.h,i,j show
examples of nonradiative recombination involving the interaction of a core excited REI-trap
(N_o^*) with an electron trapped on a separate center (N_-), an electron trapped on a core excited

$$\frac{dN_-}{dt} = \frac{n}{\tau_{ei}}\left(\frac{N_0}{N}\right) + \frac{N_-^*}{\tau_3} + \frac{1}{\tau_{xp}}\left(\frac{N_x}{N}\right)\frac{N_v}{\beta_h}\exp\left(-\frac{E_h}{kT}\right) - \frac{1}{\tau_{se}}\left(\frac{N_-}{N}\right)\beta_e N_c\exp\left(-\frac{E_t}{kT}\right)$$

$$- \frac{p}{\tau_{px}}\left(\frac{N_-}{N}\right) - B_{FB1}(N_-)p - B_T(N_-)p - B_{BT1}(N_0^*)N_- \tag{1}$$

$$\frac{dN_x}{dt} = \frac{N_x^-}{\tau_3} + \frac{p}{\tau_{px}}\left(\frac{N_-}{N}\right) - N_x\left(\frac{1}{\tau_2} + \frac{1}{\tau_{xT}} + \frac{1}{\tau_{xe}}\right) - \frac{1}{\tau_{xp}}\left(\frac{N_x}{N}\right)\frac{N_v}{\beta_h}\exp\left(-\frac{E_h}{kT}\right) \tag{2}$$

$$\frac{dN_0^*}{dt} = \frac{N_x}{\tau_{xT}} + B_T(N_-)p + \frac{1}{\tau_{se}}\left[\frac{N_-^*}{N}\right]\beta_e N_c\exp\left[-\frac{E_t}{kT}\right] - \frac{n}{\tau_{ei}}\left[\frac{N_0^*}{N}\right] - \frac{N_0^*}{\tau_3}$$

$$- B_{BT1}(N_0^*)N_- - B_{BT3}(N_0^*)n - B_{BT4}(N_0^*)p \tag{3}$$

$$\frac{dN_-^*}{dt} = \frac{n}{\tau_{ei}}\left(\frac{N_0^*}{N}\right) + \frac{1}{\tau_{xp}}\left(\frac{N_x^*}{N}\right)\frac{N_v}{\beta_h}\exp\left(-\frac{E_h}{kT}\right) - \left(\frac{1}{\tau_3} + \frac{1}{\tau_{BT}}\right)N_-^*$$

$$- \frac{p}{\tau_{px}}\left(\frac{N_-^*}{N}\right) - \frac{1}{\tau_{se}}\left(\frac{N_-^*}{N}\right)\beta_e N_c\exp\left(-\frac{E_t}{kT}\right) - B_{BT2}(N_0^*)N_-^* - B_{FB1}(N_-^*)p \tag{4}$$

$$\frac{dN_x^*}{dt} = \frac{p}{\tau_{px}}\left(\frac{N_-^*}{N}\right) - N_x^*\left(\frac{1}{\tau_2} + \frac{1}{\tau_3} + \frac{1}{\tau_{BXT}} + \frac{1}{\tau_{xd}}\right) - \frac{1}{\tau_{xp}}\left(\frac{N_x^*}{N}\right)\frac{N_v}{\beta_h}\exp\left(-\frac{E_h}{kT}\right) \tag{5}$$

$$\frac{dn}{dt} = G + N_x^*\left(\frac{1}{\tau_{xd}} + \frac{1}{\tau_{BXT}}\right) + \left(\frac{N_- + N_-^*}{N}\right)\frac{1}{\tau_{se}}\beta_e N_c\exp\left(-\frac{E_t}{kT}\right)$$

$$+ \frac{N_x}{\tau_{xd}} + \frac{N_-^*}{\tau_{BT}} - \frac{n}{\tau_{ei}}\left(\frac{N_0 + N_0^*}{N}\right) - \frac{n}{\tau_{ns}}\left(\frac{N_s^0}{N_s}\right) + B_{BT2}(N_0^*)N_-^* + B_{BT3}(N_0^*)N_- \tag{6}$$

$$\frac{dp}{dt} = G + \frac{1}{\tau_{xp}}\cdot\frac{N_v}{\beta_h}\exp\left(-\frac{E_h}{kT}\right)\left(\frac{N_x + N_x^*}{N}\right) - \frac{p}{\tau_{px}}\left(\frac{N_- + N_-^*}{N}\right) - \frac{p}{\tau_{ps}}\left(\frac{N_s - N_s^0}{N_s}\right)$$

$$- B_T(N_-)p - B_{FB}(N_- + N_-^*)p \tag{7}$$

$$\frac{dN_s^0}{dt} = \frac{p}{\tau_{ps}}\left(1 - \frac{N_s^0}{N_s}\right) - \frac{n}{\tau_{ns}}\left(\frac{N_s^0}{n_s}\right) \tag{8}$$

$$\left.\begin{array}{l} N_0 = N - N_- - N_x - N_0^* - N_-^* - N_x^* \\ N_s = N_s^0 + N_s^- \end{array}\right\} \tag{9}$$

$$p = n + N_- + N_-^* + \left(1 - \frac{N_s^0}{N_s}\right)N_s \tag{10}$$

Table I   Parameters Describing Rise and Decay Kinetics
of InP : Yb.

Symbol	Unit	Parameter Value
τ_2	sec	2×10^{-7}
τ_3	sec	11.6×10^{-6}
τ_{BT}	sec	1×10^{-7}
τ_{BTX}	sec	1×10^{-3}
τ_{ea}	sec	5×10^{-6}
τ_{ea}	sec	3×10^{-6}
τ_{XT}	sec	1.25×10^{-6}
τ_{ei}	sec	5×10^{-11}
τ_{ei}	sec	5×10^{-11}
B_T	cm³/sec	4×10^{-10}
B_{TW}	cm³/sec	1×10^{-11}
B_{BT1}	cm³/sec	1.2×10^{-13}
B_{BT2}	cm³/sec	1.2×10^{-13}
B_{BT3}	cm³/sec	4×10^{-13}
B_{BT4}	cm³/sec	4×10^{-13}
N_t	cm⁻³	8×10^{16}
N	cm⁻³	5×10^{17}
G	# photons / (cm³.sec)	$2 \times 10^{20} - 1.5 \times 10^{23}$
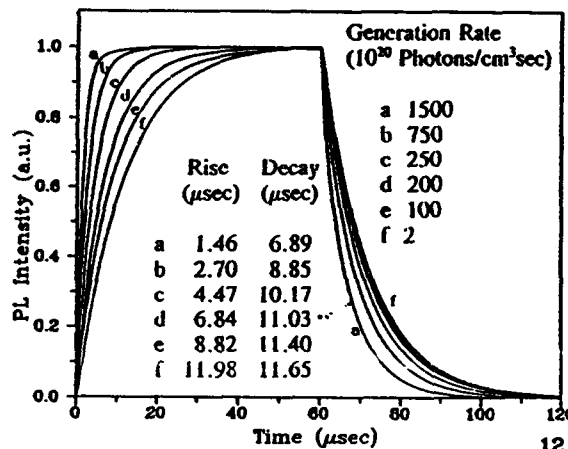
Fig. 2. Numerical solutions of Eqs.(1)-(10). The rare earth luminescence intensity versus time for the set of parameters shown in Table I. The set of computed profiles (normalized to unity at maximum), showing the buildup of luminescence, the steady state value, and the decay after switching off (at 60 μs) the excitation pulse.

	Rise (μsec)	Decay (μsec)
a	1.46	6.89
b	2.70	8.85
c	4.47	10.17
d	6.84	11.03
e	8.82	11.40
f	11.98	11.65

Generation Rate (10²⁰ Photons/cm³sec)

a	1500
b	750
c	250
d	200
e	100
f	2

Fig. 3 The numerically computed rise and decay times (solid lines) as a function of generation rates. The experimental values of rise times (circles-single exp. f.), (squares-double exp. f.) The dots stand for the decay times constant of the dominant component of the experimental data fitted to double exponential function.

Theoretical Decay (Solid)
Experimental Decay (•)

Decay

Rise

Theoretical Rise (Solid)
Experimental Rise : (o)Double, (■)Single
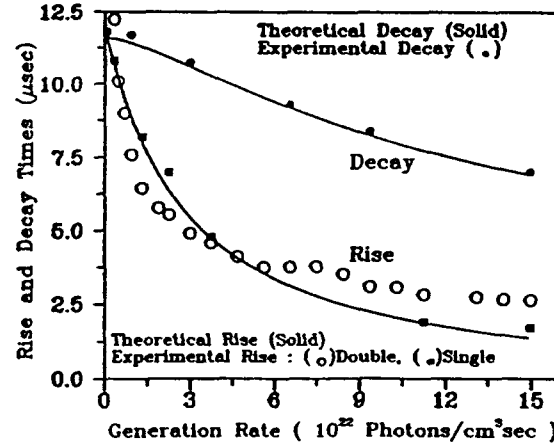
REI-trap (N$^-$), or the free electrons (holes) with Auger coefficients B_{BT3},(B_{BT4}) [14,15]. By consulting Figs.1, we can now complete the formal description of the model by deriving the differential equations for the REI-trap kinetics. To solve this system , we assumed, excitations take place at a low enough temperatures (8.6 K) that thermal activation of the trapped carriers is negligible. That is, terms explicitly dependent on temperature were ignored, and only trapping, transferring and recombination transitions were considered. The numerical solution of equations was obtained using the parameters shown in Table I by repeating the numerical calculations for different values of the generation rate. The luminescence intensities are proportional to N$^*_0$, N*, and N$^*_x$. Figure 2 shows the computed luminescence rise and decay as a function of the generation rate. In figure 3, the solid lines are the computed rise and decay times (the experimental data are imposed on the computed curves). The circles shown in Fig.3 represent the experimental rise time obtained from fitting to a single exponential function. The squares stand for the rise time of the dominant component of the experimental data fitted to double exponential function. The dots represent the experimental decay time of the dominant component of the double exponential fitting. The numerically simulated luminescence rise and decay measurements show a good quantitative agreement with experiment over a wide range of generation rates.

For n-type material the equations are even more complicated, similar equations hold for p-type material. Such systems of coupled, first order stiff nonlinear differential equations require specialized numerical integration routines designed specifically for stiff systems.

The detailed analysis of the parameters and their influences on the rise time, the efficiency of the steady state luminescence, and decay time will be published elsewhere. Finally, the proposed model can be refined by taking into account the surface recombination and carrier diffusion processes, which may play important roles in the reduction of the overall photoluminescence emission .

REFERENCES

1.   H.Ennen,G.Pomrenke and A.Axmann J.Appl. Phys. 57,2182,(1985).
2.   F.B.Klein, Solid State Commun. 65,1097,(1988).
3.   P.S.Whitney,K.Uwai,H. Nakagome, and K. Takahei, Appl.Phys. Lett., 53, 2074 (1988),
4.   K. Thonke, K. Pressel, G. Bohnert, A. Stapor, J. Weber, M. Moser, A. Malassioti, A. Hangleiter and F. Scholtz, Semicond. Sci. Technol., 5, 1124 (1990).
5.   C. Lhomer, B. Lambert, Y. Toudic, A. LeCorre, M. Gauneau, F. Clerotand, B. Sermage, Semicond .Sci .Technol .6, 916, (1991).
6.   H. J. Lozykowski, A. K. Alshawa, G. Pomrenke, and I. Brown, Bulletin American Phys. Soc. Vol. 36, C54, 2167, (1991), ibid., E 4.4.
7.   D. G. Thomas, J. of the Phys. Soc. of Japan, 21, 265 (1966).
8.   D.J.Robbins and P. J. Dean, Adv. in Physics, 27 (4), 499 (1978) and references therein.
9.   J. D. Cuthbert and D. G. Thomas, Phys. Rev., 154 (3), 763, (1967).
10.   J. Jayson, R. Bhargava, and R. Dixon, J. Appl. Phys., 41, 4972, (1970)
11.   J. M. Dishman and M. DiDomenico, Jr., Phys. Rev. B 1, 3381, (1970),
12.   J. S. Jayson and R. Z. Bachrach, Phys. Re. B., 4(2), 477, (1971)
13.   T. Holstein, S. Lyo,and R. Orbach, Excitation in Disorder Systems, in Laser Spect.of Solids, edited by W. Yen and P. Selzer, Springer-Verlag, Berlin, 1981, p., 39.
14.   J. M. Langer, Springer Proceedings in Physics Vol.38, Electroluminescence, Editors: S. Shionoya and H. Kobayashi Springer-Verlag, 1989 and references cited therein.
15.   J. M. Langer and Le Van Hong, J. Phys. C: Solid State Phys., 17, L923, (1984).

LUMINESCENCE PROPERTIES OF YB-DOPED INP

H. J. Lozykowski, A. K. Alshawa, Ohio University, Athens, Ohio. G. Pomrenke AFOSR /NE Bolling AFB, Washington,D.C., and L. Brown, Lawrence Berkeley Laboratory, University of California at Berkeley.

ABSTRACT

The photoluminescence, time resolved spectra and kinetics of Yb implanted InP samples are studied under pulsed and CW excitations (above and below band-gap) at different temperatures and excitation intensity. The photoluminescence intensity and decay time as a function of temperature is explained by a proposed new quenching mechanism involving Fe ion. The rise and decay times depend on excitation intensity. The above experimental facts was explained using the kinetics model developed by H.J. Lozykowski [2]. The numerically simulated luminescence rise and decay times show a good quantitative agreement with experiment, over a wide range of generation rates. The electric field InP:Yb photoluminescence quenching was investigated and reported for the first time.

INTRODUCTION

There has been increasing interest in rare earth doped semiconductor compound because of their potential for light emitting device applications. Beside the application aspect, the rare earth impurities are of great interest from the scientific point of view. Scientific interest is related to the uniqueness of optical and electrical properties of rare earth impurities in semiconductor hosts. Among rare earth ions are those that upon replacing the element from column III in III-V compounds that are isovalent, concerning outer electrons of RE^{+3} ions, create isoelectronic traps in III-V semiconductors. This conclusion is supported by the fact that the atomic covalent radii (ionic RE^{+3}) for all rare earth are bigger than atomic radii of Ga and In that they replace [2]. Pauling's electronegativity of rare earth elements is in the range of 1.1-1.25, and is smaller than Ga (1.81) and In (1.78) for which it substitutes. The rare earth isovalent traps (REI-trap) that we can call isoelectronic "structured" impurities [1,2] possess the unfilled $4f^n$ core shell. The structured luminescence arises from intra-configurational f-f transitions in the core of the isoelectronic "structured" impurities. Ytterbium in InP replaces indium on a substitutional site [3] and acts as an isoelectronic trap. It was originally proposed by Whitney at al [4] and confirmed by others [5a,b] that the Yb ion creates an electron trap at 30 meV below the bottom of conduction band. Recently, admittance spectroscopy [5b] was used to identify the electrical activity of Yb in n and p type InP. It was found that Yb in InP creates a hole trap at 50 meV above the valence band, and an electron trap at 29 meV below the conduction band.

SAMPLES AND MEASUREMENT RESULTS

The InP material was produced from Fe-doped, semi-insulating iron doped InP. Samples D and E were implanted using a novel high current metal ion implantation facility in which a metal vapor vacuum arc (MEVVA) ion source is used. The Yb was implanted with mean ion energy $\approx$ 140 keV and the dose (5-10) $\times 10^{13}$ ion/cm^2 (peak at $\sim$370 Å from the surface, concentration 1.8x10^{19} cm^{-3}). Sample D and E were annealed for 10 minutes at 600 $^\circ$C and 680 $^\circ$C, respectively. Sample C was implanted using ion beam energy of 1 MeV and dose of 3 $\times 10^{13}$ ion/cm^2(peak at 1960 Å from the surface, concentration 1.46x10^{18} cm^{-3}). The sample was annealed at 650 $^\circ$C for 15 minutes.

The photoluminescence spectra of InP:Yb (sample C) shown in Fig.1 was recorded at 8.5 K. The emission intensity of sample C is the highest of the three samples. The spectrum of each sample consists of one sharp peak at 1001 nm and broader overlapping peaks at 1005.5 nm and 1007 nm corresponding to the $^2F_{5/2}$-$^2F_{7/2}$ transitions. The inset of
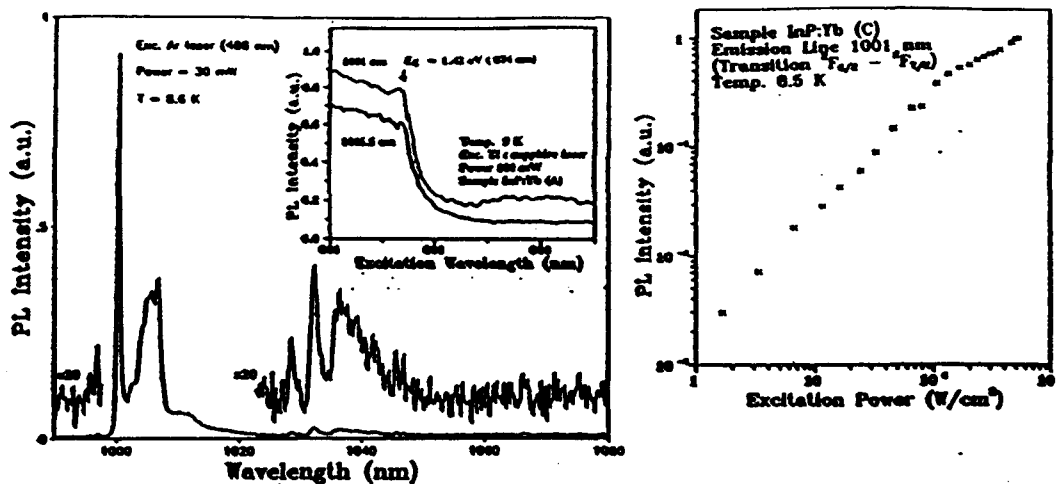
Fig. 1 PL Spectra of InP:Yb (sample C) The inset shows the excitation spectra.

Fig. 2 The PL intensity of InP:Yb (at 1001 nm) as a function of excitation power.
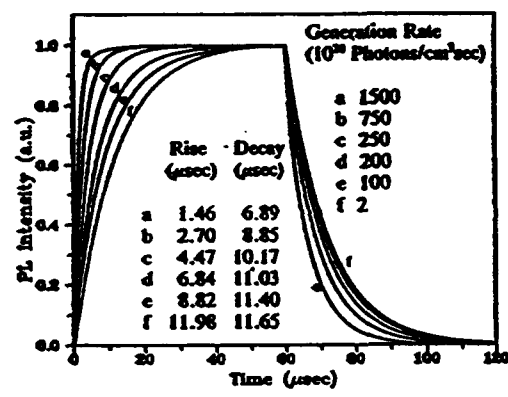

Fig. 3 The computed luminescence rise and decay for different generation rates.

Fig. 4 The calc. and experimental rise and decay times as functions of the generation rate.

Fig. 1 shows the excitation spectra recorded at emission lines 1001 nm and 1005.5 nm. In Fig. 2, the intensity of 1001 nm peak was measured as a function of the excitation power. The PL kinetics measurements were investigated at different excitation intensities and temperatures. The experiment shows that the rise and decay times are function of excitation intensity. The above experimental facts were explained using the kinetics model developed by H.J. Lozykowski [2]. To adequately describe the kinetics of the energy transfer from the host to REI-trap, the buildup and decay kinetics of rare earth luminescence (as the function of excitation intensity), we have to consider six separate states of the REI-trap (for details see [2]). The energy transfer processes occur through: a) transfer of energy from the bound exciton on REI-trap to the core states, and b) by Auger mechanism where the recombination energy of the bound electron with free hole is transferred nonradiatively to the core states. If the initial and final states are not resonant (in both mechanisms), the energy mismatch must be accommodated by emission or absorption of phonons [1,6]. In SI InP:Yb the kinetics are described by a set of differential equations which were solved assuming low temperature. That is, terms explicitly dependent on temperature were ignored, and only trapping, transferring and recombination transitions were considered. The numerical solution of the differential equations was obtained by repeating the numerical calculations for different generation rates. Fig. 3 shows the computed luminescence rise and decay as a

function of the generation rate. In Fig. 4, the solid lines are the computed rise and decay times (the experimental data are imposed on the computed curve). The circles shown in Fig.4 represent the experimental rise times obtained from fitting to single exponential function. The squares stand for the rise times of the dominant component of the experimental data fitted to double exponential function. The dots represent the experimental decay times of the dominant component of the double exponential fitting. The numerically simulated luminescence rise and decay measurements show a good quantitative agreement with experiment over a wide range of generation rates.

The time resolved spectra (TR, Fig. 5) was recorded at temperatures 8.5K, 20K and 40K for different time delays from 0.0 to $30\mu s$ (for 8.5 K) and from 0.0 μs to 25 μs for temperatures 20K and 40K. The time resolved emission spectra of the main peak at 1001nm (I_1) shows changes in the emission line width and also slight change in the position of the peak. The positions and the widths of the emission lines recorded at long time after the excitation pulse were changed compared to those measured just after the excitation pulse. The excitation energy seems to move within the regular Yb^{3+} and slightly distorted ion system, and also between Yb^{3+} and other accidental impurities where the energy is dissipated nonradiatively. At this point it is reasonable to introduce the hypothesis of energy transfer from Yb^{3+} to iron or other accidental impurities. The energy transfer process from Yb^{3+} to Fe ions is attributed for thermal quenching of the ytterbium luminescence intensity and decay time decrease with temperature increase . Crystals used in our investigation were semi-insulating InP doped with Fe (concentration $> 2x10^{16}cm^{-3}$) and implanted with Yb. Iron is a common contaminant in MOCVD Yb doped InP semiconductor. Uwai et al. [7] presented the SIMS analysis of MOCVD grown $InP:Yb^{3+}$ that showed a flat ytterbium incorporation profile for a total Yb^{3+} concentration of about $6x10^{18}$ cm^{-3}. The SIMS spectra also reveals significant amounts (10^{16} cm^{-3} or higher) of Fe and Mn, elements that were not present in undoped layers, and which probably appear from contaminated ytterbium [$Yb(C_5H_5)_3$] source. Also Williams[8] , found an evidence for impurities such as Fe and Mn which, did not appear in undoped samples. The iron contamination of InP:Yb is probably very common to most of the investigated samples in literature.

The excellent review of optical properties of iron doped InP (absorption, photoluminescence, photoconductivity and photoluminescence excitation spectra) was recently published by S. Bishop[9]. The first level scheme of Fe^{+3} ion in InP was proposed by Stauss et al [10] to explain the photo quenching spectra of Fe^{3+} ESR signal with onset at 0.75 eV,
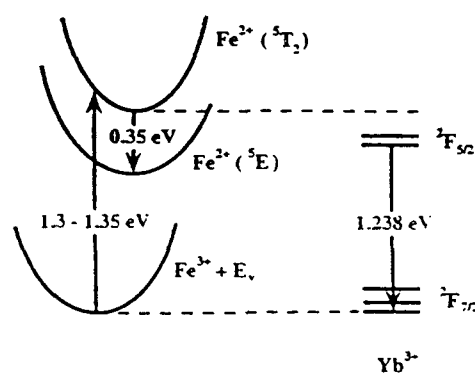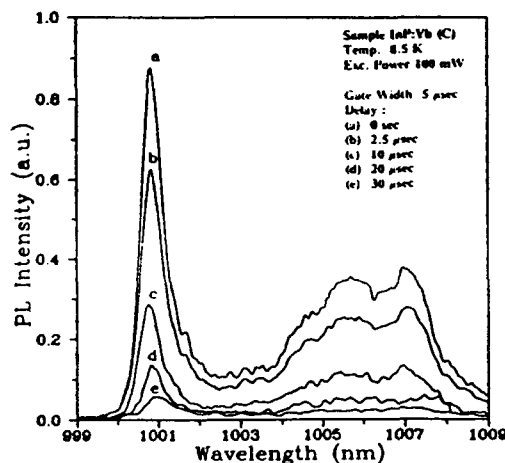

Fig. 5   Time-resolved spectra of InP:Yb, sample(C),   for different time delays.

Fig. 6   The energy levels schemes for Yb^{3+} and (Fe^{3+} - Fe^{2+}) in SI InP.
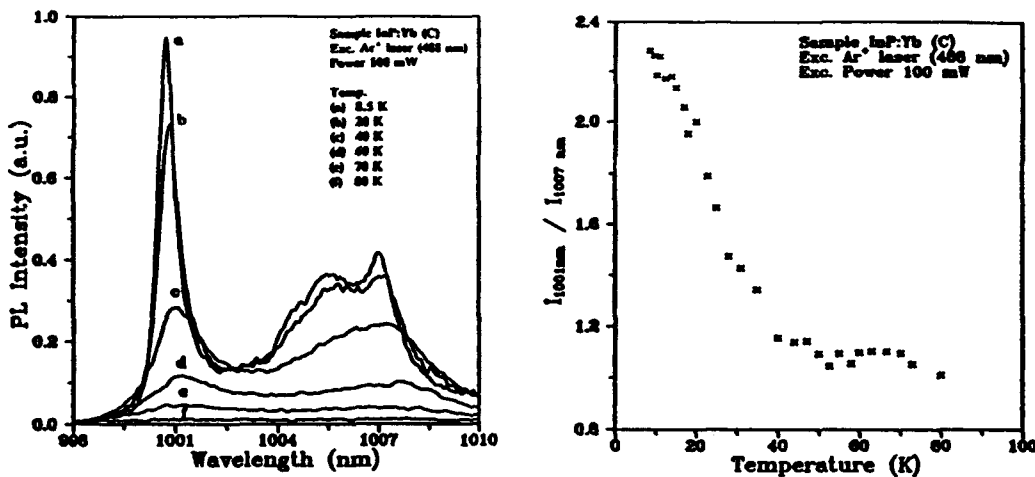
Fig. 7 Temperature dependance of the PL spectra of InP:Yb in the range 8.5 K-80 K.
Fig. 8 The intensity ratio of the emission lines1001 nm to 1005.5 nm.

a shoulder near 1.13 eV, and maximum between 1.2 eV and 1.4 eV . These thresholds (at 0.75 eV and 1.13 eV) were attributed to direct transfer of electrons from the valence band to Fe^{3+} which converts it to the ground state of Fe^{2+} (^5E) or to excited state of Fe^{2+} ($^5T_2$) respectively. Bishop [11] and Leyral [12] observed the photoluminescence of Fe^{2+} (^5E) at 0.35 eV by extrinsic excitation (PLE) peaking at the excitation energy between 1.3eV and 1.35 eV. In conclusion according to Bishop et al.[11] the extrinsic excitation of the Fe^{2+} ($^5T_2$) photoluminescence is attributed to a ligand-to-metal charge transfer transition in which a valence electron from an adjacent phosphorus atom is transferred to a Fe^{3+} ion, creating an Fe^{2+} in the excited $^5T_2$ state. The energy levels scheme for Yb^{3+} ($4f^{13}$ in cubic symmetry T_d) and schematic configuration coordinate diagram for the (Fe^{3+}- Fe^{2+}) in SI InP is shown in Fig. 6. Furthermore, the energy levels schemes show the 0.35 eV luminescence attributed to the Fe intracenter transition ($^5T_2 \rightarrow$ ^5E), and energy transfer from Yb^{3+} to Fe^{3+} via the $^2F_{5/2}$ state of Yb ion. Excitation of Fe^{2+} photoluminescence at 0.35 eV is due to an electron capture by Fe^{3+} giving a Fe^{2+} in the excited $^5T_2$ state which, relaxes radiatively to the ^5E (Fe^{2+} ground state). The structured infrared (0.35eV) PL emission attributed to transition $^5T_2$ $\rightarrow$ ^5E exhibits exponential decay. At 10 K the decay time constant for semi-insulating sample is 8.8 μs , and for n type sample is 10.5 μs which corresponds to the lifetime of the $^5T_2$ excited state [13]. The lifetime of $^5T_2$ excited state decreased quickly with increasing temperature, and at 50 K it is 6.6 μs. The Yb^{3+} ($^2F_{5/2}$ -$^2F_{7/2}$) emission occurs in the region 1.229-1.242 eV and overlaps the broad extrinsic absorption band of Fe^{3+} , a requirement for efficient energy transfer. The quenching of Yb^{+3} characteristic PL (integrated) emission intensity and the decay time was investigated as a function of temperature. Fig. 7 shows the photoluminescence spectra of InP:Yb as a function of the temperature in the range 8.5 - 80 K. Fig. 8 shows the ratio of the integrated intensity I_1 (area under peak at 1001nm)to the integrated intensity I_2 (area under broad peak at 1007 nm) as a function of temperature for sample C. The ratio decreases from 2.3 at 8.6K to about 1.15 at 40K and remains constant till 80K. Figure 9 shows that the Yb^{3+} PL integrated intensity as a function of temperature remains approximately constant between 8.6 and 55 K, above which it decreases rapidly with further increase of temperature. The experimental data (for 1001nm peak) was fitted to equation show in Fig. 9 and plotted with theoretical fitting (solid line) using parameters E_A ≈ 100 meV, E_B ≈ 7.57 meV, a=0.9, b=1.66x10^{11} and c=11.25. The experimental data are well fitted and explained by the above simple model in which the excited Yb^{3+} ions lose their energy via the $^2F_{5/2}$ to the $^5T_2$ of Fe^{2+} ion (quenching trap). Activation energy E_A = 100 meV obtained from the experimental data is in good agreement with the gap between
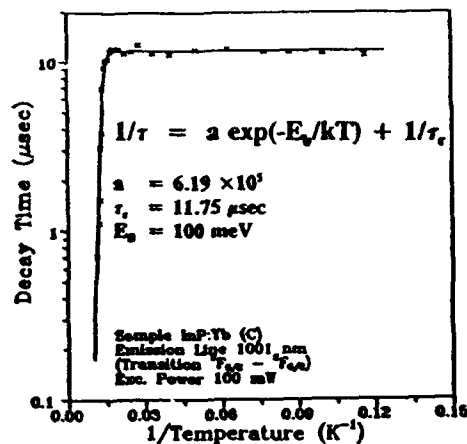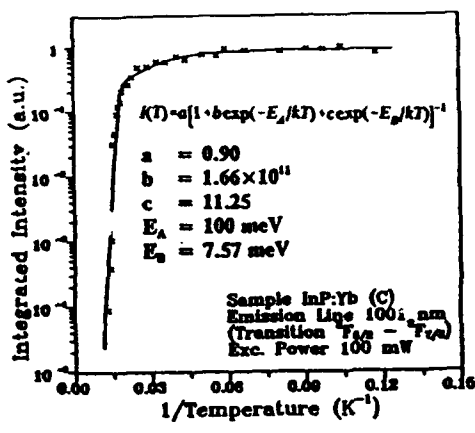
Fig. 9   A fit of the PL intensity of InP:Yb versus temperature.
Fig. 10   A fit of the experimentall decay times versus temperature.

the $^2F_{5/2}$ upper Stark level of Yb^{3+} and the excited level $^5T_2$ of Fe^{2+}. The energy of the excited Fe^{2+} ($^5T_2$) ion is lost via the $^5T_2 \rightarrow ^5E$ photon or multiphonon emissions. A similar simple model describes the relaxation rate $R_r = 1/\tau$ (decay time) of the Yb^{3+} luminescence as a function of temperature shown in Fig. 10 The relaxation rate $(1/\tau)$ as a function of temperature is given by the equation shown in Fig. 10 where the activation energy E_a $=100$ meV, is approximately the separation between $^2F_{5/2}$ (Yb^{3+}) and $^5T_2$ levels, and a $=$ 6.19×10^5 sec^{-1}. The $\tau_r = 11.75$ μsec is the decay time of Yb^{3+} at very low temperature. The lifetime of $^5T_2$ (Fe^{3+}) excited state decreased quickly with increasing temperature and at 50 K it is 6.6 μs [13]. At all temperatures investigated, the Fe^{2+} ($^5T_2$) lifetime is shorter than the Yb^{3+} lifetime, therefore Fe^{3+} is appropriate to serve as an energy sink for Yb^{3+} excitation. As mentioned above, the energy transferred from Yb^3 to Fe^{3+} ion is lost via the $^5T_2 \rightarrow ^5E$ (0.35eV) photon (or multiphonon) emission. The temperature dependence of the PL intensity of the $^5T_2 \rightarrow ^5E$ transition should show some increase at the temperature where the Yb^{3+} ($^2F_{5/2} \rightarrow ^2F_{7/2}$) emission intensity drastically decreases (experiment in progress). If the outcome of the experiment will be positive it will give an additional direct proof of the proposed new quenching mechanism.

The width of the emission line 1001 nm as a function of temperature is shown in Fig. 11. The line shape in the temperature range 9-80 K is described by a convolution of a Lorentzian and Gaussian functions (the Voigt contour). The emission line is homogeneously broadened with the Lorentzian as the dominant component ($\sim 90\%$) of the line shape . The width of the experimental homogeneous component as a function of temperature is plotted together with theoretical curve using the equation shown in Fig. 12. The equation in Fig.12 is typical for a single-phonon relaxation process with absorption of a phonon of energy ΔE. The fitting parameters are: $\Delta E = 5.976$ meV is the energy difference between the level 5 and 4 [3], a=0.65meV and b=11.44. The estimated energy $\Delta E = 5.976$ meV is close to the TA zone boundary phonons energy TA(L) $= 6.82$meV (TA(X) $= 8.478$ meV), in InP [14].

The effect of the electric field on the PL of InP:Yb was studied for the first time.To perform this experiment, a semi-transparent gold electrode (100 Å) was deposited on the implanted surface of InP, a second thick gold electrode (500 Å) was deposited on the opposite side of the sample. Figure 12 shows the quenching of PL of Yb^{3+} emission as a function of the applied electric field at both polarities. Assuming uniform absorption , the excitation photons are absorbed within the surface layer where a strong electric field exists. The quenching of PL of Yb^{3+} can be explained by two possible mechanisms : (1) exciton
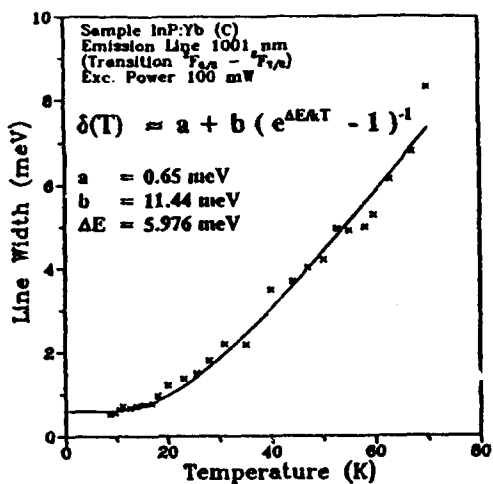
Fig. 11   The temperature dependance of the line width of the emission line 1001 nm.
Fig. 12   The PL intensity of InP:Yb as a function of the applied DC voltage.
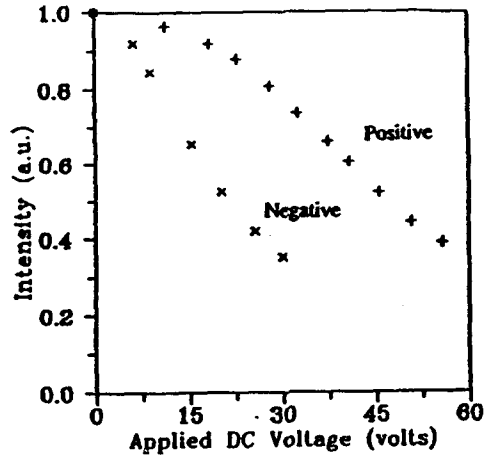
bound to the isoelectronic trap dissociation by hot electron impact ionization or (2) swept of electrons or holes to the Au-InP interface where they will recombine nonradiatively.

REFERENCES :

[1] D. J. Robbins and P. J. Dean, Adv. in Physics, 27 (4), 499, (1978) and references

[2] H.J. Lozykowski, Phys Rev. (in press)

[3] J. Wagner, J.Windscheif, and H.Ennen, Phys.Rev.B, 30, 6230, (1984)

[4] P. S.Witney, K.Uwai, H. Nakagome, and K. Takahei, Appl. Phys. Lett.,21, 2074,(1988)

[5a] D. Seghier, T. Benyattou, G. Bremond, F. Ducroquet, J. Gregoire, G. Guillot, C. Lhomer, B. Lambert, Y. Toudic, and A. Le Corre, Appl. Phys. Lett. 60, 983, (1992),

[5b] B.Lambert,A.Le Corre, Y. Toudic, C. Lhomer, G. Grandpierre and M. Gauneau, J. Phys. Condens. Mater 2, 479, (1990).

[6] T. Holstein, S. K. Lyo, and R. Orbach, Excitation in Disorder Systems, in Laser Spectroscopy of Solids, edited by W. M. Yen and P. M. Selzer, Springer-Verlag, Berlin, 1981, p.39.

[7] K. Uwai, H. Nakagome, and K. Takahei, Appl. Phys. Let., 50, 977, (1987)

[8] D.M. Williams and B.W.Wessels Appl.Phys. Lett.,56,566,(1990)

[9] S. Bishop, Iron Impurity Centers in III-V Semiconductors in Deep Centers in Semiconductors A State-of-the-Art Approach, Second Edition, Edited by S.T. Pantelides, Gordon and Breach Science Publishers, Philadelphia 1992.

[10] G. H Stauss, J. J. Krebs, and R. L. Henry, Phys. Rev. B16, 974, (1977)

[11] S. G. Bishop, P. B. Klein, R. L. Henry, and McCombe, in G. J. Rees (Editor)Semi-Insulating III-V Materials , (Shiva, Orpington, 1980), p. 161.

[12] P. Leyral, G. Bremond, A. Nouailhat, and G. Guillot, J.of Lum., 24/25, 245, (1981).

[13] P. B. Klein, J. E. Furneaux, and R. L. Henry, Phys. Rev. B29, 1947, (1984).

[14] P. H. Borcherds, G. F. Alfrey, D. H. Saunderson, and A. D. B. Woods, J. Phys C : Solid State Phys., 8, 2022, (1975).

Luminescence Properties of Yb- and Nd- Implanted CdS

A. K. Alshawa, H. J. Lozykowski, T. Li, Ohio University, Department of Electrical and Computer Engineering, Athens, OH. ; and I. Brown, University of California, Berkeley, Lawrence Berkeley Laboratory, Berkeley, CA

ABSTRACT

The photoluminescence (PL) and time resolved spectra of Nd- and Yb-implanted CdS samples are studied under pulsed and CW excitations using Ar^+ ion laser for different excitation intensities and temperature (9 - 300 K). The samples were annealed under different conditions using the thermal-pulse method. For CdS:Nd, the PL spectra was recorded in the range 890-930 nm (transitions $^4F_{3/2} \rightarrow ^4I_{9/2}$) and for CdS:Yb it was recorded in the range 985 - 1010 nm (transitions $^2F_{5/2} \rightarrow ^2F_{7/2}$). The Rise time and decay time were studied for both CdS:Nd and CdS:Yb at different emission lines as a function of temperature and excitation power.

INTRODUCTION

The photoluminescence properties of rare earth (RE) ions in II-VI semiconductor compounds have been of interr · for many years. The light emission due to radiative transitions in the partially occupied $4f$ shell of RE^{3+} ions in the form of lines and narrow bands is the basis for numerous applications such as solid state lasers. Beside the application aspect, the rare earth impurities are of great interest from scientific point of view. Scientific interest is related to the uniqueness of optical and electrical properties of rare earth impurities in semiconductor hosts. It is well known that the rare earth luminescence depends very little on the nature of the host and the temperature. The 4f orbits of rare earth ions incorporated in semiconductors are so deeply buried within the electronic shell that the energy levels of the $4f$ configuration are only slightly perturbed compared to free ion energy levels. The electronic structure of the rare earth luminescence centers and their electrical activities, as well as their indirect photoluminescence excitation mechanisms are still not well understood. The luminescence of rare earth doped cadmium sulphide has been reported by many researchers[1-4]. The attempt was to explain the mechanisms of exciting the RE^{3+} in CdS. In [1], Kingsley and et al, proposed that the energy is transferred from luminescence centers (in his case, copper) to the rare earth ions. Anderson [2] proposed that the transfer of energy is due to the electronic transition between donor-acceptor levels. In this paper, we report the luminescence properties of Nd^{3+} and Yb^{3+} implanted in CdS. Time resolved spectra was recorded for Nd^{3+} and Yb^{3+} in the ranges 890-930 nm (transitions $^4F_{3/2} \rightarrow ^4I_{9/2}$) and 985-1010 nm (transitions $^2F_{5/2} \rightarrow ^2F_{7/2}$), respectively. The term assignments for these transitions are obtained from [5]. The PL spectra was investigated at different temperatures in the range 8.5 - 300 K. Rise time and decay time processes were also studied as a function of temperature and excitation intensity.

SAMPLES AND MEASUREMENT

The implantation of Yb and Nd was performed with an unconventional technique using a new kind of high current metal ion source. The implantation dosage was 7.5×10^{13} cm^{-2} and the mean ion energy was 150 keV for Nd and 140 keV for Yb. In the CdS:Nd sample, the concentration of Nd is 1.31×10^{19} cm^{-3} and the peak -to-surface depth is 412 Å. For Yb, the concentration is 1.38×10^{19} cm^{-3} and the peak-to-surface depth is 390 Å. Both samples were annealed at 900 °C for 15 seconds using a Thermal-Heat-Pulse method. The photoluminescence (PL) was excited by the 488 nm line from a argon ion laser (Laser Ionics Model 553A). The pulsed excitation for time resolved spectra (TRS) was obtained by

acousto-optic light modulator (IntraAction Model AOM-125). The samples were mounted on a cold finger cooled by a close-cycle helium cryostat down to 8.5 K. The emission was dispersed by a Jarrel Ash Model 78-490, 0.75 M, scanning monochrometer equipped with a 1180 grooves/mm grating. The detecting electronics consists of a Hamamatsu R632-01 photomultiplier with spectral response extended to IR region. The signal from the photomultiplier is amplified by a fast preamplifier and then fed to a dual-channel gated photon counting system controlled by a computer, which also control the scanning monochromator. The photoluminescence kinetics (rise and decay) were measured with exceptional accuracy using Turbo-Multi Channel Scaler (Turbo-MCS, EG&G Ortec) which offers a wide range of channel dwell times (minimum 5ns), with no deadtime between channels.

RESULTS AND DISCUSSION

The Photoluminescence spectra of CdS:Nd and CdS:Yb was recorded at 8.5 K in the spectral range 895 - 930 nm (1.385-1.335 eV) and 985-1010 nm (1.26-1.225 eV), respectively. For CdS:Nd, the spectrum consists of about nine sharp peaks corresponding to the transitions between Stark levels $^4F_{3/2}$ - $^4I_{9/2}$. The PL spectrum of CdS:Yb consists of six sharp peaks around 988 nm (1.255 eV) and two broader peaks at 995.6 nm (1.245 eV)
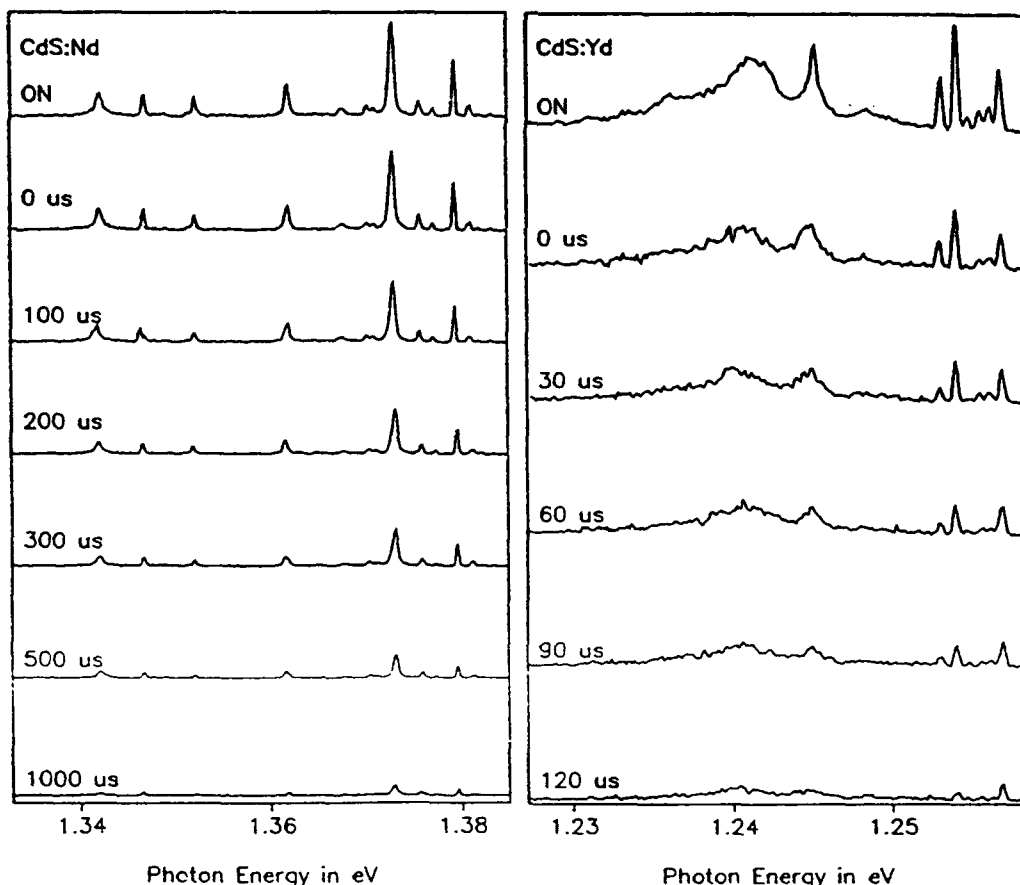
Figure 1. The Time Resolved Spectra (TRS) of (a) CdS:Nd and (b) CdS:Yb at T=8.6 K. The gate widths are 100 µsec. The delays are as indicated in each spectrum. The spectra labeled ON are measured with gate and excitation pulse overlapped.

and 998.8 nm (1.241 eV). The Yb^{3+} emission peaks correspond to the $^2F_{5/2}$ - $^2F_{7/2}$ transitions. The time resolved spectra were recorded at 8.6 K for different delay times from 0 to 1000 μsec for Nd and from 0 to 120 μsec for Yb as shown in figure 1. For CdS:Nd, the intensity of all emission lines decreased with delay uniformly. In the case of CdS:Yb the intensities of the emission lines at 986 nm (1.257 eV), 995.6 nm (1.245 eV) and 998.8 nm (1.241 eV) decreased slower than the other lines.

The PL spectra were investigated as a function of temperature in the range 8.5 - 300 K for Nd and 8.5- 150 K for Yb. In figure 2a, the intensity of all lines of CdS:Nd stayed fairly constant from 8.5 to 35 K then fill down until no emission was observed after 100 K.
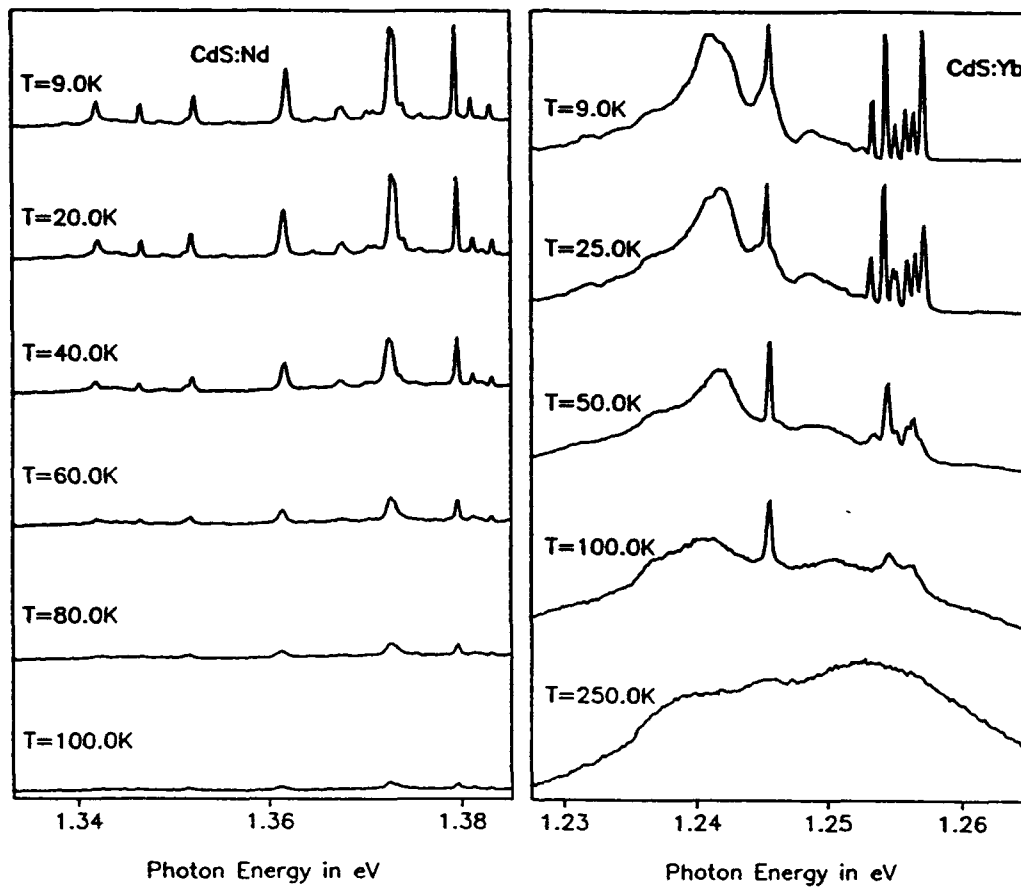
Figure 2. Temperature dependence of the PL spectra of (a) CdS:Nd and (b) CdS:Yb excited by Ar^+ laser at 488 nm with 80 mW power.

The integrated intensity of the emission line 903 nm (1.372 eV) is plotted versus temperature as shown in figure 3a. From figure 2b, the PL intensity of Yb sharp emission peaks decreases with the temperature increase until 40 K and started to increase with temperature until it reached a maximum at around 55 K. Then started to decrease with further increase in temperature. This behavior is clear from figure 3b where the integrated intensity of the emission line 995.6 nm (1.245 eV) is plotted as a function of temperature. Another observation is that with the increase of temperature, the sharp peaks evolved into one broad emission band at the same range of wavelength.

In figure 3a the decay characteristic of the Nd^{3+} $^4F_{3/2}$ integrated emission intensity is shown. The experimental data of the temperature dependance (at peak 903 nm) was fitted to the relationship:

$$I(T) = I(0)\left[1 + A_1 e^{-\frac{E_1}{kT}}\right]^{-1}$$ (1)

The experimental result is plotted with theoretical fitting (solid line) using the parameters $E_1 = 72.4$ meV, $I(0) = 0.99$ and $A_1 = 3.5 \times 10^4$.
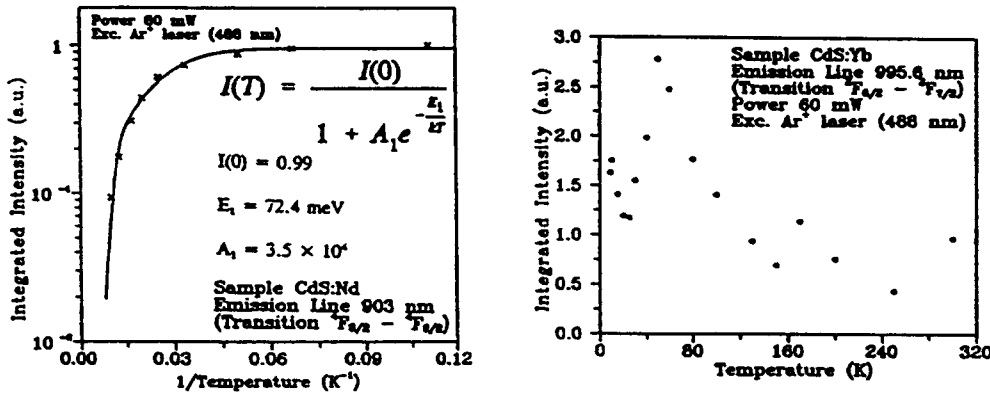

Figure 3. PL integrated intensity of (a) CdS:Nd at emission line 903 nm and (b) CdS:Yb at emission line 995.6 nm versus temperature. For (a) CdS:Nd the solid line is a fit to the experimental data using the relation discussed in the text.

The widths of the Nd emission line at 903 nm (1.372 eV) and Yb emission line at 995.6 nm (1.245 eV) as functions of temperature are shown in figure 4. The line shapes of both samples were described by a Gaussian (inhomogeneously broadened) function in the forementioned temperature range. The experimental line widths for both Nd and Yb as functions of temperature shown in figure 4 (a & b, respectively) are plotted together with the theoretical curves using equation :

$$\delta(t) \approx a + b\left(e^{\frac{\Delta E}{kT}} - 1\right)^{-1}$$ (2)
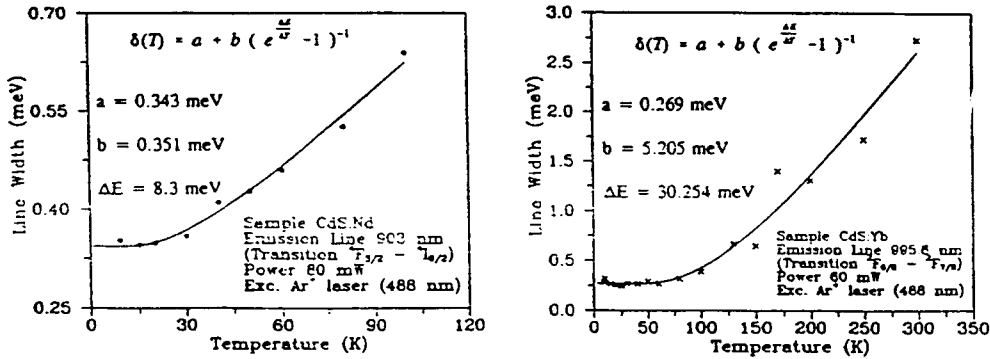
Figure 4. The temperature dependence of line widths of (a) CdS:Nd at 903 nm and (b) CdS:Yb at 995.6 nm.

For Nd, $\Delta E=8.3$ meV, a=0.343 meV and b=0.351 meV, and for Yb, $\Delta E=30.254$ meV, a=0.269 meV and b=5.205 meV. The above equation describing the width of the emission line as a function of temperature, is typical for a single-phonon relaxation process with absorption of a phonon of energy $\Delta E=8.3$ meV ($E_{TA}=9.0$meV in CdS) for Nd, and $\Delta E=30.254$ meV ($E_{TO}=30.0$ meV in CdS) for Yb.

The rise time and decay time of Nd and Yb were investigated as functions of temperature and excitation power. Figure 5 shows the decay time of Nd at emission peak 903 nm (1.372 eV) as a function of temperature.
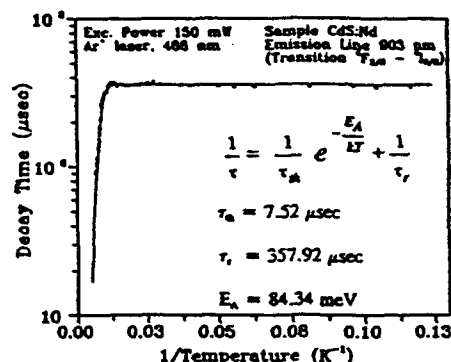
Figure 5. A fit (solid line) of the time decay CdS:Nd at emission line 903 nm to the experimental data (crosses) as a function of temperature.

The decay time remains constant around 357 μsec from 8.6 to 50 K and after it falls down below 100 μsec at 100 K. The decay time, , as a function of temperature is given by the equation

$$\frac{1}{\tau} = \frac{1}{\tau_{th}} e^{-\frac{E_A}{kT}} + \frac{1}{\tau_r} \qquad (3)$$

where $E_A = 84.34$ meV, $\tau_{th} = 7.52$ μsec and $\tau_r = 357.92$ μsec where τ_r is the decay time at very low temperature. The activation energy $E_A = 84.34$ meV is close to the activation energy $E_1 = 72.4$ meV obtained from the decay characteristics of the integrated intensity as a function of temperature. For Yb, the decay time of the emission line 995.6 nm (1.245 eV) remained constant around 90 μsec for the entire range of temperature of 8.6 - 100 K.

In figure 6, The rise times of both Nd and Yb, were studied as functions of excitation power in the range 1 - 400 W/cm^2. The rise time of Nd at 903 nm (1.372 eV) decreased from 556 μsec to 300 μsec as the excitation power was increased from 1 W/cm^2 to 400 W/cm^2 as shown in figure 6a. For Yb (figure 6b), the rise time at 988.2 nm (1.254 eV) decreased from 97 μsec to 23.5 μsec as the excitation power was increased from 1 W/cm^2 to 400 W/cm^2. The rise time decrease with the excitation power increase indicates that the mechanism of exciting the RE is indirect.

The PL intensities of CdS:Nd (at emission line 903 nm) and CdS:Yb (at emission line 988.2 nm) were recorded at different excitation powers in the range 1-400 W/cm^2. From figure 7, we can see that the intensities increase linearly with the excitation power until 100 W/cm^2 and then start to saturate.

In order to interpret our results more thoroughly and provide explanations for   rgy transfer and kinetics processes, more investigation is needed, such as ⌐   .on measurements, excitation spectra, and the electroluminescence.

286
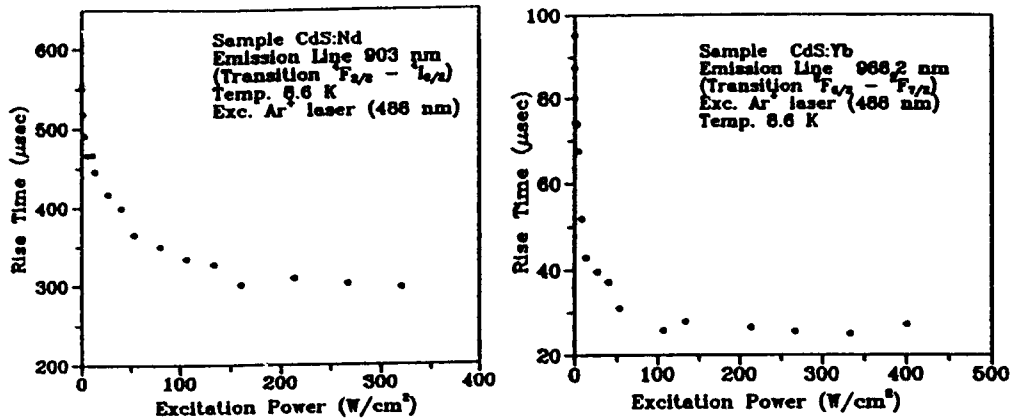
Figure 6. The rise times of (a) CdS:Nd at 903 nm and (b) CdS:Yb at 988.2 nm as functions of the laser excitation power.
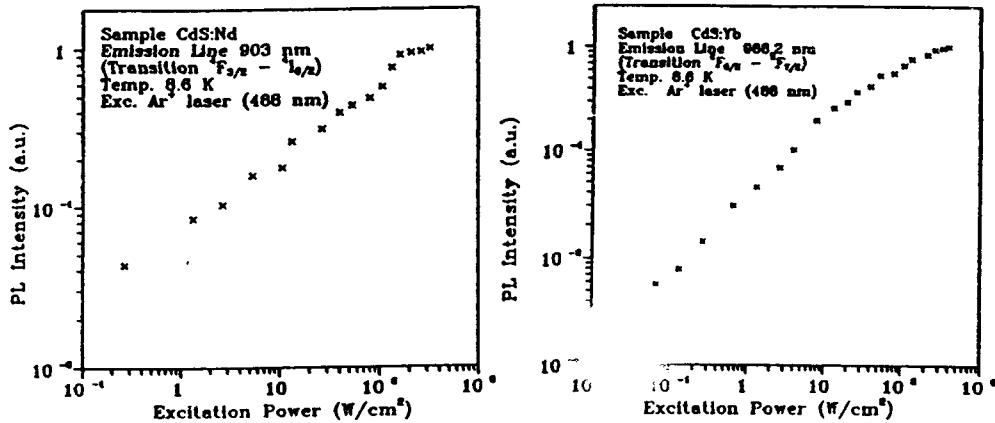

Figure 7. The PL intensities of (a) CdS:Nd at 903 nm and (b) CdS:Yb at 988.2 nm as functions of the laser excitation power

REFERENCE

[1] J. D Kingsley, J. S. Prener, and M. Aven, Phys. Rev. Letters 14, 136 (1964)
[2] W. W. Anderson, J Chem. Phys. 44, 3283 (1966)
[3] J. Apperson, W. E. Lamb, and B. Lunn, Infrared Phys. 8, 241 (1968)
[4] J. Apperson, G. F. J. Garlick, W. E. Lamb, and B. Lunn, Phys. Stat. Sol. 34, 537 (1969)
[5] G. H. Dieke and H. M. Crosswhite, Appl. Optics 2, 675 (1963)

Digital spectropolarimeter for the measurement of optical polarization

H. J. Lozykowski,[a] T. Li, and Z. I. Akir

Electrical and Computer Engineering Department, Ohio University, Athens, Ohio 45701

A computerized setup for optical polarization measurements is described. The heart of this setup is a photoelastic modulator (PEM) whose retardation phase can be kept constant when the wavelength of modulated light is scanned in a wide range, and a dual-channel gated photon counter which has the capability of compensating the variation of excitation intensity with time and wavelength. Unlike conventional analog setups, where the difference of two perpendicularly polarized light components $(I^+ - I^-)$ and the average of these components $\frac{1}{2}(I^+ + I^-)$ are extracted electronically and the ratio $2(I^+ - I^-)/(I^+ + I^-)$ is recorded as degree of polarization, this spectropolarimeter directly records the I^+ and I^- components (for circular polarization) or $I_{\parallel}$ and $I_{\perp}$ components (for linear polarization) of the analyzed light signal. Once the spectra of the two components are stored as a numerical file in the computer, they can be processed to extract the degree of polarization as a function of wavelength, temperature, etc. The curvature and asymmetry of the modulator response are taken into account exactly in data processing. The spectropolarimeter has proved to be very accurate due to the capability of compensating the fluctuation in excitation source and of electronically tracking the modulation wavelength.

I. INTRODUCTION

Optical orientation (or optical pumping) measurement has been a very useful tool in physical, chemical, and biochemical resea ch[1-3] because of its sensitivity, selectivity, and accuracy. In this article, we describe a computerized setup for optical polarization measurements. This setup consists of a photoelastic modulator (PEM) whose retardation phase can be kept constant even when the wavelength of the modulated light is scanned in a wide range, and a dual-channel gated photon counter which can compensate the variation of excitation intensity with time and wavelength. Unlike conventional analog setups, where the difference of two perpendicularly polarized light components $(I^+ - I^-)$ and the average of these components $\frac{1}{2}(I^+ + I^-)$ are extracted electronically and the ratio $2(I^+ - I^-)/(I^+ + I^-)$ is recorded as degree of polarization, this spectropolarimeter directly records the I^+ and I^- components (for circular polarization) or $I_{\parallel}$ and $I_{\perp}$ components (for linear polarization) of the analyzed light signal in the same run of wavelength, temperature, etc. The spectra of the two components are stored as a numerical file in a computer and can be further processed to extract the degree of polarization as a function of wavelength, temperature, etc.

II. PRINCIPLE

The circular or linear polarization of an optical signal can be analyzed by inserting a $\lambda/4$ retarder and a linear polarizer (or, for linear polarization, simply a linear polarizer) between the source and the detector. To measure the degree of circular polarization, one alternately sets the linear polarizer $+45°$ and $-45°$ with the fast axis of the retarder so that σ^+ and σ^- components of the signal can be detected alternately. For linear polarization, the retarder is removed and the linear polarizer is set $+45°$ and $-45°$ to the horizontal so that $I_{\parallel}$ and $I_{\perp}$ can be measured alternately. The degree of polarization is defined as

$$\rho = \frac{I^+ - I^-}{I^+ + I^-}. \tag{1}$$

For circular polarization, I^+ is the intensity of right-hand circular polarization (σ^+) and I^- is the intensity of left-hand circular polarization (σ^-). For linear polarization, I^+ and I^- stand for the beam polarized along the $+45°$ and $-45°$ axes, respectively.

The automatic spectropolarimeters utilizing the mechanically rotating polarizer and analog lock-in techniques are described in many publications.[4,5] There are two main drawbacks of this technique. First, the response of devices such as the monochromator's grating and the photomultiplier depends on the polarization of the incoming light, and this can induce error in the measured degree of polarization [Eq. (1)]. The second is the nonachromaticity of the retarder. To overcome these limitations, a fixed analyzer and a modulated retarder are put in series with their optical axes 45° apart. The retardation is modulated such that the retardance A is a function of time given by

$$A = A_0 \sin(2\pi\nu t), \tag{2}$$

where A_0 is proportional to the driving voltage and ν is the modulation frequency. Now that a fixed analyzer is used, the photomultiplier as well as the grating of the monochromator are exposed to only one state of linear polarization and hence the dependence of their response on the polarization of incoming light has no effect on the accuracy of the measurements.

[a] On Faculty Fellowship Leave at the Electronic Technology Laboratory (WRDC/EL), Wright Research and Development Center, Wright-Patterson Air Force Base, Dayton, OH 45433.
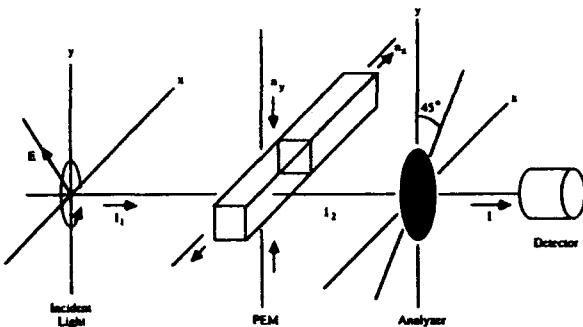
FIG. 1. Basic setup for analyzing the circular polarization of light. I_1 and I_2 are the intensity of the light before and after the modulator, respectively. I is the intensity seen by the detector. n_x and n_y are the refraction indices in the x and y directions.

To assure a constant retardation for different wavelengths, an electronic compensation system was designed.

Figure 1 illustrates this setup. The standard electromagnetic field complex vector analysis given by Kemp[6] is followed here. The transmitted intensities I^+ and I^- for σ^+ and σ^- circularly polarized light, respectively, are given by

$$I^{\pm} = |a|^2 [1 \pm \sin(A_0 \sin 2\pi\nu t)], \tag{3}$$

where $(+)$ stands for σ^+ and $(-)$ for σ^-. To see I^+ and I^- alternately at a given wavelength, one controls the driving voltage of the PEM modulator to obtain $A_0 = \pi/2$ at all wavelengths. Hence the PEM acts like a $+\lambda/4$ and $-\lambda/4$ plate alternately. Accordingly, Eq. (3) becomes

$$I^{\pm} = |a|^2 [1 \pm \sin(\pi/2 \sin 2\pi\nu t)]. \tag{4}$$

Figure 2 shows the plot of Eq. (4) where the solid line is for σ^+ and the dashed line is for σ^-. It is clear from Fig. 2 that Eq. (4) has symmetric features and if the photon counters A and B are gated as shown in the figure, the degree of polarization will be

$$\rho \approx \frac{A-B}{A+B}. \tag{5}$$

For an incident beam linearly polarized along $\pm 45°$ to the vertical, the transmitted intensities are given by
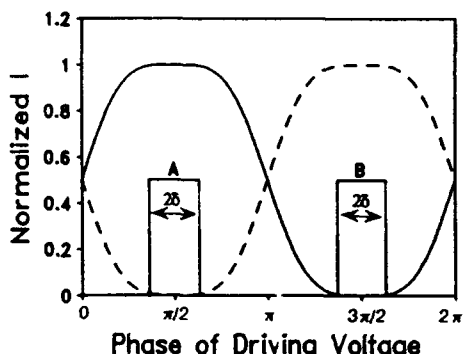
FIG. 2. The theoretical response of the PEM-analyzer system to circularly polarized light. The solid line is for σ^+, the dashed line is for σ^-, and 2δ is the gate width for the counters A and B.
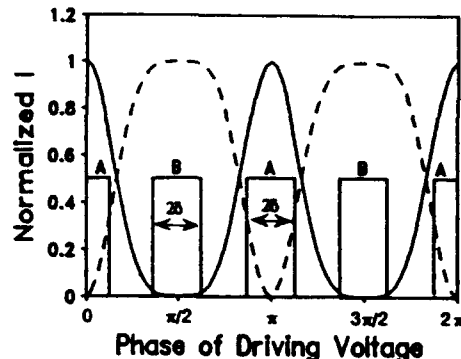


FIG. 3. The theoretical response of the PEM-analyzer system to linearly polarized light. The solid line is for $I(+45°)$, the dashed line is for $I(-45°)$, and 2δ is the gate width for the counters A and B.

$$I(\pm 45°) = |a|^2 [1 \pm \cos(A_0 \sin 2\pi\nu t)]. \tag{6}$$

To see $I(\pm 45°)$ beams alternately at a given wavelength, we control the driving voltage of the PEM modulator to obtain $A_0 = \pi$ at all wavelengths and hence the PEM acts alternately as an achromatic $+\lambda/2$ and $-\lambda/2$ retarder. Accordingly, Eq. (6) becomes

$$I(\pm 45°) = |a|^2 [1 \pm \cos(\pi \sin 2\pi\nu t)]. \tag{7}$$

The plot of Eq. (7) is shown in Fig. 3 where the solid line is for $I(+45°)$ and the dashed line is for $I(-45°)$. It can be seen from the figure that the two curves show asymmetric features. In the conventional lock-in technique, additional electronic circuits are needed to process this asymmetric wave form, which also requires that the PEM be switched on and off (enabled and disabled).[3] In our system, we deal with this marked asymmetry numerically. Suppose that photon counters A and B are gated as shown in Fig. 3 and the incident beam has two components $I(+45°)$ and $I(-45°)$. From Eq. (7), the counts in A and B are written as

$$A = \eta_A \left(\frac{1}{2} I(+45°) \int_{\pi-\delta}^{\pi+\delta} [1+\cos(\pi \sin x)] \, dx \right.$$
$$\left. + \frac{1}{2} I(-45°) \int_{\pi-\delta}^{\pi+\delta} [1-\cos(\pi \sin x)] dx \right) \tag{8}$$

$$B = \eta_B \left(\frac{1}{2} I(+45°) \int_{\pi/2-\delta}^{\pi/2+\delta} [1+\cos(\pi \sin x)] \, dx \right.$$
$$\left. + \frac{1}{2} I(-45°) \int_{\pi/2-\delta}^{\pi/2+\delta} [1-\cos(\pi \sin x)] \, dx \right), \tag{9}$$

where 2δ is the gate width and η_A and η_B are effective system efficiencies which are proportional to the transmissivity of the monochromator, the efficiency of the photomultiplier, the gain of the preamplifier, and the counter's threshold. In the system, A and B are actually using the same detecting system (monochromator, photomultiplier, and preamplifier), and if the detection thresholds of the counters are matched:
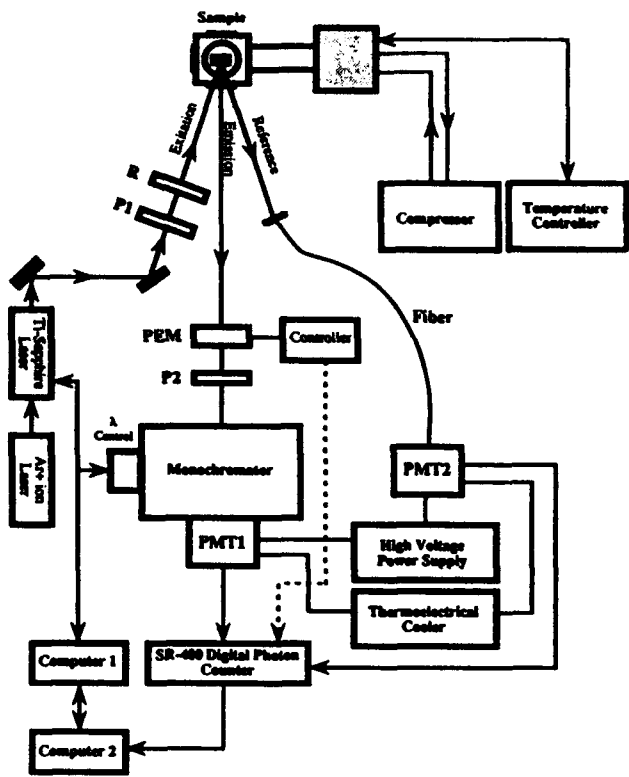
FIG. 4. Block diagram of the spectropolarimeter. $P1$, $P2$ are linear polarizers, R is an achromatic $\lambda/4$ retarder. PEM is a photoelastic modulator, and PMT1 and PMT2 are photomultiplier tubes.

$$\eta_A = \eta_B = \eta. \tag{10}$$

Normally what we are interested in is the ratio of the signal; so in the following we are going to drop this factor, η. Using the parity of the function $\cos(\pi \sin x)$ and ignoring η, Eqs. (8) and (9) can be written as

$$A = \delta[I(+45°)+I(-45°)] + \alpha[I(+45°)-I(-45°)], \tag{11}$$

$$B = \delta[I(+45°)+I(-45°)] + \beta[I(+45°)-I(-45°)], \tag{12}$$

where

$$\alpha = \int_{\pi}^{\pi+\delta} \cos(\pi \sin x)dx, \tag{13}$$

$$\beta = \int_{\pi/2}^{\pi/2+\delta} \cos(\pi \sin x)dx. \tag{14}$$

Equations (11) and (12) can be put in a matrix form:

$$\begin{bmatrix} \delta & \alpha \\ \delta & \beta \end{bmatrix} \begin{bmatrix} I(+45°)+I(-45°) \\ I(+45°)-I(-45°) \end{bmatrix} = \begin{bmatrix} A \\ B \end{bmatrix}, \tag{15}$$

which gives

$$\rho = \frac{I(+45°)-I(-45°)}{I(+45°)+I(-45°)} = \frac{\begin{vmatrix} \delta & A \\ \delta & B \end{vmatrix}}{\begin{vmatrix} A & \alpha \\ B & \beta \end{vmatrix}}. \tag{16}$$

Equations (13) and (14) can be evaluated numerically for a given δ.

Similar treatment should be made for the circularly polarized case especially when the signal is weak and a wide gate is needed. In that case

$$\rho = \frac{\delta}{\gamma} \cdot \frac{A-B}{A+B}, \tag{17}$$

where

$$\gamma = \int_{\pi/2}^{\pi/2+\delta} \sin\left(\frac{\pi}{2}\sin x\right)dx. \tag{18}$$

When the signal is strong and δ can be very small, $\gamma \approx \delta$ and Eq. (17) simplifies to Eq. (5).
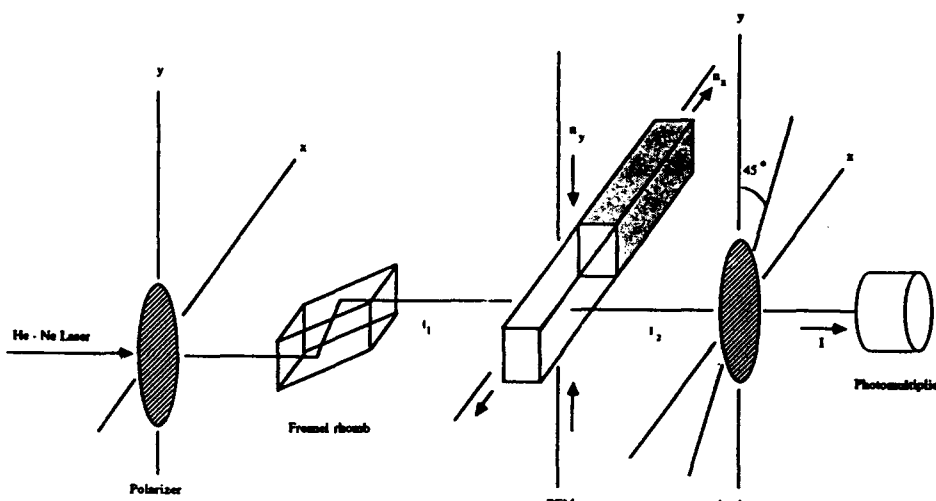

FIG. 5. Setup used to test the performance of the PEM modulator-analyzer system. The polarization state of the incident beam is defined by the orientation axis of the polarizer and the Fresnel rhomb.
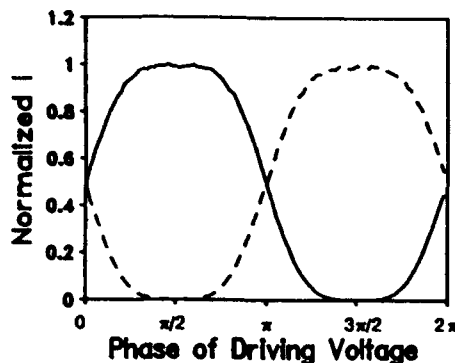
FIG. 6. Measured response of the spectropolarimeter to two input monochromatic beams (λ=632.8 nm) circularly polarized σ^+ and σ^-. The solid line is the response to σ^+ and the dashed line to σ^- circular polarization. The gate width and step size are set to 0.2 μs.

FIG. 8. Geometry used to simulate the partially polarized light. The linear polarizer is rotated φ° away from 45° to the fast axis of the retarder.

III. INSTRUMENTATION

Figure 4 shows the block diagram of the setup. The monochromatic light from the Ar$^+$ ion laser (or Ti:sapphire laser or dye laser pumped by Ar$^+$ laser), which is already linearly polarized by the Brewster output window, is retarded by the λ/4 achromatic retarder (R) to get circularly polarized excitation light. For an experiment that requires linear polarization, one can instead use the original laser beam or a λ/2 achromatic retarder. If the excitation light is from a lamp, a monochromator and a linear polarizer (P_1) are to be used in front of the quarter (half) wave achromatic retarder (R). For a linearly polarized excitation light, the quarter wave retarder is removed and a λ/2 achromatic retarder is used to rotate the polarization plane. The samples are mounted in a closed cycle cold finger cryostat. Small angles between the excitation beam and the quantization axis of the sample, and between this latter and the direction of observation (detection) are preferred for circularly polarized optical pumping studies.[7] Different arrangement of the excitation beam and the sample's orientation have been used for linear polarization studies.[8,9] The emission (or optical signal such as transmission, reflection, etc.) from the sample is modulated by a

photoelastic modulator (PEM) whose modulation depth (retardance) is electronically controlled to follow the wavelength of the signal being measured. A second polarizer (P_2) is used to analyze the modulated light. The light emerging from P_2 is then dispersed by a monochromator and detected by a photomultiplier (PMT1). The electric signal from PMT1 is amplified by a fast preamplifier and then fed into a dual-channel gated photon counter which is capable of compensating the fluctuation of excitation intensity. To sense the variation of excitation intensity, the incident beam is split and coupled into a second photomultiplier (PMT2) through the optical fiber. The output of PMT2 is preamplified and then fed into a photon counter to determine the counting period.

In the photon counter (SR-400) system, there are three fast counters: A, B, and T, all of which operate at rates up to 200 MHz. Counter T is presetable and determines the counting period for counters A and B which may be synchronized to external events via two independent gate generators. The gate generators provide gates from 5 ns to 1 s in duration with a delay from an external trigger ranging from 25 ns to 1 s. The counting period is the time it takes the counter T to reach its present count. If N_t is the preset count in counter T, and R_a, R_b, and R_t are the mean pulse rates of the inputs to counters A, B, and T, then the counting period is
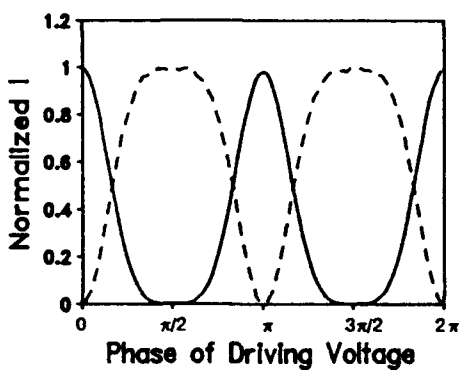
FIG. 7. Measured response of the spectropolarimeter to two input monochromatic beams (λ=632.8 nm) linearly polarized $I(+45°)$ and $I(-45°)$. The solid line is the response to $I(+45°)$ and the dashed line to $I(-45°)$ linear polarization. The gate width and step size are set to 0.2 μs.
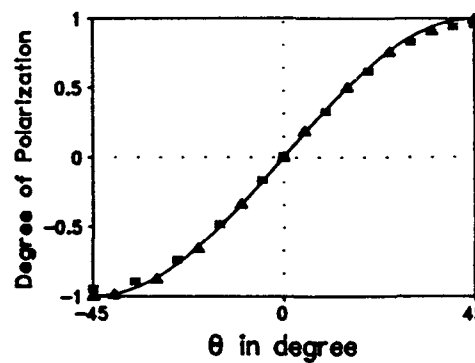
FIG. 9. Comparison of the theoretical curve calculated from Eq. (31) (solid line) and the experimental measurements for partially polarized light. (•) for linear polarization and (▲) for circular polarization.
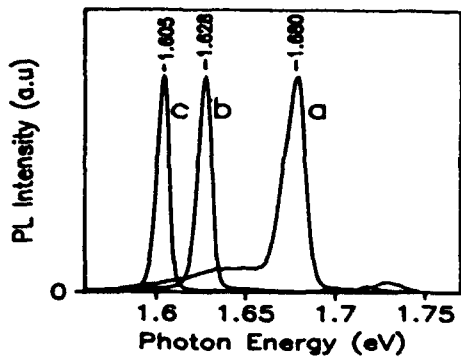
FIG. 10. Photoluminescence of $Cd_{0.79}Zn_{0.21}Te/CdTe$ strained-layer quantum wells. (a) $L_w = 25$ Å, (b) $L_w = 50$ Å, (c) $L_w = 75$ Å.

FIG. 11. Circularly polarized excitation spectra for $Cd_{0.79}Zn_{0.21}Te/CdTe$ strained-layer quantum well with $L_w = 75$ Å. Curve (a) σ^+, curve (b) σ^-, and curve (c) the degree of polarization ρ.

$$\tau = N_t / R_t \tag{19}$$

The number of counts in counters A and B will be

$$A = R_a \cdot \frac{N_t}{R_t}, \tag{20}$$

$$B = R_b \cdot \frac{N_t}{R_t}. \tag{21}$$

Since N_t is a constant in the above equations, the number of counts in counters A and B are proportional to the ratio of the rates R_a/R_t and R_b/R_t, respectively. If the input of counter T monitors the excitation intensity, the counting period will compensate for the fluctuation in the excitation source.

Once counter T reaches its present count, all the counters are "stopped" and the computer is instructed to read the data and adjust the driving voltage of the PEM as well as the wavelength (depending on the application, other parameters may be adjusted during this time). When everything is stabilized, all counters are reset and the next counting period is initiated. All other components in the setup are standard.

IV. PERFORMANCE

Figure 5 shows the test setup. The spectropolarimeter was tested using the He-Ne laser 632.8-nm line which was 100% circularly polarized by the linear polarizer and the achromatic Fresnel rhomb. The plots in Fig. 6 were recorded when the linear polarizer was set at $+45°$ and $-45°$ from the fast axis of the retarder (σ^+ and σ^-) and the gate of counter A is scanned with 0.2 μs in gate width and delay increment. The solid (dashed) line shows the intensity of $\sigma^+ (\sigma^-)$ circularly polarized beam versus the phase angle of the driving voltage. A similar test was also done for linearly polarized light and the results are plotted in Fig. 7. It is clear that the experimental results in Figs. 6 and 7 match the theoretical results shown in Figs. 2 and 3.

As shown in Fig. 8, partially polarized light can be simulated by rotating the linear polarizer away from 45° to the fast axis of the retarder. The degree of polarization with a rotated angle φ can be written as
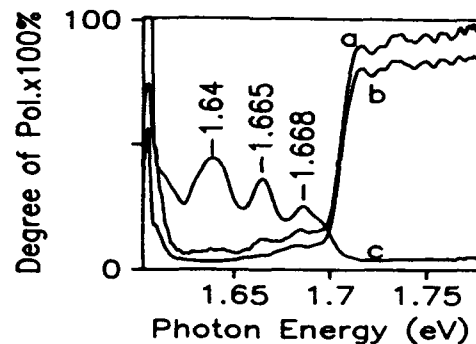
$$\rho = \frac{I^+ - I^-}{I^+ + I^-} = \frac{\cos^2 \varphi - \sin^2 \varphi}{\cos^2 \varphi + \sin^2 \varphi}$$

$$= \cos 2\varphi = \sin 2\theta \quad (-45° < \theta < 45°). \tag{22}$$

Equation (22) is valid for both circular and linear polarization. Partial linear polarization was tested with $\delta = \pi/5$ (and hence $\alpha = 0.3120$, $\beta = -0.6056$) in Eq. (16) and partial circular polarization was tested with $\delta = \pi/4$ (and hence $\gamma = 0.7684$) in Eq. (17). The results are compared with Eq. (22) in Fig. 9 where the solid line is the theoretical curve given by Eq. (22). The superimposed symbols (*) and (▲) are the experimental data for linear and circular polarization, respectively.

The setup of the apparatus shown in Fig. 4 has been used for photoluminescence spectra (PL), excitation spectra (PLE), and optical pumping studies of $Cd_{1-x}Zn_xTe/CdTe$ strained layer single quantum wells. Figures 10 and 11 show the PL and circularly polarized excitation spectra of a $Cd_{1-x}Zn_xTe/CdTe$ ($x=0.21$) strained-layer single quantum wells with well thicknesses of $L_w = 25$, 50, and 75 Å recorded at $T=9.0$ K. The PL spectrum in Fig. 10 was measured using the 488-nm line of an Ar^+ ion laser as the excitation source when the detected wavelength was scanned. The circularly polarized excitation spectra in Fig. 11 were detected at the longer wavelength side of the peak at 1.6 eV of the PL spectra (Fig. 10) when the excitation photon (circularly polarized σ^+) energy from the cw Ti-sapphire laser was scanned. Curves a and b show the σ^+ and σ^- components of the excitation spectra, respectively, for the quantum well with $L_w = 75$ Å. Curve c in Fig. 11 is calculated by Eq. (5) since the signal was strong enough to use narrow gates ($\delta = \pi/5$). Detailed discussion of the PL, PLE, and optical pumping studies of $Cd_{1-x}Zn_xTe/CdTe$ strained-layer single quantum wells is published separately.[7]

ACKNOWLEDGMENTS

[1] F. Meier and B. P. Zakharchenya, eds., *Modern Problems in Condensed Matter Sciences, Vol. 8: Optical Orientation* (North-Holland, 1984).

[2] F. S. Richardson and J. P. Riehl, Chem. Rev. 77, 773 (1977).

[3] J. E. Wampler and R. J DeSa, Analytical Chem. 46, 563 (1974).

[4] I. Z. Steinberg and B. Ehrenberg, J. Chem. Phys. 61, 3382 (1974).

[5] R. R. Parsons, Can. J. Phys. 49, 1850 (1971).

[6] I. C. Kemp, HINDS International, Inc., Polarized Light and its Interaction with Modulating Devices, A Methodology Review.

[7] T. Li and H. J. Lozykowski (to be published).

[8] J. Y. Marzin, M. N. Cherasse, and B. Sermage, Phys. Rev. B 31, 8298 (1985).

[9] A. J. Wojtowicz and H. J. Lozykowski, ACTA Physica Polynica A 54, 867 (1978).

Optical properties of CdTe/Cd₁₋ₓZnₓTe strained-layer single quantum wells

T. Li

Electrical and Computer Engineering Department, Ohio University, Athens, Ohio

H. J. Lozykowski*

*Electronic Technology Laboratory (WRDC/EL), Wright Research and Development Center,
Wright-Patterson Air Force Base, Dayton, Ohio 45433*

John L. Reno

Sandia National Laboratories, Albuquerque, New Mexico

(Received 22 January 1992)

The electronic states in a series of molecular-beam-epitaxy-grown CdTe/Cd₀.₇₉Zn₀.₂₁Te strained-layer single quantum wells have been studied both theoretically and experimentally. Calculations based on model solid theory and deformation-potential theory have shown that, at Zn concentration of 0.21 in the barriers, the band lineup is type I for heavy holes and type II for light holes. The confined states were calculated using the three-band envelope function model. Photoluminescence measurement at temperatures between 9 and 100 K indicates that the broadening mechanism is dominated by the polar optical phonon (longitudinal optical) interactions. The circularly polarized excitation spectra have shown predominant heavy-hole feature confirming that the band lineup is type I for heavy holes and type II for light holes. With well width between 25 and 75 Å, our study has shown that exciton binding energy decreases with decreasing well width.

I. INTRODUCTION

Recently, considerable interest has developed in strained-layer quantum wells and superlattices because of their potential for optoelectronics device applications. While less extensively studied than III–V compounds heterostructures, II–VI compounds quantum wells and superlattices are attracting more and more attention today. They offer the possibility to tune the energy gap to cover the spectrum range from near UV to the far infrared.[1–4] Besides, the strain effect splits and shifts the energy band in constituent layers and hence provides a

wealth of properties with which to design devices and study material physics. In the case of CdTe/Cd₀.₇₉Zn₀.₂₁Te, Harrison's linear combination of atomic orbitals (LCAO) theory indicates that it has a type-I band lineup configuration. When the strain effect is considered, however, it may end up to be simultaneously type I for heavy holes and type II for light holes.[5]

This paper reports on the photoluminescence (PL), excitation (PLE), and polarization spectra for CdTe/Cd₀.₇₉Zn₀.₂₁Te strained-layer single quantum wells with the band lineup configuration of Fig. 1. Following this introduction, the experiments are briefly described in Sec. II. Section III gives the calculation of confined electronic states in the strained-layer single quantum wells (SL SQW's) by a three-band envelope function model for strained-layer structure and all the observation of spectra and discussion are presented in Sec. IV.

FIG. 1. The band lineup of the strained-layer CdTe/Cd₀.₇₉Zn₀.₂₁Te quantum well.

II. EXPERIMENTS

Our samples were grown by molecular-beam epitaxy (MBE) on semi-insulating ⟨001⟩ GaAs substrates. The structures consist of a 4-μm-thick Cd₀.₇₉Zn₀.₂₁Te buffer layer; a CdTe single quantum well with the nominal thickness L_w of 25, 50, and 75 Å; and a 0.5-μm-thick Cd₀.₇₉Zn₀.₂₁Te cap layer (Fig. 1). The optical spectra were measured in the backscattering direction at ≈26° from the normal to the quantum-well layer, with the sample mounted on a cold finger cooled by a closed-cycle helium cryostat down to 8.5 K. The PL measurements were performed with an Ar⁺ laser for the Cd₀.₇₉Zn₀.₂₁Te barriers excitation (488-nm line) or by a tunable

FIG. 2. Composition dependence of $Cd_{1-x}Zn_xTe$ alloy band gap at 6 K, plotted using bowing parameter 0.294.

Ti:sapphire laser for barrier excitation or directly the CdTe quantum-well excitation. Luminescence spectra were recorded with a Jarell-Ash 0.75-m monochromator equipped with a 1180-grooves/mm grating. The detection electronics consists of thermoelectrically cooled photomultiplier with a fast preamplifier connected to a dual-channel gated photon counting system controlled by a computer, which also controls the scanning monochromator Jarell-Ash and tunable Ti:sapphire laser. The circular polarization of luminescence and excitation spectra were measured using a highly sensitive and absolute apparatus involving a photoelastic modulator (PEM). The system will be described in detail elsewhere.[6]

III. THEORY

A. Interpolation scheme for band lineup

In ternary alloys $A_{1-x}B_xC$, if AC and BC are lattice matched, linear interpolation is a valid procedure for variation of material parameters with x. But in ternary alloys constituted from lattice mismatched binaries, bowing effects should be taken into account. One material should be regarded as being compressed while the other being expanded. Therefore, from deformation theory we know that for a given band edge E_i we have[7,8]

$$E_i(x) = (1-x)E_i(AC) + xE_i(BC)$$

$$+ 3x(1-x)[a_i(AC) - a_i(BC)]\frac{\Delta a_0}{a_0} , \quad (1)$$

where

$$a_0 = (1-x)a(AC) + xa(BC) ,$$

$$\Delta a_0 = a_0(BC) - a_0(AC) .$$

a_0's are lattice constants and a_i's are the intraband (absolute) hydrostatic deformation potentials for band E_i.

For variation of band gap $E_g(x)$ with composition x we have

$$E_g(x) = E_c(x) - E_v(x)$$

$$= (1-x)E_g(AC) + xE_g(BC)$$

$$+ 3x(1-x)[a(AC) - a(BC)]\Delta a_0/a_0 , \quad (2)$$

where $a(AC)$ and $a(BC)$ are the interband (relative) hydrostatic deformation potentials: $a = a_c - a_v$. This leads to a bowing parameter

$$b \approx 3[a(AC) - a(BC)]\Delta a_0/a_0 . \quad (3)$$

Here a_0 chooses the midcomposition lattice constant. Note that in (2) and (3) we ignored the strain dependence of spin-orbit splitting which is normally insignificant (see next section). For the ternary alloy $Cd_{0.79}Zn_{0.21}Te$, using the parameters given in Table I, Eq. (3) gives $b = 0.378$.

According to Hill's theory,[9] the bowing parameter b can be calculated from the equation

$$b = \frac{Ze}{8\pi\varepsilon_0} \left[\left[\frac{1}{r_A} - \frac{1}{r_B} \right]^2 (r_A + r_B) \exp\left[-sa\frac{\sqrt{3}}{8} \right] \right] , \quad (4)$$

where Ze is the charge of the substituting ion, a is the lattice constant of the midcomposition alloy, s is the screening factor (0.25 Å^{-1}), and r_A, r_B are the Pauling's covalent radii of elements A and B, respectively.

With $a(CdTe) = 6.481$ Å and $a(ZnTe) = 6.1037$ Å,[4] the lattice constant of the midcomposition alloy is calculated to be $a = 6.29235$ Å. Using $r_{Cd} = 1.405$ Å and $r_{Zn} = 1.225$ Å,[29] the bowing parameter calculated by Eq. (4) is $b = 0.294$ (Fig. 2).

The experimental dependence of the energy band gap on alloy composition $(T = 6 K)$ given in Ref. 30 goes

$$E_g(Cd_{1-x}Zn_xTe) = 1.606(1-x) + 2.394x$$

$$- 0.26x(1-x) \text{ eV} . \quad (5)$$

Based on the above notation, the interpolation scheme

TABLE I. Parameter values used for calculations. $E_g(Cd_{1-x}Zn_xTe) = 1.606 + 0.494x + 0.294x^2$ (eV) (calculated using Hill's theory), $a(Cd_{1-x}Zn_xTe) = 6.481 - 0.3773x$ (Å), from Ref. 30 and using $m_e^*(Cd_{1-x}Zn_xTe) = 0.099 + 0.017x$, $\gamma_1(Cd_{1-x}Zn_xTe) = 4.11 - 0.04x$, $\gamma_2(Cd_{1-x}Zn_xTe) = 1.08 - 0.3x$, as defined in Ref. 4.

	E_g (Ref. 30) (eV)	Δ (Ref. 8) (eV)	a_v (Ref. 8) (eV)	a_c (Ref. 8) (eV)	b (Ref. 8) (eV)	a_0 (Ref. 30) (Å)	C_{11} (Ref. 8) C_{11} (Ref. 8)	C_{12} (Ref. 8) C_{12} (Ref. 8)	$E_{v,a}^a$ (eV)
ZnTe	2.394	0.91	0.79	−5.83	−1.26	6.1037	0.713	0.407	+0.03
CdTe	1.606	0.93	0.55	−3.96	−1.10	6.481	0.562	0.394	+0.21

[a] Relative to the top of GaAs valence band given by HAO theory (Ref. 10).

should be: starting from Harrison atomiclike orbital (HAO) theory's $E_{v\,av}(AC)$ and $E_{v\,av}(BC)$,[10] adding $\frac{1}{3}\Delta(AC)$ and $\frac{1}{3}\Delta(BC)$ to get $E_v(AC)$ and $E_v(BC)$, and then interpolating $E_v(x)$ by Eq. (1), and adding the experimental $E_g(x)$ or the $E_g(x)$ given by the bowing equation onto $E_v(x)$ to get $E_c(x)$. To get the spin-orbit splitting band $E_{s.o.}(x)$, the linearly interpolated $\Delta(x)$ is subtracted from $E_v(x)$. This gives all the band lineups before the strain between barrier and well layers is considered. The valence-band offset used above is in good agreement with the experimental data obtained from core-level x-ray photoemission spectroscopy.[10]

B. Strain effect on band edges

As mentioned before, all three of our samples have a buffer layer of 4 μm which is much thicker than its critical thickness so that the strain between the substrate and the buffer is relaxed, a cap layer of 0.5 μm which is, again, much thicker than the quantum wells (25, 15, and 75 Å). Therefore, it is quite reasonable to assume that only quantum-well layers are under a biaxial compressive strain which is equivalent to a hydrostatic strain plus a uniaxial strain. The hydrostatic component of the strain shifts the energy bands. The uniaxial component lifts the $J = \frac{3}{2}$ degeneracy and splits it into a pair of Kramers doublets.[11]

The strain Hamiltonian H_ε for a p-like multiplet can be expressed as[12]

$$\hat{H}_\varepsilon = \hat{H}_\varepsilon^{(1)} + \hat{H}_\varepsilon^{(2)} ,$$

$$\hat{H}_\varepsilon^{(1)} = -a_1 \text{Tr}(\varepsilon) - 3b_1[(\hat{L}_x^2 - \tfrac{1}{3}\hat{L}^2)\varepsilon_{xx} + \text{c.p.}]$$

$$\qquad - \sqrt{3}d_1[(\hat{L}_x\hat{L}_y + \hat{L}_y\hat{L}_x)\varepsilon_{xy} + \text{c.p.}] , \qquad (6)$$

$$\hat{H}_\varepsilon^{(2)} = -a_2(\hat{L}\cdot\sigma)\text{Tr}(\varepsilon) - 3b_2[(\hat{L}_x\sigma_x - \tfrac{1}{3}\hat{L}\cdot\sigma)\varepsilon_{xx} + \text{c.p.}]$$

$$\qquad - \sqrt{3}d_2[(\hat{L}_x\sigma_y + \hat{L}_y\sigma_x)\varepsilon_{xy} + \text{c.p.}] ,$$

where $\hat{H}_\varepsilon^{(1)}$ is the orbital-strain Hamiltonian and $\hat{H}_\varepsilon^{(2)}$ is the strain-dependent spin-orbit Hamiltonian, ε and ε_{ij} denote the strain tensor and its components, L is the orbital angular momentum operator, σ the Pauli matrix vector, and c.p. stands for cyclic permutation with respect to the indices x,y,z. a_1 is the intraband (absolute) hydrostatic deformation potential while b_1 and d_1 are orbital uniaxial deformation potentials appropriate to strains of tetragonal and rhombohedral symmetries, respectively. a_2, b_2, and d_2 are additional deformation potentials describing the effects of a strain on the spin-orbit interaction.

The effect of a strain on the conduction-band edge E_c is to produce a hydrostatic shift given by

$$\hat{H}_\varepsilon^{(c)} = a_c \text{Tr}(\varepsilon) , \qquad (7)$$

where a_c is the intraband (absolute) hydrostatic deformation potential of the conduction band. For the biaxial strain in $\langle 001 \rangle$ plane we have

$$\varepsilon_{xx} = \varepsilon_{yy} = \varepsilon = \frac{a_1 - a_0}{a_0} ,$$

$$\varepsilon_{zz} = -\frac{2C_{12}}{C_{11}}\varepsilon , \qquad (8)$$

$$\varepsilon_{xy} = \varepsilon_{yz} = \varepsilon_{zx} = 0 ,$$

where a_1 is the in-plane lattice constant, a_0 the lattice constant without strain, and C_{11}, C_{12} are elastic constants.

If we choose $|J, M_j\rangle$ basis which makes spin-orbit interaction diagonal, at $k = 0$, the Kane matrix becomes[13]

$$\begin{vmatrix} E_{c0} + \delta E_{H,c} & 0 & 0 & 0 \\ 0 & E_{v\,ac} + \dfrac{\Delta}{3} - \delta E_{H,v} - \delta E_s & 0 & 0 \\ 0 & 0 & E_{v\,ac} + \dfrac{\Delta}{3} - \delta E_{H,v} + \delta E_s & \sqrt{2}\delta E'_s \\ 0 & 0 & \sqrt{2}\delta E'_s & E_{v\,av} + \dfrac{2\Delta}{3} - \delta E'_{H,v} \end{vmatrix} , \qquad (9)$$

where

$$\delta E_{H,c} = a_c(2 - \lambda)\varepsilon ,$$

$$\delta E_{H,v} = (a_1 + a_2)(2 - \lambda)\varepsilon = a(2 - \lambda)\varepsilon ,$$

$$\delta E'_{H,v} = (a_1 - 2a_2)(2 - \lambda)\varepsilon = a'(2 - \lambda)\varepsilon ,$$

$$\delta E_s = -(b_1 + 2b_2)(1 + \lambda)\varepsilon = -b(1 + \lambda)\varepsilon ,$$

$$\delta E'_s = -(b_1 - b_2)(1 + \lambda)\varepsilon = -b'(1 + \lambda)\varepsilon ,$$

$$\lambda = 2C_{12}/C_{11} .$$

E_{c0} is the edge of the conduction band without strain and $E_{v\,av}$ is the center of gravity of the p-like multiplet given by HAO theory.[10]

Normally, the strain dependence of spin-orbit splitting is not very significant and we will ignore it ($a_2 \approx 0$, $b_2 \approx 0$). Therefore

$$a' \approx a_1 \approx a_c ,$$

$$b' \approx b_1 \approx b ,$$

$$\delta E_H \approx \delta E'_{H,v} \approx a_c(2 - \lambda)\varepsilon , \qquad (10)$$

$$\delta E_s \approx \delta E'_s \approx -b(1 + \lambda)\varepsilon .$$

The values for a_v and b are given in Table I. Under these approximations, the strain dependence of the four energy-band edges of interest can be written

$$E_c = E_{v\,av} + \frac{\Delta}{3} + E_g + \delta E_{H,c} \ ,$$

$$E_{hh} = E_{v\,av} + \frac{\Delta}{3} - \delta E_{H,v} - \delta E_s \ ,$$

$$E_{lh} = E_{v\,av} - \frac{\Delta}{6} - \delta E_{H,v} + \tfrac{1}{2}\delta E_s$$

$$+ \tfrac{1}{2}[\Delta^2 + 2\Delta\delta E_s + 9(\delta E_s)^2]^{1/2} \ ,$$ (11)

$$E_{s.o.} = E_{v\,av} - \frac{\Delta}{6} - \delta E_{H,v} + \tfrac{1}{2}\delta E_s$$

$$- \tfrac{1}{2}[\Delta^2 + 2\Delta\delta E_s + 9(\delta E_s)^2]^{1/2} \ .$$

C. Three-band envelope function model for strained-layer quantum wells

To calculate the confined electronic states in our samples, the strain effects discussed above need to be incorporated into the three-band envelope function model.[14] For a strained system, a change of coordinates for Euler coordinates r_E to Lagrange r_L is necessary to preserve the Hamiltonian H's periodicity[11]

$$r_E = r_L + u(r_L) \ ,$$ (12)

and for a given function $f_E(r_E) = f_L(r_L)$ we have

$$p_L f_L = (I + \varepsilon)p_E f_E \ ,$$

$$k_L = (I + \varepsilon)k_E \ .$$ (13)

Following the procedure in normal envelope function approach,[14,15] we end up with an equation

$$\cos(k_w' L_w) + \frac{1}{2}\left[\eta - \frac{1}{\eta}\right]\sin(k_w' L_w) = 0 \ .$$ (14)

This has the exact same form as in the unstrained case except for the expression of η and for the dispersion relation in each material,

$$\eta = \frac{(1 + \delta\varepsilon_w)k_w' m_b'(E)}{(1 + \delta\varepsilon_b)k_b' m_w'(E)} \ ,$$ (15)

$$[E - \delta E_{H,c}]\{[(E + E_g + \delta E_{H,v} - \delta E_s)$$

$$\times(E + E_g + \Delta + \delta E_{H,v})] - 2(\delta E_s)^2\}$$

$$= (1 - 4\delta\varepsilon)P^2 h^2 k_z'^2[E + E_g + \tfrac{2}{3}\Delta + \delta E_{H,v} - \delta E_s] \ ,$$ (16)

where

$$\delta\varepsilon = \varepsilon_{zz} - \varepsilon_{xx} = \left[\frac{C_{11} + 2C_{12}}{C_{11}}\right]\varepsilon \ ,$$

E_g, Δ are energy-band gap and s.o. splitting and $m_b'(E), m_w'(E)$ are given by the relation

$$E = \frac{h^2 k'^2}{2m'(E)} \ .$$ (17)

$\delta E_{H,v}, \delta E_{H,c}, \delta E_s$ are defined in Eq. (9). The results here are similar to that of Marzin et al.[15] Due to the strain effect, our samples have type-II energy-gap configuration as shown in Fig. 1.

Our calculated optical gap $(E_{1e} - E_{1h})$ and experimental value of the free-exciton transition 1e-1h are plotted in Fig. 3 as functions of well width L_w. We take the difference between the experimental points ($\triangle$) and calculated optical gaps as binding energy of the free exciton (E_{bx}). As predicted by theoretical calculation,[16–19] E_{bx} first increases with decreasing L_w because of the tendency to a two-dimensional behavior and then, beyond a certain point, E_{bx} decreases due to the recovery of a three-dimensional behavior through the increasing penetration of electron and hole wave function in the barrier.

The three-dimensional (3D) exciton binding energies given in Ref. 20 are 12 meV for CdTe and 13 meV for ZnTe. For the 50-Å-thick CdTe quantum-well sample in this study, the value of E_{bx} is estimated to be about three times larger (36.5 meV) than that of the 3D exciton. In Ref. 5, the E_{bx} for a 50-Å-thick CdTe quantum-well sample is also reported to be more than two times larger (25 meV) than that of a 3D exciton. The main difference between the samples used here and Ref. 5 is in the barrier Zn composition x. In the sample used here, x is 0.21, while in Ref. 5 x is only 0.08. A larger x value can have two effects. First, a larger x gives a wide band gap in the barrier layer and hence a higher potential barrier. Second, a larger x value in the barrier layer causes larger strain in the well, pushing both electron and heavy-hole well deeper. Both of these effects enhance the two-dimensional (2D) feature of the exciton in the quantum well, enlarging the binding energy E_{bx}. The accuracy in the deduced E_{bx} values is dependent on the precision of parameters such as deformation potentials a_c, a_v, b, and elastic constants C_{11}, C_{12} used for calculations. Different values for these parameters have been used in literature.[1–5,30]
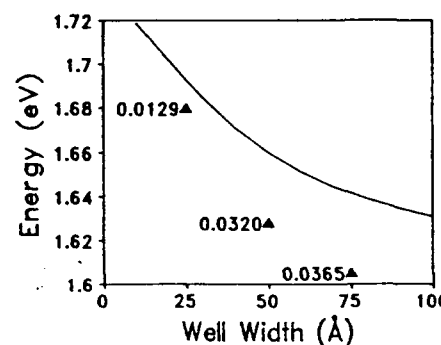
FIG. 3. The exciton transition energies as a function of well width. Solid line shows the calculated transition energies (1e-1h), and $\triangle$ represents the experimental points. The numbers beside the experimental data are the difference between calculated and measured data in eV.

IV. RESULTS AND DISCUSSION

A. PL at different temperatures

Figure 4 shows the PL spectra of the samples with well width 25, 50, and 75 Å, respectively. The spectra were measured at 9.0 K using the 488-nm Ar$^+$ laser line for excitation. The excitation is indirect (i.e., free carriers are photogenerated in Cd$_{0.79}$Zn$_{0.21}$Te barriers and then transferred into CdTe wells.) As expected, the sharp emission peak was shifted to lower energy and became narrower as the well width was increased. The main emission peak cannot be explained by a single line (it is neither Gaussian nor Lorentzian). Instead, it can be fitted gracefully to a combination of two lines, one Gaussian and one Lorentzian as shown in Fig. 5. The least-square fit of QW-3 ($L_w = 75$ Å)'s spectrum yields linewidths of 7.553 and 6.65 meV, centered at 1.6049 and 1.6005 eV, respectively. In the bulk binary II–VI semiconductors, the linewidth of the bound exciton is smaller than kT since the bound exciton has no kinetic energy. The line shape is described by the Lorentzian function.[21] The free-exciton line shape is described by Gaussian function. We believe that the Gaussian peak at 1.6049 eV originates from the confined $n = 1$ electron and $n = 1$ heavy-hole free-exciton transition and the Lorenzian peak at 1.6005 meV is attributed to the excitons bound to neutral acceptors (E_{1h}-A^0) in a CdTe quantum well. Similar high-quality fittings were also obtained for the other two samples except that sample QW1 ($L_w = 25$ Å) exhibits one additional peak on the lower energy side of the main emission peak, which, by comparison with the PL spectra of 3-μm Cd$_{0.79}$Zn$_{0.21}$Te epitaxy layer grown at the same conditions as the buffer layer in our quantum-well samples [Fig 4(d)], is attributed to an unidentified band at buffer-substrate interface. This band also exists at the buffer-substrate interface of the other two samples ($L_w = 50$ and 75 Å). However, we cannot see it because the optical gap (window) in these two samples are too narrow to let this emission come out. Figure 6 shows the PL spectra of QW-1 ($L_w = 25$ Å) at different excitation intensities. The spectrum a was recorded at the excitation intensity 10 W/cm^2 and spectrum b at 40 W/cm^2 us-
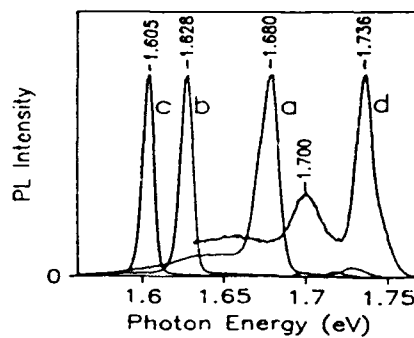
FIG. 5. The decomposition of the PL spectrum for (a) QW-3 single quantum well to two components spectra, (b) free-exciton Gaussian shape, and (c) bound exciton Lorentzian shape.

ing an Ar$^+$ ion laser line 488 nm. The spectra are normalized at maximum. The additional low-energy band gets saturated at a higher excitation intensity. Such behavior suggests that the additional band may be determined by defects.[22]

The temperature dependence of the PL spectra of QW-3 ($L_w = 75$ Å) is shown in Fig. 7. The photoluminescence is quenched mainly due to the thermally activated nonradiative recombination channel in the well and the temperature dependence transfer mechanism of photogenerated carriers from barrier to well. The inset shows the activation energies obtained from the quenching data of the decomposed free-exciton emission peak. Figure 8 shows the temperature dependence of the linewidth of the free-exciton emission. The full width at half maximum (FWHM) of the $n = 1$ electron–heavy-hole excitonic emission increases slowly in the temperature range of 9–50 K, but increases rapidly with temperature above 50 K. This behavior is described by the equation[23]

$$\Gamma_{tot} = \Gamma_0^+ + \Gamma_{ph} \left[\exp\left[\frac{E_{LO}}{kT} \right] - 1 \right]^{-1}$$

$$+ \Gamma_{imp} \exp\left[\frac{-\langle E \rangle}{kT} \right], \tag{18}$$

where the first term Γ_0^+ is the linewidth due to the inhomogeneous fluctuation of the well thickness. Second term Γ_{ph} describes the interactions between exciton and longitude optical (LO) phonon, and the last term Γ_{imp} is the linewidth due to the ionized-impurity scattering. $\langle E \rangle$ is the average binding energy of impurities. Fitting the above equation to our data yields the solid line in Fig.


FIG. 4. Photoluminescence spectra of CdTe/Cd$_{0.79}$Zn$_{0.21}$Te single-quantum-well heterostructures with well widths (a) 25, (b) 50, and (c) 75 Å, respectively, under indirect excitation. Spectra (d) is the photoluminescence of Cd$_{0.79}$Zn$_{0.21}$Te epitaxial layers shown for comparison.
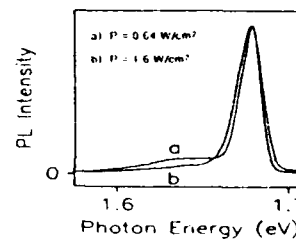
FIG. 6. Photoluminescence spectrum for single-quantum-well QW-1 under different excitation intensities.

FIG. 9. (A) The polarized excitation spectra excited by circularly polarized σ^-. The polarized spectra (a) σ^+ and (b) σ^- are obtained when detecting at the longer wavelength side of free-exciton transition $1e$-$1h$. Curve c is the degree of circular polarization. (B) Phonon-assisted cooling processors for hot electrons.
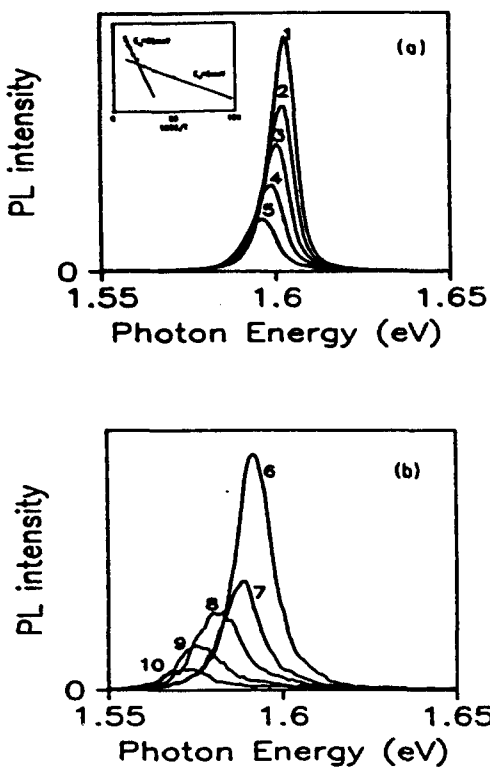
FIG. 7. The photoluminescence spectra of a CdTe/Cd$_{0.79}$Zn$_{0.21}$Te single-quantum-well heterostructure of well width L_w=75 Å, measured at different temperatures between (a) 10 and 50 K (step 10 K), and (b) 60 and 100 K, under indirect excitation with Ar$^+$-ion laser line 488 nm. The inset shows the Arrhenius plot of integrated PL intensity versus $1/T$ which reviles two activation energies 25 and 5 meV.

8 with the parameters Γ_0^+=75 meV, Γ_{ph}=400 meV, E_{LO}=22 meV, Γ_{imp}=500 meV, and $\langle E \rangle$=92 meV.

B. Circularly polarized excitation spectra

Since the calculation has shown that the band lineup is type I for heavy holes and type II for light holes, the main emission peak is expected to be characterized predominantly by the heavy-hole feature, which is clearly shown in our circular polarization optical pumping spectra (Fig. 9). The degree of circular polarization ρ is defined as [24]

$$\rho = \frac{I_+ - I_-}{I_+ + I_-} , \qquad (19)$$

where I_+ and I_- are the intensities of right and left circularly polarized (σ_+ and σ_-) radiation.

In bulk material, according to the selection rule shown in Fig. 10(a), the maximum degree of circular polarization that can be expected is only 0.25 because of the degeneracy at the top of the valence band. [25]

In the case of SL SQW's or SL SL's, on one hand the removal of the degeneracy by strain and confinement suggests that degree of circular polarization as high as 100% could be observed. On the other hand, however, the mixing of the states due to the in-plane dispersion lowers the degree of polarization. Furthermore, the spin relaxation

FIG. 8. Temperature dependence of linewidth (FWHM) of free-excitonic emission. The solid curve is the best fit to Eq. (18). Experimental data are indicated by ▼.
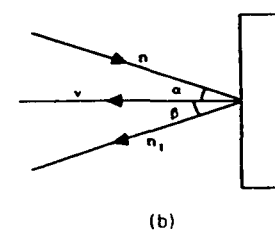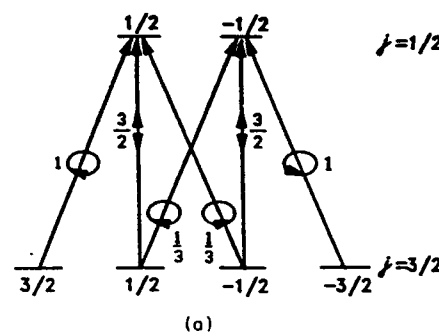
FIG. 10. (a) Selection rules for optical transitions and relative intensities. (b) The excitation and observation geometry in relation to sample orientation.

of the photogenerated carrier also reduces the degree of polarization. And finally, the orientation of the sample relative to the direction of the excitation beam and observation direction also affects the observed degree of polarization.[24,25]

$$\rho \propto \frac{2(v \cdot n_1)(v \cdot n)}{1+(v \cdot n)^2} = -\frac{2 \cos\alpha \cos\beta}{1+\cos^2\alpha} , \quad (20)$$

where n, n_1, and v are unit vectors in the direction of excitation beam, observation, and sample growth respectively [see Fig. 10(b)].

The circularly polarized excitation spectrum of QW-3 (L_w=75 Å) is shown in Fig. 9(a). The transition monitored is the long-wavelength side of the free exciton ($1e$-$1h$) at 1.605 eV. The excitation source was a continuous wave (cw)Ti:sapphire tunable laser. The light from the laser was circularly polarized (σ^-) by an achromatics circular polarizer. The detecting system record simultaneously in two gated photon counters the σ^+ and σ^- components of the luminescence light which are curves a and b, respectively. Curve c is the circularly polarized excitation spectrum calculated using Eq. (19). Similar spectra were obtained for all the SQW samples studied. The forbidden transition ($1e$-$2h$, $1e$-$3h$, etc.) energies, according to our calculations, happen to be in the valleys of the excitation spectra shown in Fig. 9(a). Therefore, the peaks in Fig. 9(a) at 1.683, 1.663, and 1.639 eV are related to the LO phonon replicas (bulk CdTe's LO-phonon energy is 21 meV) as indicated in Fig. 9(b).

As one can see in Fig. 9(a), when the excitation energy $h\nu$ is above the barrier (but smaller than $E_{gb}+\Delta$ of the barrier), most of the spin orientation of photogenerated carriers created by σ_+ excitation are relaxed in the process of transferring to the quantum well and subsequent thermalization (or cooling) in the quantum well before recombination, and hence a very low degree of polarization is observed. When the excitation energy $h\nu$ is below the barrier such that $[h\nu-(E_{1e}+E_g+E_{1hh})]m_{hh}/(m_{hh}+m_e)$ is a multiple of the LO phonon energy $h\omega_{LO}$, the excited hot electrons emit LO phonons and fall directly to the bottom of the subband retaining most of their spin orientation.[26] The gradual decrease of the degree of luminescence polarization with increasing number of emitted LO phonons indicates noticeable spin relaxation at each stage of the cascade. When the condition $[h\nu-(E_{1e}+E_g+E_{1hh})]m_{hh}/(m_{hh}+m_e)=nh\omega_{LO}$ is not fulfilled, the cooling process always involves emission of a great number of acoustic phonons, and spin orientation of the hot electrons is significantly relaxed. When the excitation photon (σ^+) energy $h\nu$ is resonant with the emission peak, the degree of circular polarization as high as 73% is observed.

C. Collection of photogenerated carriers into the wells

Assuming a uniform absorption coefficient of 5×10^{-4}/cm for Cd$_{0.79}$Zn$_{0.21}$Te at 10 K at 488 nm, 99% of the incident photons during a PL experiment are absorbed within the 0.5-μm-thick cap (barrier) layer,

though thin quantum wells give very intense PL (I_w is 50 times stronger than I_b). Evidently, most of the carriers generated in the barrier are transferred into the well before recombination occurs. The carrier collection dynamics of SQW's have been studied by many groups.[27,28] The simple lumped continuity equations are written

$$g_b d_b = \frac{n_b}{\tau_{rb}} + \frac{n_b}{\tau_{nrb}} + \frac{n_b}{\tau_{tr}} ,$$

$$g_w d_w + \frac{n_b}{\tau_{tr}} = \frac{n_w}{\tau_{rw}} + \frac{n_w}{\tau_{nrw}} , \quad (21)$$

where the subscript r, nr, and tr denote radiative, nonradiative, and transfer; b and w denote the barrier and well, respectively; n_b and n_w are the two-dimensional minority-carrier concentrations; $g_b d_b$ and $g_w d_w$ are the two-dimensional generation rate in the barrier and the well; and τ's are the associated minority-carrier lifetimes. The τ_{tr} is the time needed to transfer photogenerated carriers from a 5000-Å barrier into the well. The internal radiative recombination rate per unit area I_b and I_w are given

$$I_b = \frac{n_b}{\tau_{rb}} ,$$

$$I_w = \frac{n_w}{\tau_{rw}} . \quad (22)$$

From Eqs. (21) and (22) one can obtain

$$\frac{I_w}{I_b} = \frac{\dfrac{\tau_{rb}}{\tau_{tr}} + \left[1+\dfrac{\tau_{rb}}{\tau_{tr}}+\dfrac{\tau_{rb}}{\tau_{nrb}}\right]\dfrac{g_w d_w}{g_b d_b}}{1+\dfrac{\tau_{rw}}{\tau_{nrw}}}$$

$$= \eta_w \frac{\tau_{rb}}{\tau_{tr}} \left[1+\left[1+\dfrac{\tau_{tr}}{\tau_{rb}}+\dfrac{\tau_{tr}}{\tau_{nrb}}\right]\dfrac{g_w d_w}{g_b d_b}\right] . \quad (23)$$

The ratio I_w/I_b can be approximated by the ratio of integrated PL intensities if we assume identical conversion factors linking the external and internal radiative recombination rates for the well and the barrier. It is quite reasonable to assume $\eta_w=1$.[28] Neglecting of carrier generation in the well simplifies (23) to

$$\frac{I_w}{I_b} = \frac{\tau_{rb}}{\tau_{tr}} \eta_w . \quad (24)$$

Now, the time needed to transfer the photogenerated carriers from the 5000-Å-thick Cd$_{0.79}$Zn$_{0.21}$Te barrier to the CdTe well can be estimated if the radiative minority-carrier lifetime in the barrier is known.

$$\tau_{tr} = \frac{I_b}{I_w} \eta_w \tau_{tr} \approx \frac{\tau_{rb}}{50} \eta_w . \quad (25)$$

Assuming that the radiative lifetime in the barrier is the same as in bulk ZnTe, about ≈ 2 ns, and the quantum efficiency in well is $\eta_w=1$, the estimated transfer time τ_{tr} is 40 ps. If quantum efficiency η_w is not equal to unity, the transfer time should be shorter. From a Streack

Camera measurement under direct excitation, the emission from the well reached its peak about 550 ps after excitation pulse. That time is the sum of the transfer time, the exciton creation time, and radiative lifetime of the exciton in the well $(\tau_{tr} + \tau_{cx} + \tau_{rw})$. The radiative lifetime of exciton in the well is about 510 ps if we ignore the exciton creation time τ_{cx}.

V. CONCLUSION

In conclusion, we have reported theoretical calculations and experimental results on $CdTe/Cd_{0.79}Zn_{0.21}Te$ strained-layer single quantum wells. We have presented theoretical calculations for the confined carrier energies using the three-band envelope function model including the strain effect. Based on Hill's and model solid theories, we have computed the band gap of the $Cd_{0.79}Zn_{0.21}Te$ alloy as a function of composition x. The calculated bowing parameters are 0.294 and 0.303 from Hill's theory[9] and model solid theory,[8] respectively.

The exciton binding energies were estimated from the difference between the calculated $1e$-$1h$ transitions in well and experimental free-exciton transitions (Fig. 3). The binding energy is reduced from 36.5 to 12.9 meV when well width is reduced from 75 to 25 Å. This behavior is predicted by theory. In the range of investigated quantum well widths, the binding energy E_{bx} decreases with reduction of the well width. This is due to the recovery of a three-dimensional behavior through the increasing penetration of the electron and hole wave functions in the barrier.

The analysis of the free-exciton linewidth as a function of temperature indicated that the broadening mechanism is dominated by the polar optical phonon (LO) interactions. The temperature dependence of the integrated intensities of free excitons yield activation energies of 25 meV in high-temperature regions and 5 meV in low-temperature regions. The activation energy 25 meV corresponds to the dissociation of the free excitons.

The polarized excitation spectra have shown a predominant heavy-hole feature. No light-hole transitions were observed. This confirms that the lineup configuration is type I for heavy holes and type II for light holes.

ACKNOWLEDGMENTS

*Permanent address: Electrical and Computer Engineering Department, Ohio University, Athens, OH 45701.

[1]Y. Merle d'Aubigné, Le Si Dang, F. Dal'bo, G. Lentz, N. Magnéa, and H. Mariette, Superlatt. Microstruct. 5, 367 (1989).

[2]H. Mathieu, J. Allegre, A. Chatt, P. Lefebvre, and J. P. Faurie, Phys. Rev. B 38, 7740 (1988).

[3]B. Gill, D. J. Dunstan, J. Calatayud, H. Mathieu, and J. P. Faurie, Phys. Rev. B 40, 5522 (1988).

[4]J. Allegre, J. Calatayud, B. Gil, H. Mathieu, H. Tuffigureo, G. Lentz, N. Magnea, and H. Mariette, Phys. Rev. B 41, 8195 (1990).

[5]H. Mariette, F. Dalbo, N. Magnea, G. Lentz, and H. Tuffigureo, Phys. Rev. B 38, 12443 (1988).

[6]H. J. Lozykowski, T. Li, and Z. Akir, Rev. Sci. Instrum. (to be published).

[7]M. Cardona and N. E. Christensen, Phys. Rev. B 37, 1011 (1988).

[8]Chris G. Van de Walle, Phys. Rev. B 39, 1871 (1989).

[9]R. Hill, J. Phys. C 7, 521 (1974).

[10]H. Kroemer, in Molecular Beam Epitaxy and Heterostructures, NATO Advanced Study Institute Series B: Physics, edited by L. L. Chang and K. Ploog (Nijhoff, Dordrecht, 1985); T. M. Duc, C. Hsu, and J. P. Faurie, Phys. Rev. Lett. 58, 1127 (1987).

[11]G. L. Bir and G. E. Pikus, Symmetry and Strain-Induced Effects in Semiconductors (Wiley, New York, 1974).

[12]F. H. Pollak, in Semiconductors and Semimetals, edited by T. P. Pearsall (Academic, San Diego, 1990), Vol. 32.

[13]E. O. Kane, in Semiconductors and Semimetals, edited by R. K. Willardson and A. C. Beer (Academic, New York, 1966), Vol. 1.

[14]G. Bastard (unpublished).

[15]J. Y. Marzin, J. M. Gerald, P. Voison, and J. A. Brum, in Semiconductors and Semimetals (Ref. 12).

[16]R. L. Green, K. K. Bajaj, and D. E. Phileps, Phys. Rev. B 29, 1807 (1984).

[17]G. Bastard, E. E. Mendez, L. L. Chang, and L. Esaki, Phys. Rev. B 26, 1974 (1982).

[18]J. A. Brum and G. Bastard, J. Phys. C 18, L789 (1985).

[19]J. A. Brum and G. Bastard, Phys. Rev. B 31, 3893 (1985).

[20]D. C. Reynolds and T. C. Collins, Excitons: Their Properties and Uses (Academic, New York, 1981).

[21]E. F. Schubert and W. T. Tsang, Phys. Rev. B 34, 2991 (1986).

[22]G. Ambrazecius, S. Marcinkevicius, T. Lideikis, and K. Nandzius, Semicond. Sci. Technol. 6, 41 (1991).

[23]J. Lee, E. S. Koteles, and M. O. Vassell, Phys. Rev. B 33, 5512 (1986).

[24]C. Weishbuch, R. C. Miller, R. Dingle, A. C. Gossard, and W. Wiegmann, Solid State Commun. 37, 219 (1987).

[25]V. I. Perel and B. P. Zakharchenya, in Modern Problems in Condensed Matter Science, edited by F. Meier (North-Holland, Amsterdam, 1984), Vol. 8.

[26]G. E. Pikus and A. N. Titkov, in Modern Problems in Condensed Matter Science (Ref. 25).

[27]E. H. Reihlen, A. Persson, T. Y. Wang, K. L. Fry, and G. B. Stringfellow, J. Appl. Phys. 66, 5554 (1989).

[28]D. Bimberg, J. Christen, A. Steckenborn, G. Weimann, and W. Schlap, J. Lumin. 30, 562 (1985).

[29]W. Giriat and J. K. Furdyna, in Semiconductors and Semimetals, edited by J. K. Fyrdyna and J. Kossut (Academic, Orlando, 1988), Vol. 25.

[30]G. Nimtz, in Numerical Data and Functional Relationships in Science and Technology, edited by O. Madelung, Landolt-Börnstein, New Series, Group III, Vol. 17, Part 6 (Springer-Verlag, Berlin, 1982), Chap. 3, p. 247.